UNIVERSIDADE D
COIMBRA

Pedro Nuno Sousa Leite da Silva

Investigation on Iguratimod

STUDIES IN SOLID STATE AND IN SOLUTION

Dissertação no âmbito do Mestrado em Química Medicinal, orientada pela Professora Doutora Teresa Margarida Roseiro Maria Estronca e pelo Professor Doutor João Carlos Canotilho Lage e apresentada ao Departamento de Química da Faculdade de Ciências e Tecnologia da Universidade de Coimbra.

Setembro de 2022

Faculdade de Ciências e Tecnologia da Universidade de Coimbra

INVESTIGATION ON IGURATIMOD

STUDIES IN SOLID STATE AND IN SOLUTION

Pedro Nuno Sousa Leite da Silva

Dissertação no âmbito do Mestrado em Química Medicinal, na área de especialização em Química Avançada e Industrial, orientada pela Professora Doutora Teresa Margarida Roseiro Maria Estronca e pelo Professor Doutor João Carlos Canotilho Lage e apresentada ao Departamento de Química da Faculdade de Ciências e Tecnologia da Universidade de Coimbra.

Setembro de 2022

UNIVERSIDADE D
COIMBRA

“O que sabemos é uma gota; o que ignoramos é um oceano. Mas o que seria o oceano se não infinitas gotas?”

- Isaac Newton

AGRADECIMENTOS

Foi um percurso longo, sem dúvida longo, mas que nunca na minha vida irei esquecer. Sair da casa dos pais e ir estudar para uma cidade desconhecida a 200 km de casa foi, como seria de esperar, uma aventura. Desde os anos passados na tuna, da praxe, do ambiente jovem no centro da cidade de Coimbra, da "casa" em que vivi desde o meu segundo ano na universidade, e que não sei como é que ainda não caiu, até aos amigos que me acompanharam nos bons, e menos bons momentos. Só tenho a agradecer, só queria poder repetir.

Aos meus orientadores, a Professora Teresa Roseiro e o Professor João Canotilho, que tanta paciência tiveram comigo, e incessantemente me apoiaram ao longo deste percurso.

Ao Professor Ricardo Castro e à Professora Ermelinda Eusébio, por toda a ajuda no desenvolvimento deste projeto, e por terem tornado o percurso mais leve e divertido.

Ao João Baptista, que na prática também foi meu orientador. O teu apoio foi fundamental. Estarei para sempre em dívida.

Ao grupo de Termodinâmica e Química do Estado Sólido e ao UCQFarma, por me aceitarem e acolherem.

À Professora Maria João Moreno, ao Carlos Coelho, e a todo o grupo de Química Biológica, pela parceria no trabalho, por toda a incansável ajuda, e por tudo aquilo que me ensinaram.

A todos os meus amigos que conheci aqui em Coimbra, especialmente o João Santos, a Rita Neves, o Amílcar Prata, a Maria Pereira, o Rui Santos, o Tiago Pinto, o Rui Frias, a Joana Brás e a Carolina Fernandes. Vocês fizeram isto tudo valer a pena, nunca me vou esquecer de todas as memórias que criamos. Coimbra sem Coça não é a mesma.

Aos amigos de Guimarães, o Nuno Braga, o João Caldas, o António Jorge, o André Salgado, e a todos os outros. Aos bons anos que vivemos, e, acima de tudo, aos que viveremos!

Aos meus pais, Francisco Silva e Inês Sousa, ao meu irmão, o Tomás, e a toda a minha família. Sem dúvida os meus pilares motivacionais, que tanto apoio me deram e dão. Sem vocês não estaria aqui.

INDEX

LIST OF FIGURES

LIST OF TABLES

ABBREVIATIONS

Ace - Acetone
ACN - Acetonitrile
API - Active pharmaceutical ingredient
BCS - Biopharmaceutics classification system
bioDMARDs - Biologic disease-modifying antirheumatic drugs
CCDC - Cambridge Crystallographic Data Center
DCM - Dichloromethane
DDAB - Dimethyldioctadecylammonium bromide
DLS - Differential light scattering
DMARDs - Disease-modifying antirheumatic drugs
DMF - Dimethylformamide
DMSO - Dimethyl sulfoxide
DSC - Differential Scanning Calorimetry
DTA - Differential Thermal Analysis
EtOAc - Ethyl acetate
EtOH - Ethanol
FA - Folic acid
FS - Fluorescence spectroscopy
FTIR-ATR - Fourier transform infrared spectroscopy with attenuated total reflectance
GRAS - Generally regarded as safe
ICH - International council for harmonisation of technical requirements for pharmaceuticals for Human use
IGU - Iguratimod
LAG - Liquid-assisted grinding
LEF - Leflunomide
LUVs - Large unilamellar vesicles
MCP - Metoclopramide
NA - Nicotinamide
Na_2HPO_4 - Sodium phosphate dibasic
NaCl - Sodium chloride
NCEs - New chemical entities
NF-κB - Nuclear Factor Kappa-light-chain-enhancer of Activated B Cells
NG - Neat grinding
NSAIDs - Nonsteroidal anti-inflammatory drugs
OPZ - Omeprazole
PBS - Phosphate-buffered saline
PLTM - Polarized light thermal microscopy

POPC - 1-palmitoyl-2-oleoyl-sn-glycero-3-phosphocholine
Q3C - Guideline for residual solvents
QS - Quinine sulphate
RA - Rheumatoid Arthritis
SSZ - Sulfasalazine
TG - Thermogravimetric Analysis
Tm - Lipid transition temperature
TX-100 - Trition X-100
UV-Vis - Ultraviolet-visible spectroscopy
XRPD - X-ray powder diffraction

ABSTRACT

Drug discovery and development is a complex, time-consuming, and resource demanding process. Despite technological advances in the pharmaceutical industry over the years, many diseases still don't have a cure, and many others lack proper treatment. Thus, new drugs are continually required by the healthcare systems to address unmet medical needs.

Rheumatoid arthritis is an autoimmune and inflammatory disease which leads to progressive loss of motor function. Disease-modifying antirheumatic drugs are often used as the first-line treatment. However, patient variability in response to treatment with these drugs continuously demands that new alternatives for both monotherapy and combinatory therapy are found.

Iguratimod (IGU) is a synthetic non-steroidal anti-inflammatory disease modifying anti-rheumatic drug used for the treatment of rheumatoid arthritis. It has shown positive results both when administered alone, and in combination with methotrexate. The scarcity of information about IGU in literature makes this compound a very interesting subject of study.

In the present work, solid-state characterization and investigation of IGU was conducted with calorimetric and spectroscopic techniques. Solvate formation was observed with acetonitrile, methanol and dimethylformamide, but not with acetone, ethanol, ethyl acetate, and dimethyl sulfoxide. The structure of the solvate with dimethylformamide was solved with SCXRD. A new polymorphic form of IGU was also found, by crystallization in dimethyl sulfoxide.

Alternative solid formulations for enhancement of physicochemical properties were studied, specifically cocrystals, amorphous, and coamorphous, with six other compounds: leflunomide, sulfasalazine, nicotinamide, folic acid, metoclopramide and omeprazole. A cocrystal with leflunomide was obtained in a 2:1 molar ratio (IGU:LEF) with liquid assisted grinding. Additionally, coamorphous of IGU with leflunomide (1:1), sulfasalazine (1:1), nicotinamide (1:1 and 1:2), and folic acid (1:1) were also obtained, with neat grinding.

IGU was characterized in solution, and its molar absorption coefficient (ε_{IGU} (347 nm) = 1.44 x 10^4 $M^{-1}cm^{-1}$), pK_a (pK_a = 6.3), and fluorescence quantum yield (Φ_F = 0.0007 for the neutral specie, and Φ_F = 0.0779 for the deprotonated specie) were experimentally determined. Furthermore, lipid interaction was investigated with POPC and DDAB, using a partition model. IGU showed good partitioning to POPC (K_L = 4.60 x 10^1 [7, 106]), and even better partitioning to POPC:DDAB (9:1) (K_L = 1.46 x 10^2 [107, 193]). Permeation with POPC large unilamellar vesicles was also studied. IGU desorption from and permeation through the lipid bilayer was showed to occur in a time scale comparable to that of elution from the chromatographic columns, rendering most of the results obtained in this experiment inconclusive.

RESUMO

A descoberta e desenvolvimento de fármacos é um processo complexo, demorado e exigente. Apesar dos avanços tecnológicos na indústria farmacêutica ao longo dos anos, muitas doenças ainda não têm cura, e muitas outras carecem de tratamento adequado. Assim, novos medicamentos são constantemente exigidos pelos sistemas de saúde para responder a necessidades médicas emergentes.

A artrite reumatoide é uma doença autoimune e inflamatória que leva à perda progressiva da função motora. Os fármacos antirreumáticos modificadores de doença são frequentemente utilizados como tratamento primário. Contudo, a variabilidade de resposta entre pacientes ao tratamento com estes medicamentos exige que sejam continuamente encontradas novas alternativas, tanto para a monoterapia como para a terapia combinatória.

O iguratimode (IGU) é um anti-inflamatório não esteroide sistémico, pertencente à classe dos fármacos antirreumáticos modificadores de doença, utilizado para o tratamento da artrite reumatoide. Este composto demonstrou resultados positivos quando administrado sozinho, e também em combinação com metotrexato. A falta de informação sobre o IGU na literatura faz deste composto um alvo de estudo interessante.

No presente trabalho, a caracterização e investigação do estado sólido do IGU foi conduzida com recurso a técnicas calorimétricas e espectroscópicas. A formação de solvatos foi observada com acetonitrilo, metanol e dimetilformamida, mas não com acetona, etanol, acetato de etilo, ou dimetilsulfóxido. A estrutura do solvato com dimetilformamida foi resolvida com SCXRD. Foi também encontrada uma nova forma polimórfica do IGU, por cristalização em dimetilsulfóxido.

Foram estudadas formulações sólidas alternativas, para o melhoramento das propriedades físico-químicas, em particular cocristais, amorfos, e coamorfos, com seis outros compostos: leflunomida, sulfassalazina, nicotinamida, ácido fólico, metoclopramida e omeprazol. Foi obtido um cocristal com leflunomida numa proporção 2:1 molar (IGU:LEF) com moagem assistida por solvente. Além disso, também foram obtidos coamorfos de IGU com leflunomida (1:1), sulfassalazina (1:1), nicotinamida (1:1 e 1:2), e ácido fólico (1:1), com neat grinding.

O IGU foi caracterizado em solução, e o seu coeficiente de absorção molar (ε_{IGU} (347 nm) = 1.44 x 10^4 $M^{-1}cm^{-1}$), pK_a (pK_a = 6.3), e o rendimento quântico de fluorescência (Φ_F = 0.0007 para a espécie neutra, e Φ_F = 0.0779 para a espécie desprotonada) foram determinados experimentalmente. Além disso, a interação com lípido foi investigada com POPC e DDAB, utilizando um modelo de partição. O IGU mostrou uma boa partição para POPC (K_L = 4.60 x 10^1 [7, 106]), e ainda melhor partição para POPC:DDAB (9:1) (K_L = 1.46 x 10^2 [107, 193]). Foi também estudada a permeação com vesículas unilamelares grandes de POPC. Foi demonstrado que a dessorção e a

permeação do IGU através da bicamada lipídica ocorreu numa escala temporal comparável à da eluição a partir das colunas cromatográficas, tornando grande parte dos resultados obtidos nesta experiência inconclusivos.

1 - INTRODUCTION

1.1 – Rheumatoid Arthritis

Rheumatoid arthritis (RA) is a chronic autoimmune disease which affects mostly women, between the ages of 30 and 60. It causes joint swelling, deformity, and severe pain, eventually leading to motor disfunction.[1]

Its inflammatory nature has brought early interest in treatment with nonsteroidal anti-inflammatory drugs (NSAIDs). In cases which RA does not show an overtime development, these offer a good solution to alleviate some of the symptoms. Corticosteroids may also be used as a short-term solution to acute flares. However, since none of these have any influence in disease progression, they are perceived as non-sufficient for long-term treatment.[2,3]

Disease-modifying antirheumatic drugs (DMARDs) are immunosuppressive and/or immunomodulatory agents, commonly used in inflammatory arthritis, such as RA. Conventional DMARDs include methotrexate, which is the first-line DMARD, but also leflunomide, hydroxychloroquine, and sulfasalazine. Extended treatment with DMARDs usually slows down RA progression, even leading to remission, in cases of early diagnosis.[2,3] Due to RA's complexity, combinatory therapy is often used in case of monotherapy failure. Ultimately, biologic DMARDs (bioDMARDs) may be used in combination with DMARDs, providing more specific response, by targeting a particular step of the inflammatory pathway.[3,4] **FIG. 1** shows a summary of the most common treatment options for RA.

Nowadays, there are still many cases of inadequate response to DMARDs from patients, as well as the side effects connected to the continued use of some of these drugs. Suboptimal handling of RA can lead to irreversible structural damage on the body. Thus, the search for new and more efficient DMARDs remains in high demand to increase treatment options. The cure for rheumatoid arthritis is yet to be found.[5]

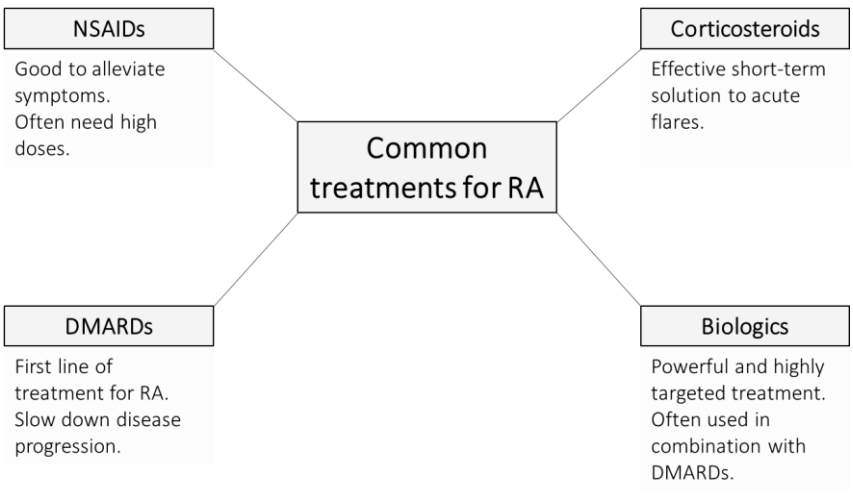

FIG. 1 – Schematic of the most commonly implemented treatments for RA on the present day.

1.2 – Iguratimod

Iguratimod (IGU), also referred to as T-614, is a synthetic non-steroidal anti-inflammatory disease modifying anti-rheumatic drug, that was developed in Japan. It was first introduced on the market in 2011, and it is currently approved for treatment of RA in China, Japan, and India. IGU has shown good efficacy and safety both in monotherapy and combinator therapy with methotrexate. [6–13] Positive results have also been reported with other rheumatic diseases, such as Sjögren's syndrome, ankylosing spondylitis and lupus nephritis.[12,14–16]

IGU presents a good alternative to inadequate response in treatment with other DMARDs. However, larger scale data is still in demand. The effects of age, sex, and ethnicity (among other heterogeneity factors) in continued treatment with IGU are still, to this day, a subject of study. Moreover, the majority of information available on this compound is clinical related, and very little is known about IGU's solid state and thermodynamics.[17]

1.2.1 – Pharmacodynamics: understanding IGU's mechanism of action

Pharmacodynamics is the study of the drug's effects on the human body. Understanding the biochemical action of a compound on the body, as well as the molecular and cellular processes involved in the target pathology, is extremely important, as it allows improving the development of drugs and clinical studies. A thorough insight on a drug's pharmacodynamics also permits predicting possible synergetic and toxic drug to drug interactions.

Although its biologic target is still unknown, the mechanism of action of IGU has been a widely studied subject over the past decade.[6,8,10,11,14,15,17–20] It can be separated in three major categories: anti-inflammatory; immunomodulatory; and osteoprotective. These are hereinafter summarized.

The Nuclear Factor Kappa-light-chain-enhancer of Activated B Cells (NF-κB) is a protein complex of major importance in gene expression. Upon activation, it modulates the transcription of genes, particularly those for pro-inflammatory cytokines. Therefore, NF-kB plays a key role in the pathogenesis of inflammatory diseases, such as RA.[21] IGU was found to interfere with NF-κB translocation to the nucleus by both Th17 and TNF-α signalling pathways, hindering the production of pro-inflammatory cytokines, such as IL-6, IL-8 and TNF. In addition, IGU can inhibit the activity of macrophage migration inhibitory factor (MIF), preventing MIF-induced pro-inflammatory effects.[14,21,22]

T cells have been found to play an important role in RA's autoimmune response. IGU regulates immune balance in patients with RA by significantly reducing the levels of Th1, Th17 and Tfh cells, while increasing the levels of cytokines and transcription factors

associated with Treg cells, a subpopulation of T cells that supresses immune response.[14,23] Moreover, IGU reduces immunoglobulin production and secretion, without affecting B cell proliferation.[14,24]

IGU's osteoprotective mechanism was found to unfold by increasing the expression of Sp7, Dlx5, and p38, proteins crucial in the differentiation of osteoblasts, which are bone-forming cells. Furthermore, IGU was found to protect osteocyte integrity by reducing NF-κB activation.[14,18]

Studies aiming to identify IGU's biological target are still ongoing. Once found, its mechanisms of action should become clearer, also being expected an increase in its clinical application.

1.3 – Drug pharmacokinetics

Drug discovery and development is an expensive and time-consuming process, which follows a series of strict rules, imposed by the regulating authorities to ensure the final product is effective, while also being safe. Since new drugs are continually required by the healthcare systems to address unmet medical needs, this procedure is of utmost importance. Even though there have been several technological advances in the pharmaceutical industry over the years, there are still many diseases without a cure, and many others with suboptimal treatment options, which inevitably cripple patients quality of life.

Nowadays, the ideal drug candidate must combine efficacy with good physicochemical and pharmacokinetic properties, in order to be accepted in what is a highly competitive market. The pharmacokinetics of an active pharmaceutical ingredient (API) is defined as how the body responds after the administration, and how that response affects the API, in terms of the absorption, distribution, metabolism and elimination. Toxicity is also a very determining factor to consider, hence why these principles are commonly represented in literature by the acronym ADMET.

One of the most important pharmacokinetic parameters is the bioavailability, this being the fraction of API that enters systemic circulation, in an unmetabolized form, thereafter reaching the desired biological target. Absorption, the transport of the drug from the administration site to the circulatory system, plays a determining role in the bioavailability of drugs administered orally, as only the absorbed fraction can exert the therapeutic effect. This, however, is not applied to intravenous administrations, because in these the drug is directly transferred to the bloodstream, and no absorption is required. The absorption process has three main limiting steps: dissolution, permeability to the intestinal mucosa, and presystemic metabolism (**FIG. 2**). In particular, dissolution and permeation are two of the most frequently chosen targets in modern science drug development, and various methods for predicting, testing and improving these parameters are often employed. [25–27]

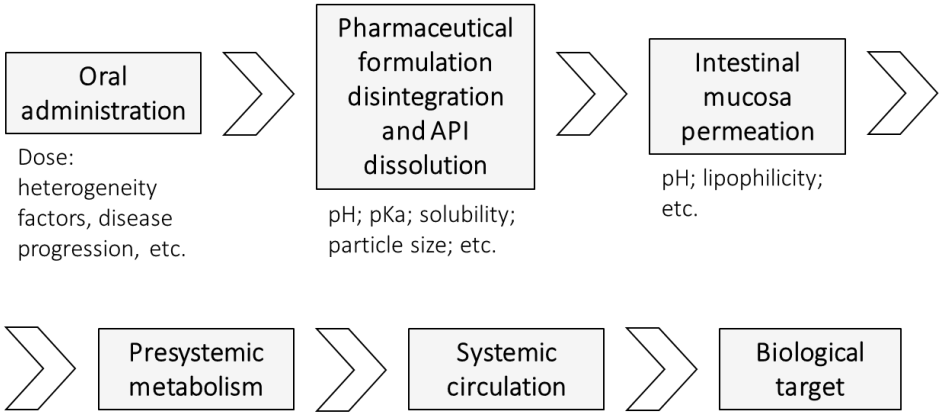

FIG. 2 – Simplified schematic representation of the absorption process of a drug.

1.3.1 – Biopharmaceutics Classification System

The Biopharmaceutics Classification System (BCS), represented in **FIG. 3**, is a simple, yet effective first indicator of bioavailability. It separates compounds according to their aqueous solubility and permeability, two determining parameters in initial formulation. It also allows for a direct correlation between dissolution and bioequivalence for class I compounds, for it is assumed that the entirety of the dissolved fraction will reach the bloodstream, since it is highly lipophilic.[28,29]

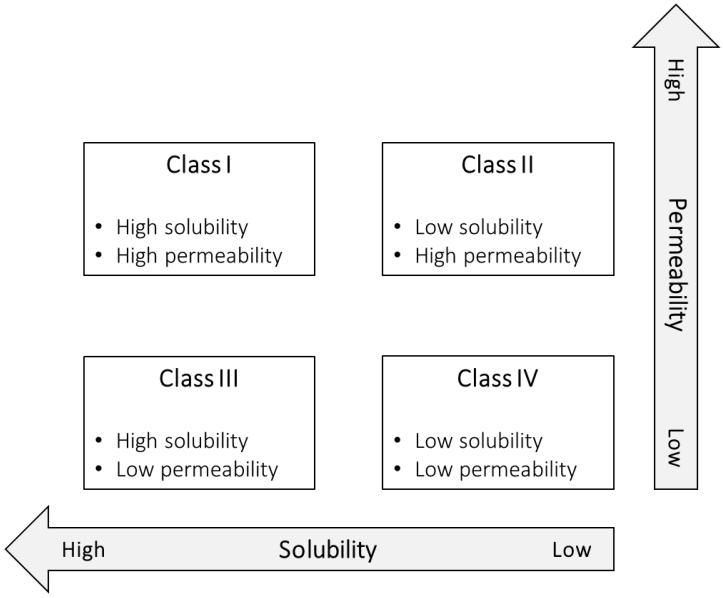

FIG. 3 – The biopharmaceutics classification system. Adapted from reference 29.

Poor water solubility is proving to be one of the most recurring problems with new drug-candidate compounds. It is estimated that approximately 90% of new chemical entities (NCEs) would be categorized as either class II or IV. Compounds belonging to one of

these two classes will requires higher doses and/or dosages in order for therapeutic effect to be observed, which increases the risk of toxicity coming from potential reactive metabolites of the unabsorbed portion. Although improving API low solubility and dissolution rates is a challenging obstacle to overcome, and can ultimately decide if a NCE will be able to reach the market, since it severely limits its bioavailability.[30]

1.4 – Solubility

Solubility is the maximum quantity of a substance which, at given temperature and pressure, can be completely dissolve in a defined amount of solvent. This parameter has increased importance is drug discovery, since only the dissolved fraction of the solute is able to cross biologic membranes, making this a limiting step in absorption.[31]
From a thermodynamics standpoint, for two phases in thermal and mechanical equilibrium (uniform temperature (T) and pressure (p)), the chemical potential (μ) of a compound in the two phases is equal, as given by equation (1):

$$\mu \text{ (phase A)} = \mu \text{ (phase B)} \quad (1)$$

In complete thermodynamical equilibrium, the chemical potential corresponds to the partial molar Gibbs energy. When the two phases are solid and liquid, the most considered in solid state chemistry, the chemical potential can be represented by equation (2):

$$\mu^{\text{liquid}} = \mu^{\text{solid}} + RT\ln(a) \quad (2)$$

where μ^{solid} is the chemical potential of the solute in the reference state; R is the gas constant; T is the temperature, expressed in Kelvin; and a is the activity of the solute in the solution, which is defined as the product of the molar fraction (χ) and the activity coefficient (γ), a thermodynamics concept used to account for deviations of a compound in solution from the ideal behaviour.[31,32]

1.5 – Solid formulations to increase solubility

The solubility of a drug is intrinsically related with its solid form. Some drug formulations aim to increase dissolution rates, without altering the drug's physicochemical properties, in order to ensure it retains its pharmacological effect. Solid state chemistry offers a wide variety of strategies for solubility enhancement (**FIG. 4**). Polymorphs, cocrystals, solvates, eutectics, amorphous and coamorphous were studied in the present work as alternative formulations over the pure API, to increase IGU's water solubility.

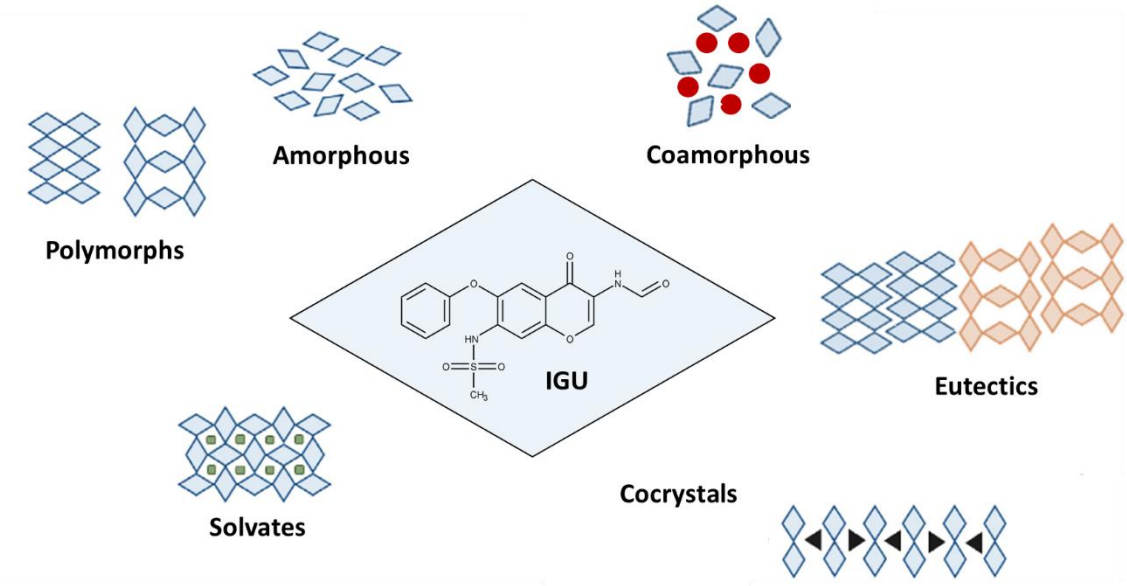

FIG. 4 – IGU solid formulations landscape in the present work.

1.5.1 – Polymorphs

A chemical substance can exist in different structural forms. These are known as polymorphs, crystalline supramolecular structures with unique molecular conformations and packing in the crystal lattice. Although being identical in chemical content (formed by the same molecules), polymorphic forms have distinct physical and chemical properties amongst each other, due to the presence of different intramolecular interactions, such as hydrogen bonds and van der Waals. These comprise stability, melting point, solubility, and even taste and smell, together with many other thermodynamical, spectroscopic, kinetic, and mechanical properties. As such, the pharmaceutical interest highly varies between different forms, the more stable and soluble being notably more appealing.

Polymorphs can exhibit a monotropic or enantiotropic relationship. In cases where two (or more) polymorphs are stable, over different temperature ranges (and constant pressure), these are said to be enantiotropes. However, if only one of them is stable, regardless of temperature and pressure, they are considered monotropes. In accordance with the phase equilibrium equation (1), spontaneous transformation from polymorphic forms A to B occurs when, at a certain temperature, $G_B < G_A$ (**FIG. 5**).[31,33–36] Sulphonamide drugs, such as IGU, have a predisposition towards crystalline polymorphism and solvate formation, due to their multiple hydrogen bond donor and acceptor groups, which makes them an interesting object of study.[37]

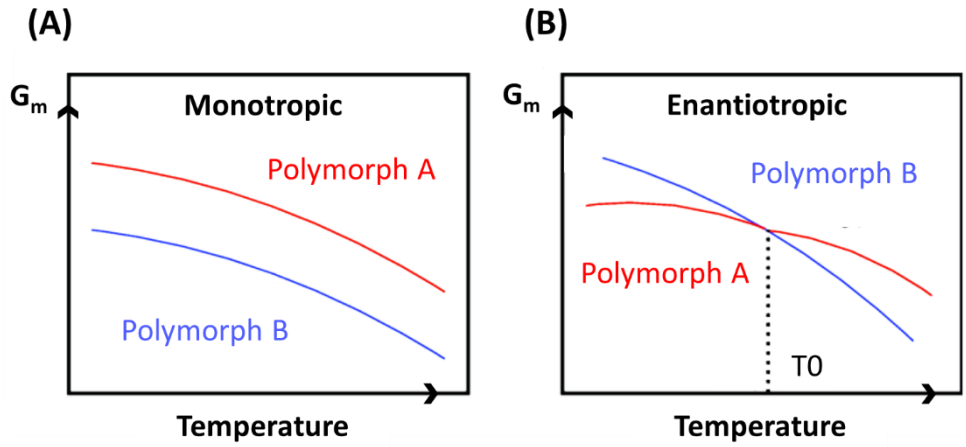

FIG. 5 – Gibbs energy diagrams, as a function of temperature, for the monotropic (**A**) and enantiotropic (**B**) relationship. T0 corresponds to the transition temperature.

1.5.2 – Cocrystals

Cocrystals are neutral single-phase materials, with supramolecular crystalline structures consisting of one (or more) API, and a coformer, typically in well-defined stoichiometric ratio. Moreover, cocrystals with different stoichiometries can be formed with the same coformer. They are stabilized by non-covalent and non-ionic intermolecular API-API, coformer-coformer, and API-coformer interactions (hydrogen bonds and van de Waals), and are solid when pure at ambient temperature and pressure. These solid forms are conferred unique physicochemical properties, such as solubility, dissolution profile, pharmacokinetics, and stability, which opens a possibility for improvements over its pure starting compounds, without altering their pharmacological nature.[37–41] Cocrystals have been extensively used as a means to increase dissolution rates, with some already on the market, and several others in clinical trials and registration phase.[42]

Coformers do not affect the pharmacological activity of an API. Thus, selection is based both on the API characteristics aimed to be enhanced, and the coformer' properties. Typically chosen coformers are both highly water soluble, and capable of forming hydrogen bonds. The coformer safety profile is also very important, as it must be in accordance with GRAS (generally regarded as safe) or other safe-for-consumption guidelines in order to be accepted on the market. Highly soluble vitamins, such as nicotinamide, are frequently used as coformers, as they are generally acknowledged as safe for consumption. Other pyridinecarboxamide isomers have also been reported as effective coformers.[43–47]

Other APIs can also be used as coformers. In this case, the final product is called drug-drug cocrystal, or simply dual-drug. Dual-drugs are an emerging strategy in drug development. They allow the combination of compounds previously used in combinatory therapy in a single solid form, while boosting their synergetic effects, and

enhancing their separate physicochemical properties, such as water solubility, and, consequently, bioavailability.[48–50]

There are numerous methods for preparing cocrystals. These can be categorized as solid-state or solution based.[40] The present work focuses on mechanochemistry, a solvent-free mechanical grinding method[51], for cocrystal formation, more specifically neat grinding (NG) and liquid-assisted grinding (LAG). Although being green chemistry friendly, and having shown good results in cocrystal obtention across several studies, mechanochemical methods cannot fully replace solution based techniques, as these can more consistently produce single crystals, which are determining for crystalline structure solving.[40,47,52]

1.5.3 – Solvates

Solvates are solid forms in which solvent molecule becomes "trapped" within the host molecule's crystal lattice. Similar to cocrystals, they are stabilized by hydrogen bond and van der Waals intermolecular interactions, and can alter physical and chemical characteristics of the API, thus modifying their pharmaceutical performance. Hydrates are a special kind of solvates, in which the solvent is water. There are many examples of pharmaceutical compounds commercialized in hydrated and dihydrated form, these showing very distinct properties when compared with the respective anhydrous (water-free) forms.[53–55]

Solvated form's stability is, much like polymorphs, temperature and pressure dependent. Overtime, metastable solvates can go through a spontaneous desolvation process, which involves solvent exit, followed by crystallization (three-dimensional molecular rearrangement).

Apart from being stable, solvates destined for commercial practice must also obey the guidelines for residual solvents, such as the ICH guideline Q3C on residual solvents in pharmaceuticals, as they are generally considered to be impurities. These two factors, however, together with non-ideal physicochemical property modifications upon solvate formation with an API (such as decreased dissolution rates), severely limits the pharmaceutical applicability of these solid forms, for which they are mostly addressed for characterization purposes.[53,54]

1.5.4 – Amorphous

Solid compounds can be classified as either crystalline or amorphous, depending on the order degree found on their molecular structure. Amorphous solids lack long-range order between molecules, this meaning molecules are not organized in a well-defined lattice.

Amorphous formulations represent one of the most direct approaches to increase solubility, and are commonly used with poorly water-soluble drugs to improve their bioavailability. This is explained by the loss of long-range order between molecules, which results in higher Gibbs energy and enhanced reactivity, thus increasing dissolution rates. However, amorphous systems are unstable, and recrystallization often occurs due to a thermodynamic drive to return to equilibrium - the lower energy state (crystalline). For this reason, the stabilization of the amorphous form stands as the main obstacle to outcome in these types of formulations.[56–58]

Glasses are a special type of amorphous rigid materials, obtained by rapidly cooling melt compounds, to avoid crystallization. This process is known as supercooling, and has been deemed as a crucial factor for glass formation. Although the kinetics of crystal nucleation and growth from the liquid are known to be directly connected, the molecular intricacies of this phenomenon are yet to be fully understood.[59–61]

1.5.4.1 – Coamorphous

Coamorphous systems, like cocrystals, are solid forms comprised of a mixture of an API and a coformer. The API is amorphized with the coformer, to obtain a single amorphous phase, in a well-defined stoichiometric ratio, as represented in **FIG. 6**. Due to the characteristics of the amorphous nature, coamorphous have the potential to increase the dissolution rates of poorly water-soluble drugs.[62]

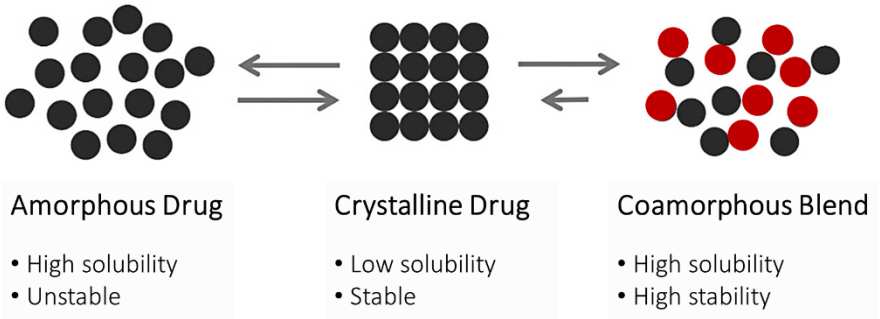

FIG. 6 – Schematic representation of crystalline and amorphous drugs, and coamorphous blends. Adapted from reference 61.

The development and stabilization of amorphous drug delivery systems has been a widely studied subject in pharmaceutics as a mean to improve aqueous solubility. Similar to amorphous solids, coamorphous tend to recrystallize after a certain period, which makes stabilization a crucial step for determining pharmaceutical potential.[62–64]

Coamorphous blends with and without molecular interactions are possible to obtain. The absence of evidence of API-coformer interactions, however, does not imply an

inferior performance over other interacting blends, as several studies demonstrated increases in solubility and dissolution rates with such coamorphous drugs.[65–67]

1.6 – Compounds used in solid form investigation with IGU

Solid state studies with IGU were conducted with six different compounds: leflunomide (LEF); sulfasalazine (SSZ); nicotinamide (NA); folic acid (FA); metoclopramide (MCP); and omeprazole (OPZ). These can be organized in three categories, according to the pharmacological purpose behind choosing them, as is shown in **FIG. 7**.

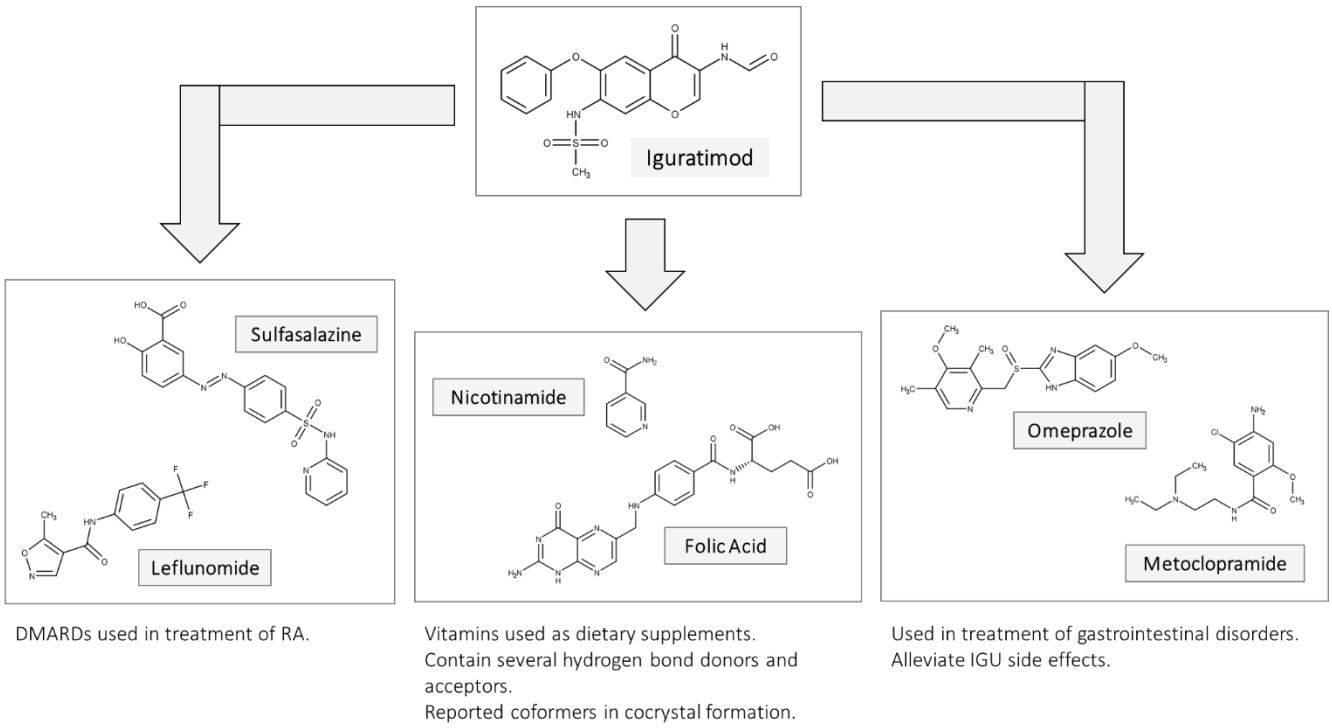

FIG. 7 – Schematic representation of the six compounds used in studies with IGU in the present work.

1.6.1 – Selection process of coformers

LEF and SSZ are DMARDs, both being used in modern clinical practice in the treatment of RA. Similar to IGU, these drugs have been used in monotherapy, but also in combinatory therapy with methotrexate.[68,69] Furthermore, both LEF and SSZ molecules have several hydrogen bond donors and acceptors, which raises their potential as coformers. LEF cocrystals have also been reported in published journals.[70] Dual-drug cocrystal and coamorphous formation was investigated with IGU, with the aim of obtaining a new API-API DMARD cocrystal, with enhanced physicochemical properties over the separate compounds.

NA and FA are vitamins. Even though the solubility of NA is far superior to that of FA,

both these compounds have been reported in cocrystal studies. Moreover, FA was found to have a synergetic effect with methotrexate in patient being treated for RA, by alleviating side-effects.[71] The added benefit of consumption safety was decisive in choosing them as coformers for investigation with IGU.[45,46,72]

MCP and OPZ were selected in order to target IGU's gastrointestinal side-effects. Possible drug-drug cocrystal formation could not only improve the bioavailability of IGU, but also alleviate one of most frequently occurring the adverse reactions associated with its treatment.[73,74]

1.7 - Biological membranes: insights on phospholipids

Biological membranes are of vital importance for the maintenance cell life. They are complex systems, composed of many types of lipids, proteins, and sugars. Aside from their structural role, they mediate a series of chemical and biochemical events, such as cell signalling, cell motility, and molecular traffic between the intracellular and extracellular compartments.[75,76]

Three different families of lipids can be found in biological membranes, these being phospholipids, glycolipids, and sterols (**FIG. 8**).

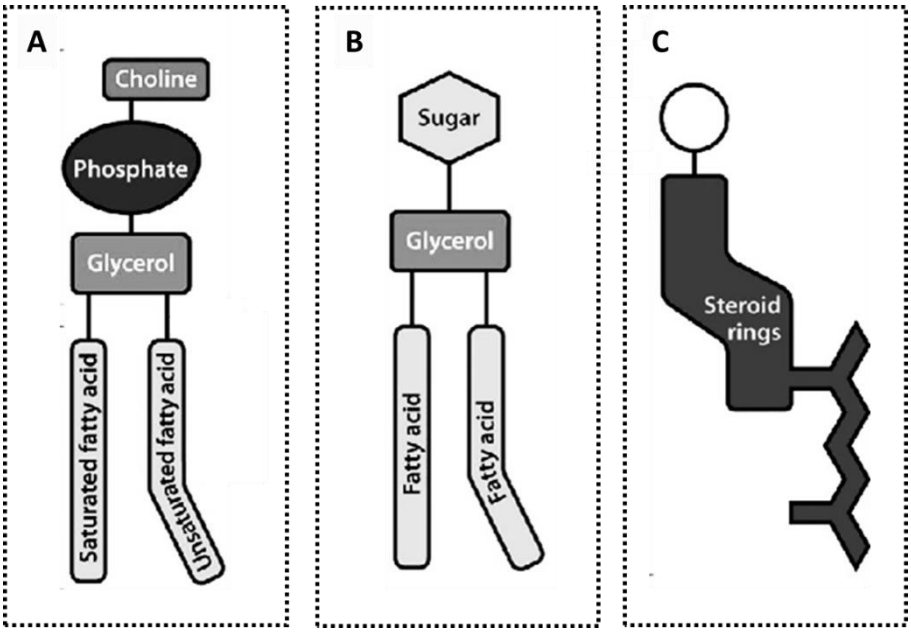

FIG. 8 – Schematic representation of the three families of lipids found in membranes: phospholipids (**A** – phosphatidylcholine), glycolipids (**B –** diacylglycerol glycolipid), and sterols (**C**). Adapted from reference 75.

Phospholipids, the most abundant in membranes, consist of two hydrophobic hydrocarbon "tails", connected to a hydrophilic "head" group. In aqueous environments, their amphipathic nature causes them to spontaneously form micelles or

bilayers, in which the polar “heads” face outward, and the non-polar “tails” face the centre, towards each other, in order to minimize their contact with water (**FIG. 9**).[75,77]

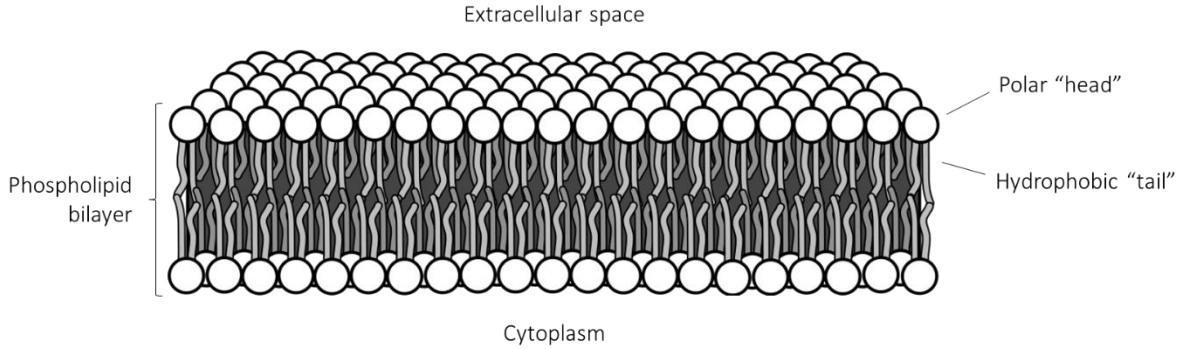

FIG. 9 – Simplified schematic representation of a phospholipid bilayer.

This phenomenon occurs due to what is known as the hydrophobic effect, a thermodynamic concept that describes the tendency of hydrophobic molecules to aggregate in aqueous solutions, and isolate themselves from water molecules. The aggregation results in a large increase in the entropy of the system, due to the break of the hydrogen bonds between the water molecules initially surrounding the hydrophobes, leading to an overall decrease in Gibbs energy. Additionally, non-covalent interactions, such as van der Waals interactions between hydrocarbon chains, and also electrostatic and hydrogen bond interactions, between the polar “head” groups and the interfacial water molecules, help further stabilise the membrane.[77,78]

Phosphatidylcholines are zwitterionic phospholipids which have a hydrophilic “head” group composed of phosphate and choline. They are the major phospholipids in biologic membranes. Other commonly found phospholipids, like phosphatidylethanolamines, phosphatidylserines, and sphingomyelins, differ on the composition of their “head” group, and the length and unsaturation degree of their hydrocarbon chains.

Unlike phosphatidylcholines, not all phospholipids are neutrally charge. Phosphatidylserines and phosphatidic acid are two examples of phospholipids with an overall negative charge (**FIG. 10**).[75,79] There are, however, no natural overall positively charged lipids.

The hydrocarbon chains of phospholipids can be saturated (only C-C bonds), monosaturated (one C=C bond) or polyunsaturated (two to six C=C bonds). The unsaturation degree affects, amongst other aspects, the lipid’s transition temperature (T_m), this being the transition between the more ordered gel phase, to the more fluid liquid phase.[80] A single C=C bond causes the hydrocarbon “tail” to bend, which impacts lipid packing in the bilayer, allowing adjacent lipid’s chains to be more flexible. This is one of the reasons why 1-palmitoyl-2-oleoyl-sn-glycero-3-phosphocholine (POPC),

which has a transition temperature of -2 ^{o}C [81], is so commonly used in mimetic membrane models, since biological membranes are often found in fluid liquid phase.[82]

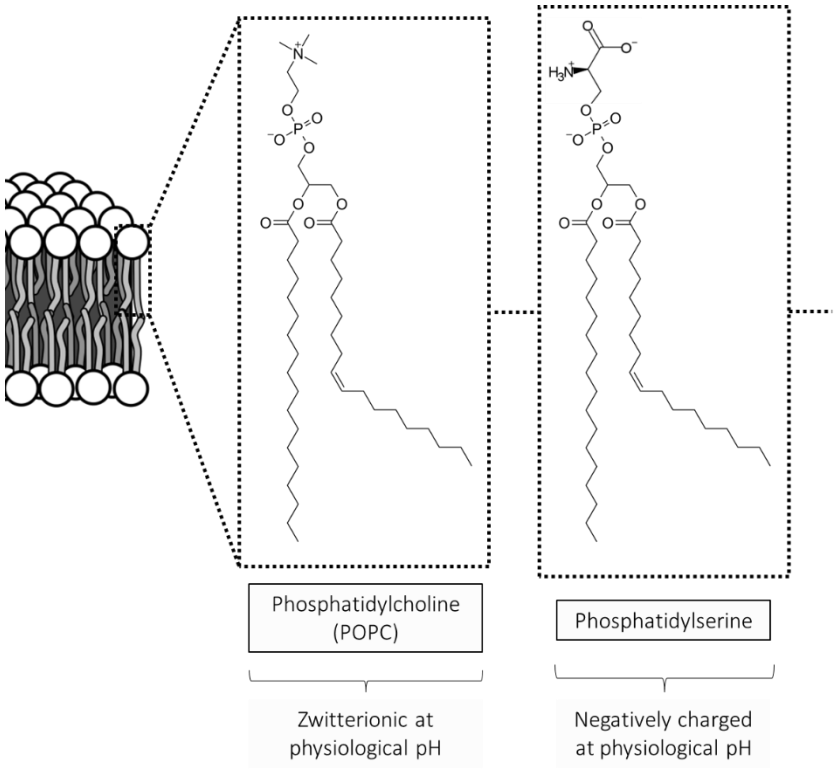

FIG. 10 – Schematic and molecular structure of two phospholipids with different overall charges at physiological pH.

1.7.1 – Partitioning and permeation studies

The biological membrane's selective permeability often presents a challenge in drug design. Although there are several different mechanisms of permeation, drug-like compounds often cross lipidic membranes by passive diffusion. Those who cannot efficiently pass through these barriers will have their bioavailability compromised, due to the inability to reach the therapeutic target.[83] Thus, finding consistent and reliable methods for predicting permeability across biological barriers is vital in early stages of drug development and testing.

In this work POPC, a very abundant phospholipid in animal membranes[84], was used to create of large unilamellar vesicles (LUVs) for evaluating IGU's permeation performance, ultimately aiming to calculate its permeation rate. POPC was also used in lipid partition studies, together with dimethyldioctadecylammonium bromide (DDAB), a positively charged surfactant that is able to form cationic vesicles in solution.[85] Unlike POPC, DDAB is not a constituent of biological membranes, and does not occur naturally. **FIG. 11** shows the molecular structure of POPC and DDAB.

Partition experiments are often used to predict a compound's lipophilicity, the primary result being the partition coefficient.[86,87] Both experiments used fluorescence spectroscopy as the main characterization technique for IGU.

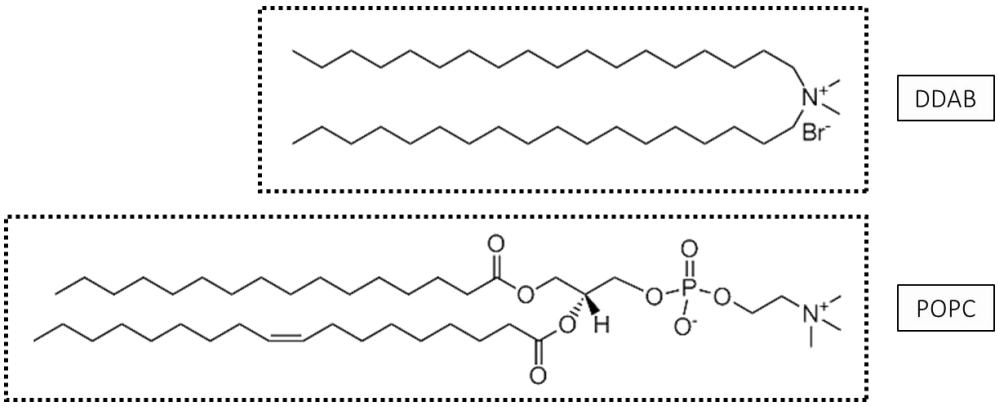

FIG. 11 – Molecular structure of POPC and DDAB.

1.8 – Objectives

The scarcity of information about IGU in literature makes this compound a very interesting subject for study. Moreover, the fact it is currently only utilized for clinical treatment of RA in China, Japan and India, means that upcoming research may be the deciding factor for treatment approval in other countries.

In the present work, IGU is investigated in solid-state, with calorimetric and spectroscopic methods, and characterized in solution, to address missing information. Cocrystal, amorphous and coamorphous formulations are studied with LEF, SSZ, NA, FA, MCP and OPZ, with the objective of obtaining a new solid form with improved physicochemical properties. Solvated and hydrated forms are additionally reported, to complement the study.

Lipid interaction studies, based on a partition model, are conducted with POPC and DDAB, and permeation through POPC LUVs is also described, in order to evaluate IGU's lipophilicity.

2 - Materials and Methods

2.1 – Materials and equipment

The full list of the chemical materials used in the development of the present work is presented in **Table 1**.

Table 1 – Materials, and respective abbreviation, supplier, molecular mass, and purity.

Compound	Abbreviation	Supplier	M / $g \cdot mol^{-1}$	Purity / %
Iguratimod	IGU	BOC Sciences & AmBeed	374.37	99.8 % & 98.0 %
Leflunomide	LEF	Supelco	270.21	≥ 98 %
Folic acid	FA	Sigma-Aldrich	441.40	≥ 97 %
Nicotinamide	NA	Sigma-Aldrich	122.12	≥ 99.5 %
Sulfasalazine	SSZ	Sigma-Aldrich	398.39	98 - 101.5 %
Metoclopramide	MCP	AmBeed	299.79	99 %
Omeprazole	OPZ	TCI	345.42	> 98 %
Acetone	Ace	Fisher Chemical	58.08	≥ 99.8 %
Acetonitrile	ACN	Fisher Chemical	41.05	99.99 %
Ethyl Acetate	EtOAc	Fisher Chemical	88.11	99.97 %
Ethanol	EtOH	Fisher Chemical	46.07	99.8 %
Dichloromethane	DCM	LAB-SCAN	84.93	> 99.8 %
Dimethylformamide	DMF	Fisher Chemical	73.09	≥ 99.8 %
Dimethyl sulfoxide	DMSO	Merck	78.13	> 99.5 %
Sodium phosphate dibasic	Na_2HPO_4	Sigma-Aldrich	141.96	≥ 99 %
Sodium chloride	NaCl	BioXtra	58.44	≥ 99.5 %
Quinine Sulphate	QS	Sigma-Aldrich	746.91	≥ 99 %
1-palmitoyl-2-oleoyl-sn-glycero-3-phosphocholine	POPC	Avanti	760.0	> 99 %
Dimethyldidodecylammonium bromide	DDAB	Avanti	462.6	> 99 %
Triton X-100	TX-100	Fluka	602.79-646.86	-

Table 2 displays the list of equipment used in the development of the present work.

Table 2 – Equipment, and respective brand, model, and technique abbreviation.

Equipment	Technique Abbreviation	Brand	Model
Differential Scanning Calorimeter	DSC	Perkin Elmer	DSC 7 TAC 7/DX
Fourier Transform Infrared Spectrometer with Smart Orbit ATR module with a diamond crystal	FTIR-ATR	Thermo Scientific	Nicolet 380
Microscope	PLTM	Leica	DM RB
Camera	PLTM	Pixelink	PL-A662
Single Cell Calorimeter for imaging and spectroscopy	PLTM	Linkam	DSC600 LNP CI 94
Mixer Mill	LAG & NG	Retsch	MM 400
Benchtop powder X-ray diffraction instrument	XRPD	Rigaku	MiniFlex 600
Thermo-microbalance for Thermogravimetric Analysis coupled to a Differential Thermal Analysis detector	TG-DTA	Netzsch	TG 209 F3
Diffractometer for Single-crystal X-ray diffraction	SCXRD	Bruker-Nonius	Kappa Apex II CCD
Fluorescence Spectrometer	FS	Varian	Cary Eclipse
Ultraviolet–visible Spectrophotometer	UV-Vis	Thermo Spectronic	Unicam UV500
Multi-Mode Microplate Readers	Fl UV-Vis	Molecular Devices	SpectraMax iD5
Light Scattering System	DLS	Malvern Panalytical	Zetasizer Nano Series

2.2 – Sample preparation methods

2.2.1 – Mechanochemistry (LAG & NG)

Mechanochemistry is a synthesis technique which works by an externally induced mechanic energy, specifically by constant shaking vessels, at a controlled frequency, which in turn causes steel balls to repeatedly collide with the sample, inside the vessel. Ball milling was used as the prime technique for cocrystal, amorphous and coamorphous production.

Solid mixtures were prepared by liquid-assisted grinding (LAG), with EtOAc as the reaction enhancing solvent (1µL/10mg), or by neat grinding (NG), in 10 mL stainless steel

grinding vessels, using two 7 mm stainless steel balls, or in 10 mL zirconium oxide vessels, using nine 5 mm zirconium oxide balls. Samples with a total mass of 70 mg were grinded at 15 Hz or at 30 Hz, for 30 to 60 minutes, according to the desired results. Cocrystal studies were mostly performed with LAG, with low milling frequencies and times, while amorphous and coamorphous investigation was conducted with NG, with higher milling frequencies and times.

2.2.2 – Solvate investigation by solvent evaporation and by slurry

Solvates were prepared by dissolving the desired amount of IGU in a fixed amount of solvent (10 to 15 mL), with constant mixing, and without a heat source. After dissolution was observed, the solution was filtrated, and then transferred to a petri dish or beaker, which was covered and stored at ambient temperature. Storage in the fridge was also tested with more volatile solvents, such as DCM. Samples were ready over a period of two weeks (except with PBS and DMSO), after the solid crystalized and dried, following solvent evaporation.

An attempt at replicating IGU's hydrate formation (which had been previously obtained in a different study[46]) was conducted with slurry chemistry. Supersaturated solutions were prepared with 20 to 50 mg of IGU and 1 to 2 mL of PBS, and maintained at 25 ^{o}C for 2 to 3 days, while being constantly stirred with a magnet. Resultant mud-like sample was analysed by XRPD.

2.3 – Calorimetric techniques

2.3.1 – Differential scanning calorimetry (DSC)

DSC was used to investigate the thermal behaviour of the solids obtained in the present work. A power compensation calorimeter, with an intracooler cooling unit adjusted to - 20 ^{o}C (ethyleneglycol-water, 1:1 (v/v)), was used. A N_2 purge, with a flow rate of 20 mL/min, was also used. Samples weighting 0.5 to 3 mg were prepared in 30 to 50 µL aluminium pans, and perforated pans were occasionally used. Scanning rates from β = 5 ^{o}C · min^{-1} to β = 100 ^{o}C · min^{-1}, with β = 10 ^{o}C · min^{-1} being the most commonly used.

2.3.2 – Thermogravimetric analysis coupled with a differential thermal analysis detector (TG-DTA)

TG-DTA was used as a complementary calorimetric technique to DSC, as it allows a sharper analysis of desolvation and degradation processes.
Samples weighting 2 to 10 mg were transferred to an alumina crucible, and were then heated at β = 10 ^{o}C · min^{-1} in air atmosphere. Resulting lost mass (%) and temperature variation from the reference (ΔT) curves, as a function of temperature, where used to identify solvent exit and sample degradation steps, and solid-solid transitions and fusions (respectively).

2.3.3 – Polarized light thermal microscopy (PLTM)

PLTM is a technique that allows direct observation of sample alterations during the heating process through imaging. Structural modifications, phase transitions and crystal habits are some of the information possible to obtain with this method.
Small samples were accommodated in the centre of the glass sample pans, which were then covered, and placed in the calorimeter unit. Scanning rates varying from β = 10 ^{o}C · min^{-1} to β = 20 ^{o}C · min^{-1} were used. Imagens were collected with an ampliation of 200x.

2.4 – Spectroscopic techniques

FTIR-ATR and XRPD allow for an easy distinction between different solid forms. However, a determined compound can only be categorised as polymorph or as solvate when these methods are complemented with calorimetric techniques, such as DSC, PLTM, and TG, which permit observing desolvation events.

2.4.1 – Fourier transform infrared spectroscopy with ATR module (FTIR-ATR)

FTIR-ATR is a technique based on the vibration of atoms in a molecule. It studies the interaction of electromagnetic radiation, with wavelengths from the infrared region, with the sample, being that for a certain molecule to absorb in this region, a dipole moment alteration caused by its vibrations must occur. This technique also allows studying cocrystal and coamorphous formulations, as the hydrogen bonds induce shifts in the infrared bands, caused by changes in the vibrational modes of the groups that are involved.

Solid's infrared spectra were collected by FTIR-ATR, using 32 scans and a resolution of 2 cm^{-1}. The attenuated total reflectance (ATR) module allows for an easy and practical sample manipulation, not requiring any preparation before analysis.

2.4.2 – X-ray powder diffraction (XRPD)

XRPD is a very useful technique for the characterization of solid formulations, namely pure APIs, cocrystals, amorphous and coamorphous. Moreover, it is particularly valuable in the study of amorphous forms. Due to the lack of a crystal lattice, fully amorphous compounds show no diffraction peaks. As such, the X-ray pattern is fully driven by short-range order, and will be composed by one or more halos, characteristic of the amorphous material.
Diffractograms were obtained with collection times of approximately 8 minutes, with a scanning range between 3 and 40 º, a scan rate of 5 º/min, and steps of 0.01 º. Zero diffraction silicon sample holders were used, which are specially design so that no diffraction occurs from them (and only from the sample). Samples were properly accommodated in the centre of the sample holder, to ensure good signal quality.

2.4.3 – Single-crystal x-ray diffraction (SCXRD)

SCXRD is a technique which provides information on molecular structure and arrangements in the three-dimensional space. It uses the diffraction that occurs when X-ray radiation is directed towards a single crystal. The measured intensities and angles of these diffracted x-ray beams are interpreted as a distribution of the electron density in 3-D space, allowing to determine the positions of each atom, and the overall molecular geometry of the molecule.
The equipment comprised a molybdenum anode, which transmits MoKα radiation (λ = 0.71013 Å). A detailed structural description of the IGU:DMF system was obtained with this method.

2.5 – IGU characterization in solution

Experimental calculation of the molar absorption coefficient (ε), ionization equilibrium constant (pK_a), and fluorescence quantum yield (ϕ) was achieved with the aid of ultraviolet-visible spectroscopy (UV-Vis) and fluorescence spectroscopy. This characterization was conducted as a means to address the lack of information on this molecule, as none of these parameters were found to be described in literature.

2.5.1 - Determination of the molar absorption coefficient (ε)

Three independent stock solutions were prepared, with 2.66 mg, 2.62 mg, and 2.54 mg of IGU, each in 1 mL of DMSO, and were named "266", "262" and "254", respectively. A first 100-fold dilution (*dil 1*) was made by collecting a 50 µL aliquot of stock and adding it to 4.95 mL of saline phosphate buffer (PBS) with 2% of DMSO. A subsequent 2-fold dilution (*dil 2*) was then made by removing 1 mL of *dil 1* and adding it to 1 mL of PBS with 2% DMSO. This process was repeated until five 2-fold dilutions (*dil 1*, *dil 2*, *dil 3*, *dil 4* and *dil 5*, corresponding to 100-, 200-, 400-, 800- and 1600-fold dilutions, respectively) were obtained from each stock in DMSO. The solutions were analysed by UV-Vis spectroscopy, in cuvettes with an optical path of 1 cm, and the maximum absorbance values were registered at 347 nm. These values were then plotted against the concentration of the respective solutions, and ε was calculated through the curve slopes, following Beer-Lambert's law.[88]

2.5.2 - Determination of the pK_a value

For this procedure, 1.25 mL of the "*dil 1*" solution used in **2.5.1** was collected, and then added to 18.75 mL of PBS with 2% DMSO, leading to a 1600-fold dilution from the stock in DMSO. The pH of this solution was then adjusted to 9, with NaOH. A titration was made in the pH range from 9 to 3, by adding small aliquots of HCl, and analysing the solution by UV-Vis and fluorescence spectroscopy between each addition. Concentration variations due to HCl addition were taken into consideration in the results' analysis.

2.5.3 - Determination of the fluorescence quantum yield (Φ_F)

The fluorescence quantum yield (Φ_F) of IGU was calculated relative to a standard with known Φ_F. In this case, quinine sulphate (QS) was used.[89] Knowing that samples with identical absorbance values at the excitation wavelength are absorbing equal amounts of photons, the Φ_F of IGU can be calculated from the ratio of the integrated fluorescence intensities, since it is indicative of the Φ_F ratio between the standard and the test samples.[90,91]

A QS solution was prepared by dissolving 2 mg of this compound in 5 mL of 0.5 M H_2SO_4, and subsequently diluting it, until the observed maximum absorbance was approximately 0.05. Using the same procedure an in **2.5.2**, two IGU solutions were prepared by preforming a 1600-fold dilution from a stock solution (with 2.59 mg of IGU

dissolved in 1 mL of DMSO) with PBS 2% DMSO. Afterwards, their pH value was adjusted respectively to 3 and to 9, and they were further diluted, so their absorbance at the desired excitation wavelengths (320 nm and 346 nm) matched with that of quinine sulphate, as visible in the UV-Vis spectra in **FIG. 12**.

The refractive indexes of the solvents (PBS for IGU and H_2SO_4 0.5M for QS) were both considered to be equal to the refractive index of PBS (1.34 [92]) while calculating Φ_F.

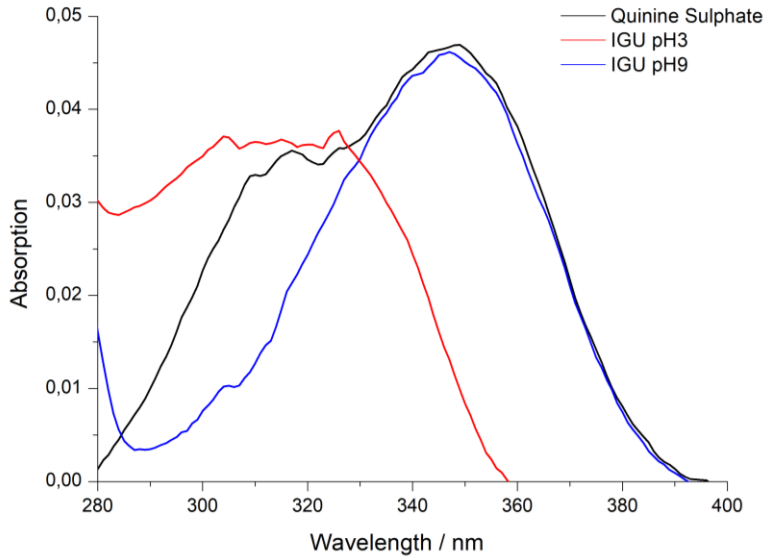

FIG. 12 – UV-Vis spectra of the quinine sulphate solution, and both IGU solutions, respectively at pH = 3 and at pH = 9.

2.6 – Studies of the interaction of IGU with POPC and POPC:DDAB membranes

For this experiment, 1-palmitoyl-2-oleoyl-sn-glycero-3-phosphocholine (POPC) was used alone, and in combination with dimethyldioctadecylammonium bromide (DDAB), in a POPC:DDAB molar ratio of 9:1. POPC is a widely abundant phospholipid in biomembranes, also being commonly used in biophysical studies with membrane models.[93–95] DDAB is a surfactant that forms cationic vesicles in solution. Unlike POPC, DDAB is not a component of biological membranes.[95,96]

From a stock solution with IGU (5.05 mg in 2mL of DMSO), 50 µL were initially diluted in 4.95 mL of PBS with 2% DMSO. This solution was named "*dil 0*". Three more dilutions were made with the same buffer, each with half the concentration of the original. These were named "*dil 1*", "*dil 2*" and "*dil 3*", being that only *dil 3*, with a concentration of 8.39×10^{-6} M, was used for these lipid interaction studies.

IGU's fluorescence was studied with successively higher concentrations of POPC and POPC:DDAB, ranging from 0 to 10 mM. A five-minute wait period was done after each addition, before reading the sample's fluorescence, and concentration variations due to

lipid addition were properly considered while analysing results. The experiment was conducted at 37 ^{o}C.

2.7 – Large unilamellar vesicles preparation

IGU's permeation through and partition to biomembranes was studied with large unilamellar vesicles (LUVs) made from POPC. These were prepared by extrusion.[97]

The required volume of a POPC solution, in a previously prepared azeotropic mixture of chloroform:methanol (87.4:12.6 (V:V)), with a concentration of 20 mM, was firstly measured and transferred to a glass tube. The solvent was evaporated under a stream of N_2, while heating the tube with a hot air flow, and constantly stirring in a vortex, producing a lipid film. The tube was placed in a desiccator, under vacuum, for one hour. After that, the vacuum pump was turned off, and the tube was left in the desiccator overnight. The POPC film was placed in a water bath at 37 ^{o}C, the minimum temperature being 10 ^{o}C above the lipid's transition temperature (T_m^{POPC} = -2 ^{o}C [81]), for five minutes.

A IGU solution was prepared beforehand, from a stock containing 4,02 mg in 1 mL of DMSO. A portion of 100 µL of this stock was added, under constant stirring in a vortex, to 4.9 mL of PBS buffer, which had been preheated to 37 ^{o}C. The solution was then once again placed in the bath at 37 ^{o}C, to prevent IGU from precipitating.

The POPC film was hydrated with the required volume of the IGU solution, and then left in the water bath for 30 minutes, with some occasional mixing, until all the lipid had been suspended.

A falcon tube was cleaned by freezing PBS buffer inside with liquid nitrogen, thawing, and then disposing of its content three consecutive times. The hydrated POPC suspension, now forming multilamellar vesicles (MLVs), was transferred to the clean falcon tube. Followed three steps of freezing, with liquid nitrogen, and thawing, in the water bath at 37 ^{o}C.

The extruder was prepared with two stacked polycarbonate filters, with 2.5 cm diameter and pores with 100 nm, and 5 mL of PBS were passed though. The lipid suspension was then passed though the extruder three times, agitating in a vortex and preforming a step of freeze and thaw after every passage. After this, ten additional passages were made, with mixing between each one.

2.8 – Permeation assay

The IGU+POPC solution from the above-described methodology contains IGU encapsulated inside the LUVs, and IGU in the external aqueous media. Since permeation is intended to occur from the internal to the external media, it is essential that the non-encapsulated IGU is separated from this solution (so that only the encapsulated IGU is characterized). To this end, size-exclusion chromatography was used, with 2 ml Zeba^{TM}

Spin Desalting Columns, from Thermo Scientific™. These columns contain a high-performance resin, that offers higher retention times to particles of smaller dimensions, allowing for an easy separation of bigger particles, such as LUVs.[98]

The gel resin of four columns was primarily resuspended and equilibrated with PBS. The IGU+POPC solution was then added to in two columns (500 mL in each one), and centrifuged at 1000 g, for two minutes. After that, 1 mL of PBS was added to each collection tube (containing only LUVs with encapsulated IGU), they were mixed, and then distributed equally through 10 eppendorfs (300 µL each). These were placed in a water bath at 37 ^{o}C, each one having a different incubation time, ranging from 0 to 60 minutes. During this time, IGU is permeating the LUVs. Once the target incubation time was reached, the eppendorfs were put in ice, to stop permeation.

The content of each eppendorf was passed through a Zeba™ Spin Desalting Column, by adding its content to the column and centrifugating at 1000 g. This was followed by a passage with 500 µL of PBS. Afterwards, 11 to 13 more passages with 1 mL of PBS were made, and the liquid from the collection tubes was stored between every passage. Once all had been collected, the samples were analysed by UV-Vis and fluorescence spectroscopy, in order to obtain the permeation profile of IGU through the LUVs over time. This process was also made with a IGU solution, in order to better understand the compound's column exit profile. For some samples, triton X-100 was added to the solutions, before absorption and fluorescence characterization, to break the lipid vesicles, thus minimising interference in the resultant spectra.

2.9 – Dynamic light scattering and zeta potential measurements

Dynamic light scattering (DLS) is a modern, non-invasive technique, used for determining the size of particles in a liquid dispersion. Such is accomplished by measuring their Brownian motion, the random movement of molecules associated with collisions with solvent molecules. By treating the particles as spheres, this allows to determine their hydrodynamic size. Smaller particles diffuse more quickly than bigger ones. Consequentially, when irradiating the dispersion with a laser, the scatter intensity correlation over time will decrease more rapidly the smaller the particles in the dispersion are. The obtained translational diffusion coefficient (D) is then used in the Stokes-Einstein equation to determine the particles size.[99,100] DLS was used to study IGU solutions with increasing concentrations, and to characterize the size distribution of the LUVs. Each sample was analysed in triplicate.

The zeta potential of POPC LUVs was also measured by DLS, and compared with and without the presence of IGU. Zeta potential, also know as electrokinetic potential, is the potential at the slipping plane, the interface between the moving particles of dispersant and the particles that eletrophoretically attached to the absorbed double layer, due to the electric field applied.[100]

3 - RESULTS AND DISCUSSION

3.1- IGU: calorimetric and spectroscopic study

3.1.1 - IGU's polymorphism

Two IGU polymorphs, forms I and II, were identified from commercial samples. Form II is converted into form I though an endothermic solid-solid transition during heating, at $T \sim 175$ °C, which is then followed by the fusion of form I, at $T = (238.7 \pm 0,6)$ °C, with a $\Delta_{fus}H = (40 \pm 2)$ kJ·mol^{-1}.[17,46] It was also found that, if the molten portion crystallizes at $T < 190$ °C, a third polymorph would form, which was designated as form III. Form III has a melting point of $T = 228$ °C. **FIG. 13** and **FIG. 14** (respectively) contain the FTIR-ATR spectra and XRPD diffractograms of the three mentioned IGU forms, while **FIG. 15** shows their DSC curves.[46]

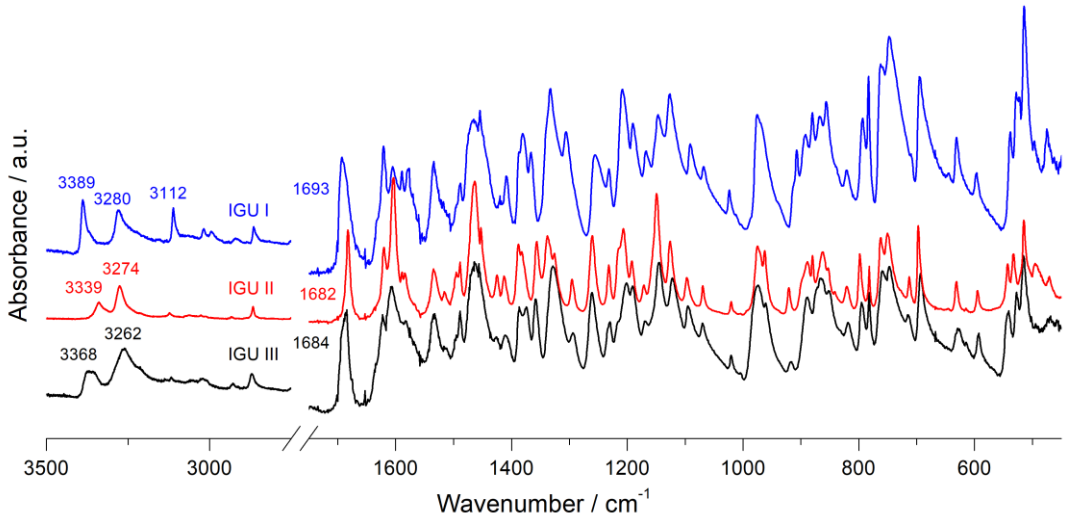

FIG. 13 – FTIR-ATR spectra of IGU's forms I, II and III.

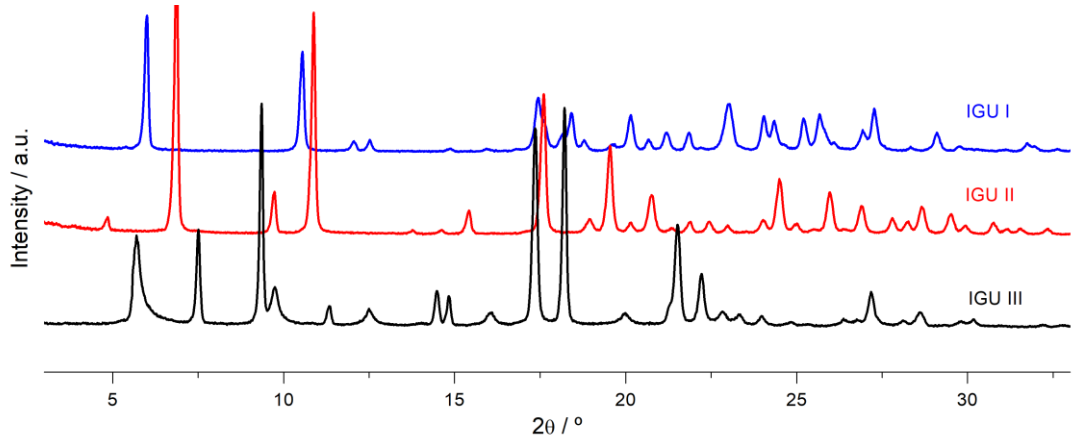

FIG. 14 – XRPD diffractograms of IGU's forms I, II and III.

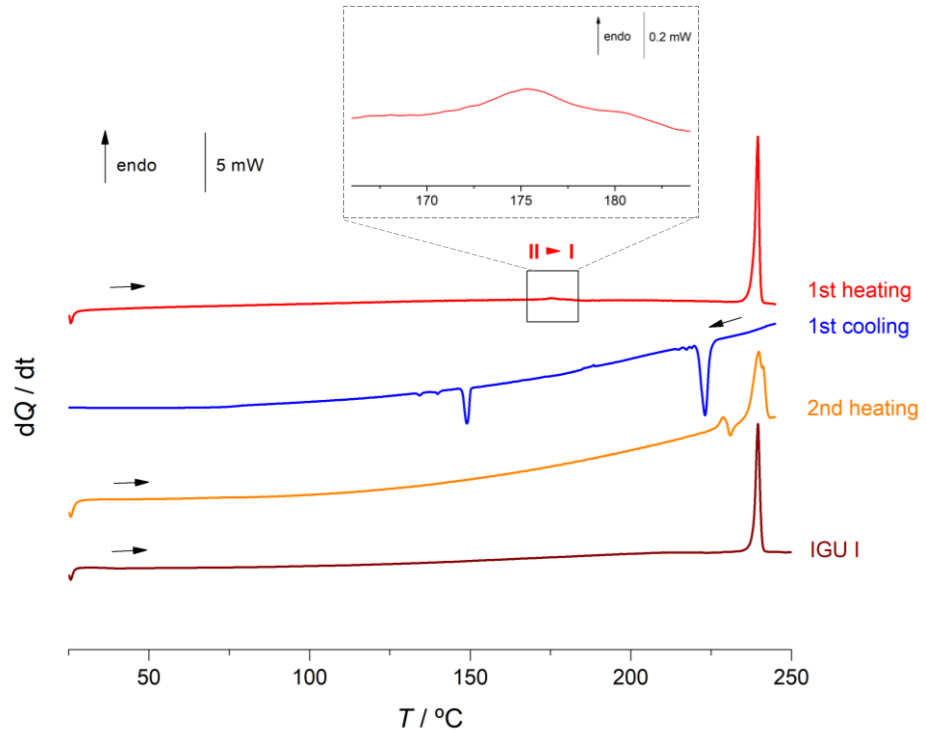

FIG. 15 – DSC curves of an IGU II sample, with m = 1.74 mg, and a IGU I sample, with m = 1.21 mg. The scanning rate used was β = |10| °C/min.

Polymorphs' I and II XRPD diffractograms were found to be in accordance with literature data (**FIG. Apdx1 - 1**).[17]

Form I converts into form II from storing at room temperature and pressure for an extended period. This supports the existence of an enantiotropic relationship between these two polymorphs. The I → II conversion was also observed by ball milling, and in crystallizations from different solvents, as is shown in **FIG. Apdx1 - 2**.

In some cases, metastable forms may endure a spontaneous polymorphic transition. Yet sometimes the energy barrier for that transition does not allow for it to happen instantaneously without an outside stimulus, whether it is temperature, pressure or mechanical related. Furthermore, the endothermic nature of the solid-solid transformation between forms II and I (**FIG. 15**) agrees with the heat transition rule, firstly briefed by Burger *et al.*, that associates endothermic transitions to enantiotropic relationships, and exothermic transitions to monotropic relationships.[33,34,36]

3.1.2 – IGU amorphization by neat grinding

IGU's amorphization was achieved with mechanochemistry, by neat grinding (NG) at 30 Hz for 60 minutes. Additionally, the performance of steel vessels was compared to zirconium vessels. **FIG. 16** shows a summary of the XRPD results obtained.

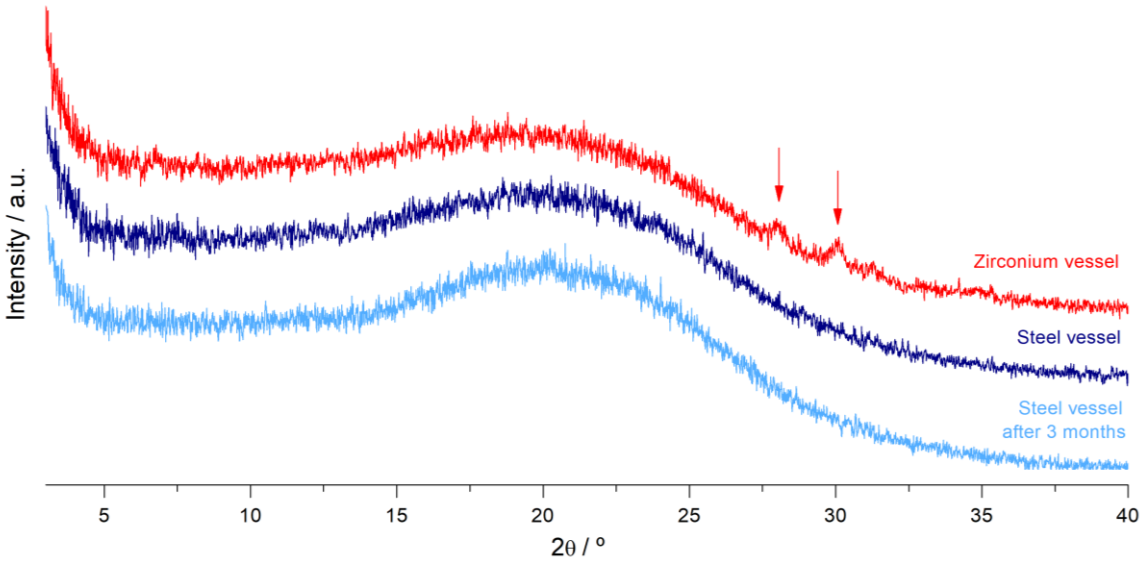

FIG. 16 – XRPD diffractogram of 100 mg IGU samples submitted to neat grinding at 30 Hz for 60 minutes in a zirconium and steel vessels.

Steel vessels performed better than zirconium vessels, since the second ones failed to fully turn the sample into an amorphous, under the same grinding frequency and time conditions. This is confirmed by the two peaks on the diffractogram of the solid grinded on the zirconium vessel (marked by arrows), which are proof that a fraction remains crystalline.

IGU's amorphous remained stable for 3 months, stored at ambient pressure and temperature (**FIG. 16**). However, a more thorough investigation of its stability and dissolution performance is necessary in order to evaluate its pharmaceutical potential over the crystalline counterpart.

3.1.3 – IGU's glass formation

Through a PLTM experiment with IGU, it was observed that, while cooling the melt at β = 20 °C/min, the crystallization process stopped, and a glass was formed. Upon reheating the sample, devitrification occurred at $T \sim 86$ °C, followed by a cold crystallization at $T \sim 110$ °C. The images captured are shown in **FIG. 17**.

A close analysis of the DSC curves for first cooling and second heating of a sample of IGU, also allows the detection of these events (**FIG. 18**). The thermogram shows both glass formation (1st cooling) and devitrification (2nd heating). There are, however, no signs of a cold crystallization, which was expected to start at $T \sim 110$ °C, according to what was observed by PLTM. Moreover, that is no certainty that this step even occurs in this case, as the sample could remain liquid during the entire heating process. This may be due to the distinct conditions in which the sample is accommodated in each of these techniques.

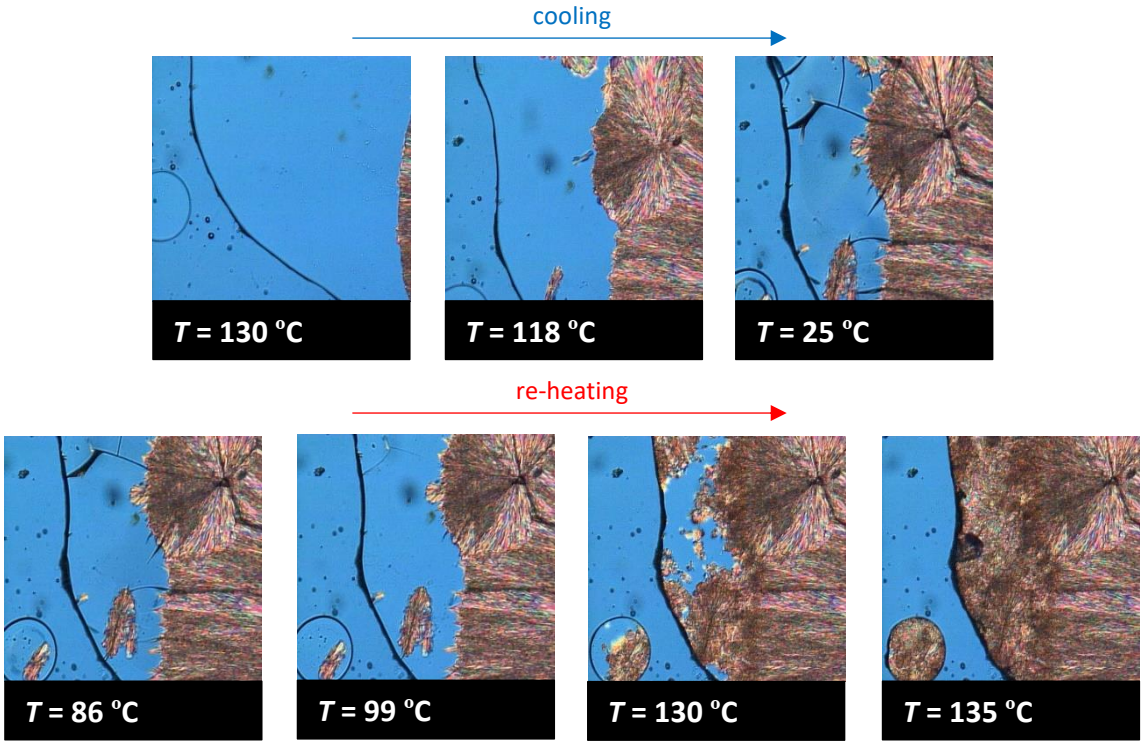

FIG. 17 – Images captured during a PLTM analysis of an IGU sample. β = |20| °C/min.

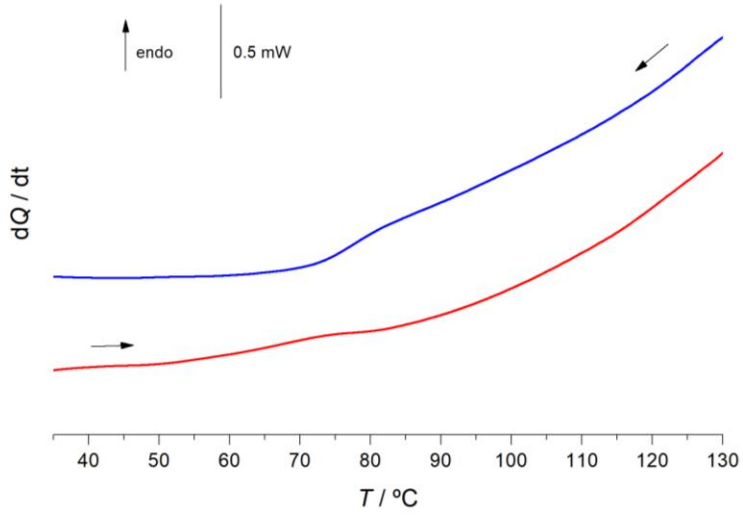

FIG. 18 – DSC curves of first cooling from the melt, and second heating of an IGU sample. β = 10 °C/min.

It was not possible to fully bypass crystallization with the conditions used, and increasing how fast the liquid was cooled produced no effect, as is shown in **FIG. 19.** However, no conclusions can be taken for cooling velocities above 100 °C/min, as they were not

tested. Finding an efficient method for obtaining and stabilizing the glass could be a valuable path for solving IGU's solubility issues in the future.

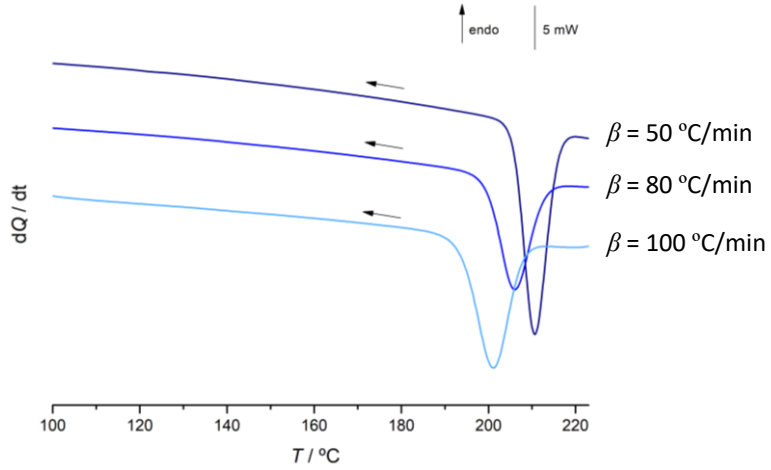

FIG. 19 – DSC curves of 3 IGU samples, cooled at successively higher rates.

3.1.4 – Crystallization from different solvents

Crystallization from solvent evaporation is often a method used to study polymorphism. Literature data refers that IGU forms solvates with EtOH, ACN, DMF, Ace and DCM.[17] Yet, there is no record of new polymorphs obtained through this method to this day. Hence, a more thorough investigation was made. **Table 3** shows the list of solvents used for this experiment.

Solvates with ACN, MeOH, MeOH:ACN and DMF were successfully obtained from solvent evaporation. **FIG. 20** and **FIG. 21**, respectively containing the FTIR-ATR spectra and XRPD diffractograms of the aforementioned samples, allow from a clear distinction between these and the three known IGU polymorphs.

Table 3 – Solvents used for the crystallization experiments, and results.

Solvent	Solvate	Polymorph
Ace	-	-
ACN	Y	-
MeOH	Y	-
EtOAc	-	-
MeOH:ACN	Y *	-
EtOAc:ACN	?	?
EtOH	-	-
DCM	?	?
DMF	Y	-
DMSO	-	?

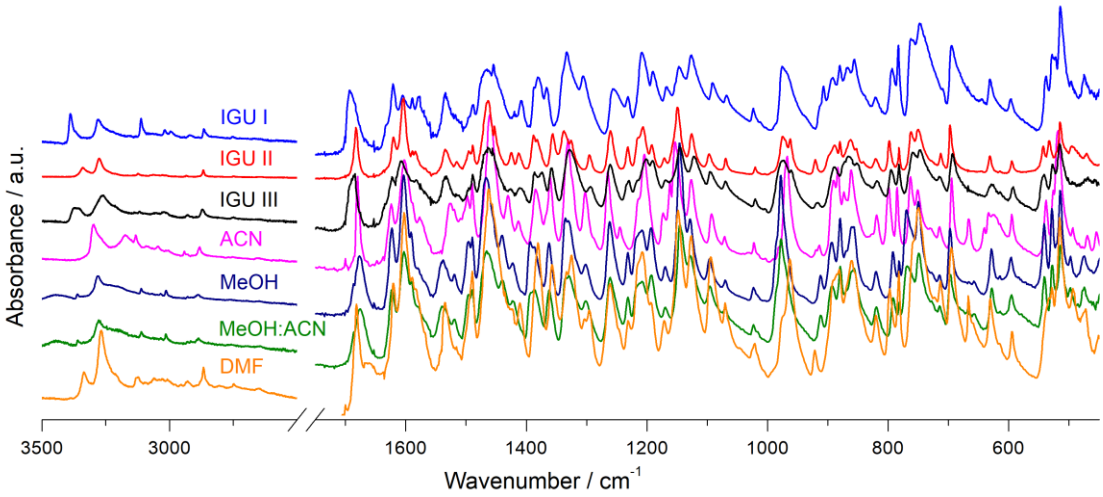

FIG. 20 – FTIR-ATR spectra of IGU's polymorphs and the solvates obtained from solvent evaporation.

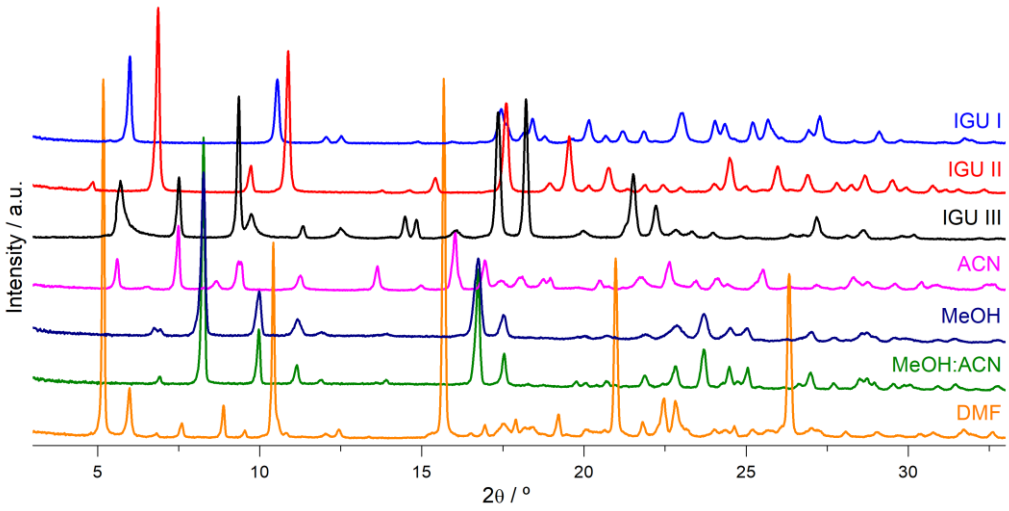

FIG. 21 – XRPD diffractogram of IGU's polymorphs and the solvates obtained from solvent evaporation.

The IGU:ACN and IGU:DMF solvates' XRPD diffractograms was found not to be in accordance with those of 梅林雨 *et al.* (**FIG. Apdx1 - 3**). However, on the mentioned paper, solvate formation is not proved, as no calorimetric techniques are used to analyse these samples. Furthermore, an accurate comparison between diffractograms was not possible, due to the poor quality of the ones published in the referred document (patent), for which the cause for this discrepancy was not found.[17]

As showed, both FTIR-ATR spectrum and XRPD diffractogram for the solvate obtained with MeOH are identical with those of MeOH:ACN. This suggests ACN is not incorporated in the crystal lattice, and the solvate is formed exclusively with MeOH. The inclusion of ACN may, however, prove useful in future attempts to replicate this solvate, as it dramatically increases IGU's solubility, which is practically insoluble in MeOH, while not affecting solvate formation.

The solids were analysed by DSC with perforated capsules, to allow monitoring of the solvate exit. The resulting curves clearly show the desolvation events for each solvate

(**FIG. 22**). This step could also be observed by TG (**FIG. 23**). The API-solvent molar ratios for each solvate were calculated from the mass lost upon each desolvation step.

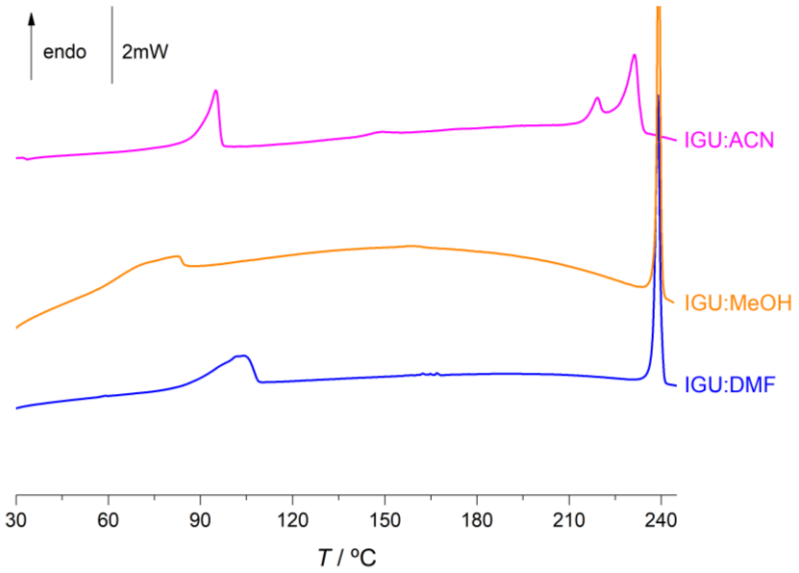

FIG. 22 – DSC curves of the IGU solvates obtained with ACN, MeOH and DMF. β = 10 °C/min.

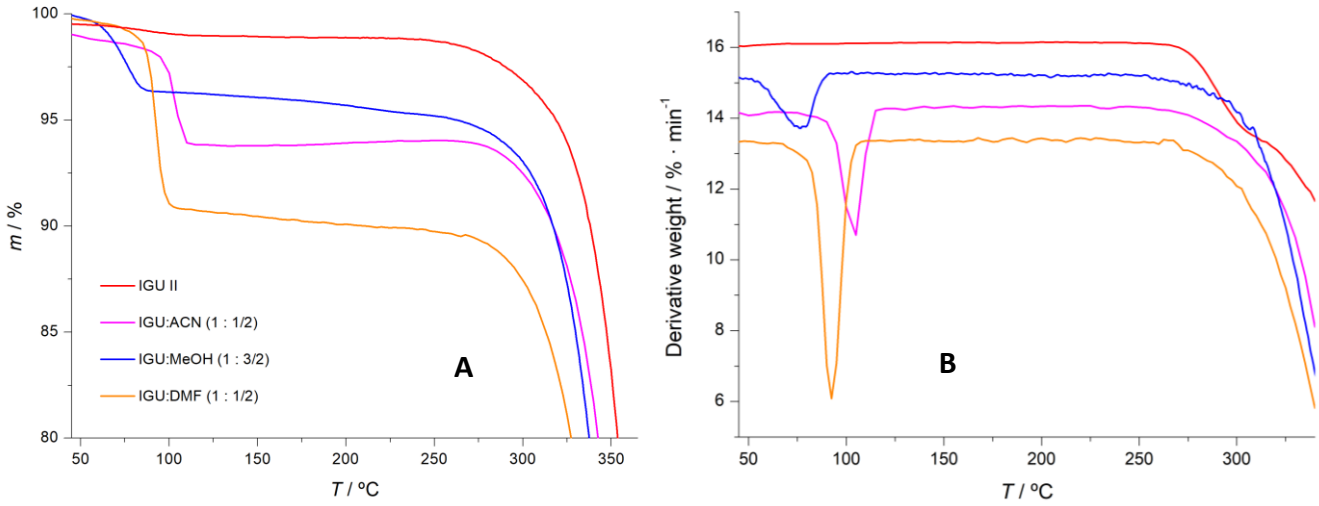

FIG. 23 – TG (**A**) and DTG (**B**) curves of IGU II and the solvates obtained. β = 10 °C/min.

The IGU:ACN curve in **FIG. 22** additionally suggests that IGU crystallized in a mixture of polymorphs after desolvation occurred. However, these were not investigated.

The DSC (**FIG. Apdx1 – 4-A**) and TG-DTA (**FIG. Apdx1 – 4-B**) curves for the solvates with MeOH do not match those of MeOH:ACN. Rather, in both cases MeOH shows a single desolvation step, whereas the curves for MeOH:ACN have two consecutive steps. A possible cause for this phenomenon may be that, at the time these analyses were made, some leftover ACN was still mixed with the sample. In this case, the second step ($T \sim 85$ °C) would be caused by its vaporization (being that this temperature is closely matched with ACN's literature vaporization temperature, which is 82 °C).

The binding energy (enthalpy of desolvation) was determined to quantify how strongly each solvent molecule is connected in the crystal lattice. This was accomplished by comparing the calculated energy (ΔH_{d}) with the enthalpy of vaporization of the respective solvents. Equation (3) was used:

$$\Delta H_{\mathrm{d}} = \mathrm{M_s} \cdot \left[\frac{\left(\Delta H_{\mathrm{d,exp}} \cdot 100\right)}{\Delta m_{\mathrm{d}}}\right] \quad (3)$$

where ΔH_{d} is the binding energy per mole of bonded solvent, $\mathrm{M_s}$ is the molecular mass of the solvent, $\Delta H_{\mathrm{d,exp}}$ is the experimental enthalpy of desolvation, and Δm_{d} is the percentage of mass lost in the desolvation process.[101–103]
The results are summarized in **Table 4**.

Table 4 – Thermal data of the desolvation of IGU's solvates.

IGU Solvate	Boiling Point of Pure Solvent/°C	Desolvation temperature/°C (DSC)		Mass Loss Upon Desolvation(%) (TG)	Enthalpy of Desolvation /J·g^{-1} (DSC)	Calculated Enthalpy of Desolvation (Binding Energy) /KJ·mol^{-1}	Enthalpy of Vaporization of Pure Solvent at 25 °C /KJ·mol^{-1}	Molar Ratio of IGU:Solvent
		Onset *T*/°C	Peak *T*/°C					
ACN	82	89.93	95.00	5.15	53.02	42.26	33.2	1:0.5
MeOH	64.7	53.79	72,43	12.23	64.45	16.88	38.3	1:1.5
DMF	153	90.51	104.07	8.94	68.27	55.81	46.9	1:0.5

Note: Values for the enthalpies of vaporization of pure solvents were collected from the NIST database.

The calculated binding energy values for IGU:ACN and IGU:DMF surpassed the enthalpies of vaporization of the respective solvents, suggesting the solvent molecules are tightly bound to the host lattice. In contrast, IGU:MeOH connections were found to be less strong, as the binding energy is lower than the enthalpy of vaporization of MeOH. Solvate formation was not observed with neither Ace, EtOAc, or EtOH, as concluded from the resultant FTIR-ATR spectra (**FIG. Apdx1 - 2**) and XRPD diffractograms (**FIG. Apdx1 - 5**), matching those from the starting IGU polymorph (form II).
From the solid crystallized in EtOAc:ACN, a crystal with a distinct crystal habit, that grew from the side of the container, revealed differences in the XRPD diffractogram (**FIG. Apdx1 - 6**), suggesting it had crystallized in a different form. But, since the sample was not enough to perform a DSC or a TG run, it's not possible to conclude weather this new form is a solvate or a polymorph.
The solid crystallized from DCM presented in a distinct FTIR-ATR spectra (**FIG. Apdx1 - 7-A**) and XRPD diffractogram from the three known IGU polymorphs (**FIG. Apdx1 - 7-B**). Although, similar to the previous case, there was not enough material

to perform a calorimetric analysis. Hence, and since no more replicates of this form could be produced in time, it's not possible to tell if it is a new IGU solvate or polymorphic form.

IGU's crystallization from DMSO resulted in a new solid form, as confirmed by analysing its XRPD diffractogram and comparing it with those of the IGU polymorphs and solvates (**FIG. Apdx1 - 8**). This solid was proved not to be a solvate, as no desolvation event was visible on the TG thermogram. The DTA curve additionally revealed an exothermic transition had occurred, at $T = 162$ °C, followed by a single fusion, at $T = 233$ °C (**FIG. 24**).

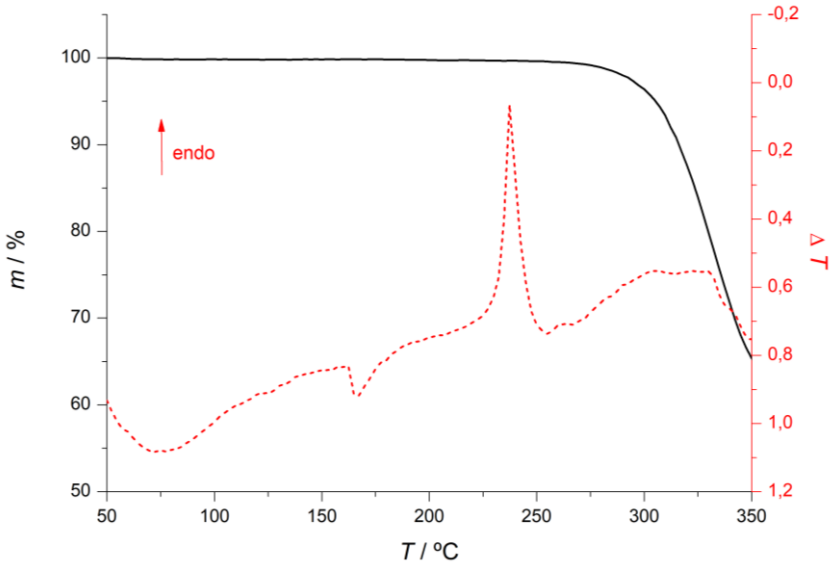

FIG. 24 – TG and DTA curves of the IGU crystallized from DMSO. β = 10 °C/min.

The results from the analysis of this sample by DSC (**FIG. 25**) did not reveal the previously observed exothermic transition. However, a crystallization was observed, followed by two overlapped fusion events, at $T \sim 230$ °C and $T \sim 235$ °C, which indicates the sample is mixture of polymorphic forms. Data from a second TG-DTA run (**FIG. Apdx1 - 9**) also revealed no solid-solid events on the DTA curve, which may be due to the technique's sensitivity, not allowing detection of this step in a polymorphic mixture. Moreover, the fusion onset was similar to the first observed by DSC, at $T = 230$ °C.

A PLTM experiment was also made (**FIG. Apdx1 - 10**). The sample remained unaltered until $T \sim 210$ °C. At this temperature, a long-lasting melting process began, which ended at $T \sim 240$ °C. This supports the presence of two distinct forms, as was observed by DSC. Since solvent exit was never observed in calorimetric studies, and the XRPD diffractogram showed clear differences from the know IGU forms, the IGU:DMSO solid can be concluded to be a new polymorph of IGU, the first obtained by solvent evaporation. Since this form was not obtained in its pure state (but rather in a mixture), it is not possible to accurately describe its thermal behaviour, as there were some discrepancies in results.

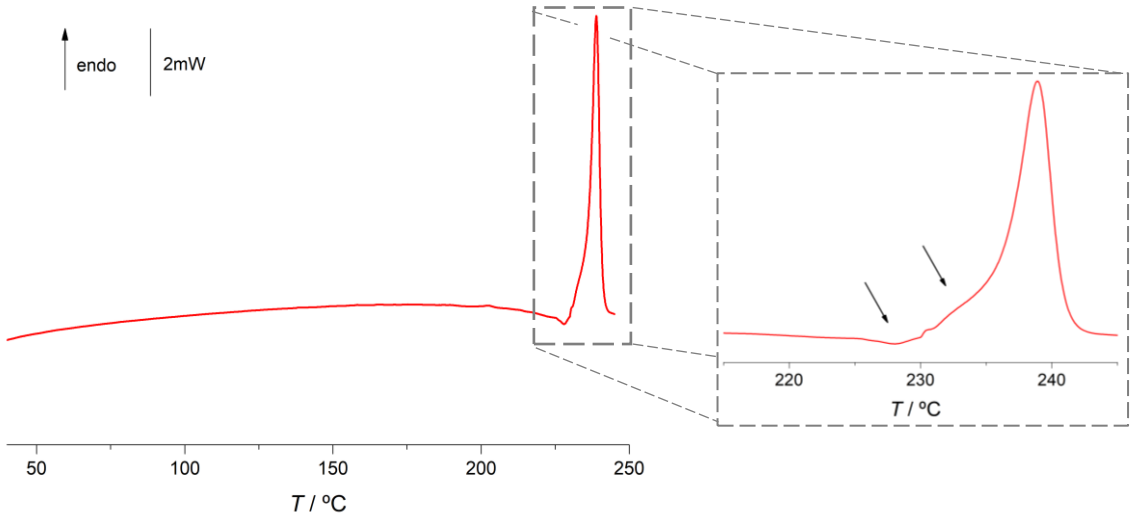

FIG. 25 – DSC curve of IGU crystallized from DMSO. β = 10 °C/min.

3.1.4.1 – IGU:DMF solvate crystal structure solving with SCXRD

From the evaporation of DMF, monocrystalline IGU:DMF crystals were obtained. The solvate was analysed by SCXRD, and its crystalline structure was solved. **FIG. 26** shows a representation of the solvate's unitary cell. The figure suggests a second IGU:DMF solvate was formed, in a 1:1 molar ratio, unlike the previously observed one, in a 1:0.5 molar ratio.

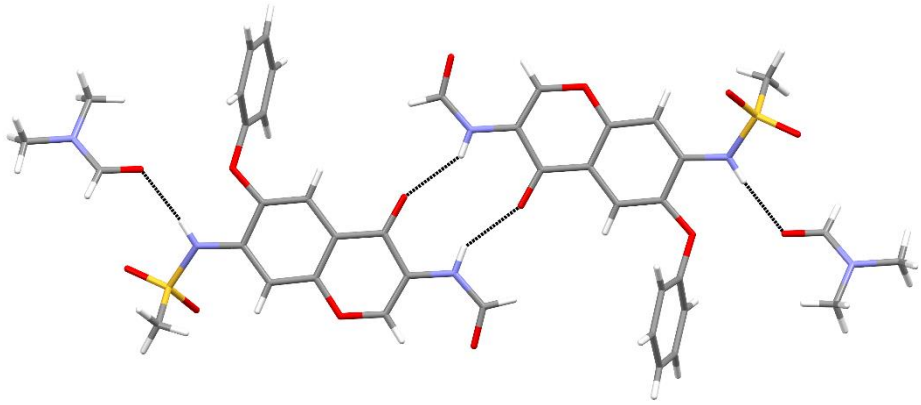

FIG. 26 – Hydrogen-bonded four-molecule unit of IGU:DMF, obtained by SCXRD. Hydrogen bonds are represented by dashed lines.

The crystal is described by a monoclinic system. The unitary cell's dimensions are a = 5.4149(4) Å, b = 11.7831(7) Å, and c = 16.9643(11) Å; the angle values α = 85.2130(10)°, β = 86.630(2)°, and γ = 79.035(3)°; and its volume is 1057.91(12) Å^3. The IGU molecules are linked to one another via N–H···O hydrogen bonds across an inversion centre. Each of them is also connected to a solvent molecule by a N–H···O hydrogen bond, thus forming hydrogen-bonded units consisting of four molecules, as visible in **FIG. 26**. These units are further interlinked with others, by weaker C–H···O hydrogen bonds and van

der Waals interactions. IGU molecules also present intramolecular N−H···O hydrogen bonds.

A 3 year later analysis of the IGU:DMF crystals revealed the sample had desolvated, and transformed into IGU's form I.

3.1.5 – Study of IGU's hydrate

In a previous study, a 1:1 cocrystal of IGU with nicotinamide (NA) was obtained with LAG. A dissolution test was preformed, to clarify whether the newly obtained solid form had improved solubility over the pure API. Although results showed no apparent increase in this parameter, it was discovered that both IGU and the IGU:NA co-crystal (which partially disassociated during the experiment) originated a 1:1 IGU hydrate while in contact with the phosphate buffer solution, which was proved by XRPD[46]and TG (**FIG. Apdx1 - 11**). A one-week later analysis revealed that the hydrate had evolved to the starting compound (IGU's form II).[46]

To replicate the hydrate obtained on the dissolution studies, three slurries were made, using IGU's forms I and II, and a saline phosphate buffer with pH = 8. The resultant solids were analysed by XRPD (**FIG. 27**).

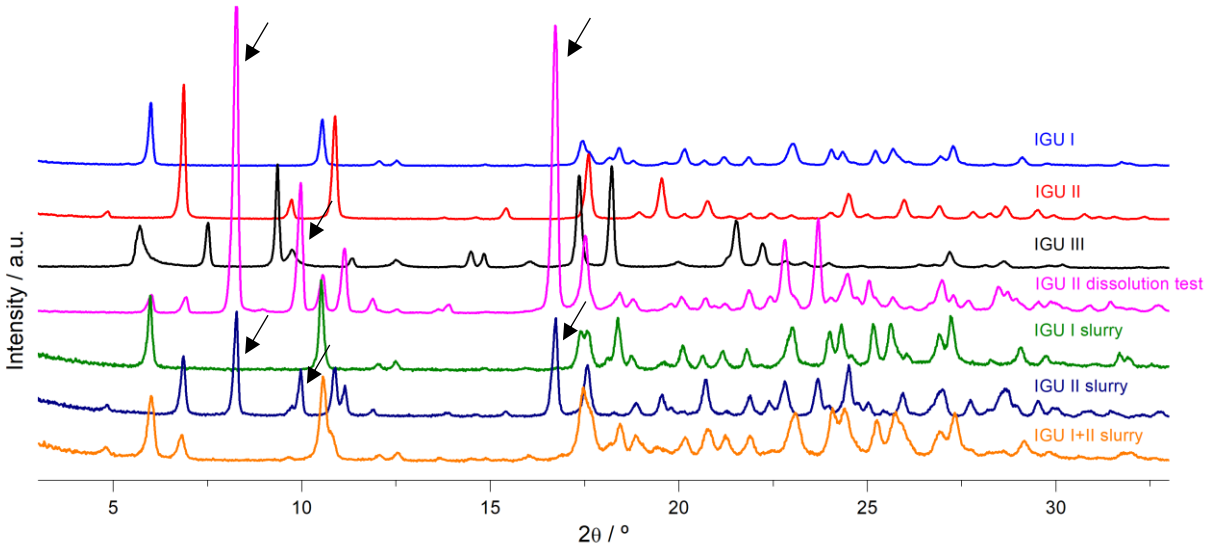

FIG. 27 – XRPD diffractogram of the IGU sample analysed after the dissolution test, the three slurries made to replicate the hydrated form, and forms I, II and III of IGU. The arrows mark the signals corresponding to the hydrate.

Three clear signals can be used to identify the hydrated form: 8.2°, 10°, and 16.7° (marked in **FIG. 27** with arrows). Using these as reference, it's possible to observe that only the slurry made from IGU's form II (IGU II slurry) originated the hydrate. It's showed, however, that this transformation was only partial, as some of form II's signals are still visible (for example, at ~ 5° and ~ 7°). As for the other two slurries, both show signals

from IGU, but none from the hydrate, by which is concluded they were not well succeeded.
Further characterization of the IGU hydrate may involve developing a better method to obtain it, with a good yield and no impurities, as well as studying its thermal behaviour with calorimetric techniques, such as DSC and TG.

3.2– Cocrystal and coamorphous investigation

3.2.1 - Leflunomide

3.2.1.1 – Polymorphism studies on LEF

Leflunomide (LEF) has two known polymorphs: form I and form II.[104] A XRPD analysis (**FIG. 29**) revealed that commercial LEF comes as a mixture of those two polymorphs, by comparison with the simulated diffractograms for forms I and II (generated on Mercury 2020.3.0 with data collected from CCDC). The isolation of each polymorph becomes then imperative, as the mixture would bring unnecessary complications for future studies with the compound.
It is known that forms I and II can be obtained by recrystallization from ethanol and benzene, respectively.[104] However, since benzene is a highly toxic solvent, it was crucial that an alternative methodology for the isolation of form II was found.
LEF's form I, when heated, transforms into form II through a solid-solid transition.[104] A DSC run, at a rate β = 10 ^{o}C/min, revealed the mentioned transition, at T = 125 ^{o}C, which was then followed by the fusion, at T = 165 ^{o}C (**FIG Apdx1 - 12**), both these values being in accordance with literature data.[104] A thorough analysis of the DSC curves of the LEF samples (**FIG Apdx1 - 12**) showed, however, that the polymorphic transition on the commercial sample was incomplete, and that a composed fusion took place, overlapping those for forms I and II. This allowed the determination of the fusion temperature of form I. A closer inspection of the DSC graph is done in **FIG. 28**. As can be seen on the commercial LEF curve, form I's fusion occurs at T = 165 ^{o}C (calculated from the commercial LEF curve), followed by the fusion of form II at T = 166 ^{o}C (calculated from the heated LEF curve).
Despite being incomplete, this transition proved to be a reliable approach for obtaining form II, as by simply heating a sample past the solid-solid transition temperature, it would convert into this polymorph (**FIG. 29**; **FIG Apdx1 - 12**).

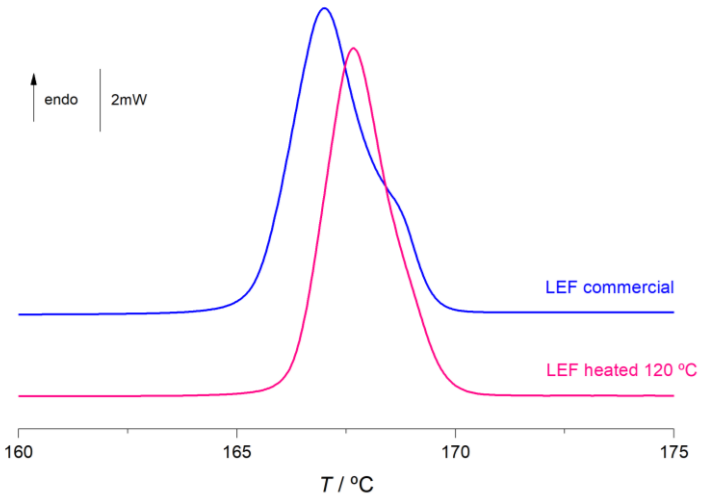

FIG. 28 – DSC curves of commercial LEF and LEF preheated to 120 ºC (zoomed in). β = 10 ºC/min.

Two samples of commercial LEF were submitted to LAG with EtOAc, respectively at 15Hz and 30Hz, for 30 minutes. A post milling XRPD analysis revealed that the compound, initially a mixture of polymorphs, had fully converted into form I in both cases (**FIG. 29** shows the result for 30 Hz). This not only presented itself as new, and essentially solvent-free, method for isolating form I, but would also imply that, in future grinding studies with LEF, regardless of its starting polymorphic composition, this compound would be fully converted into form I.

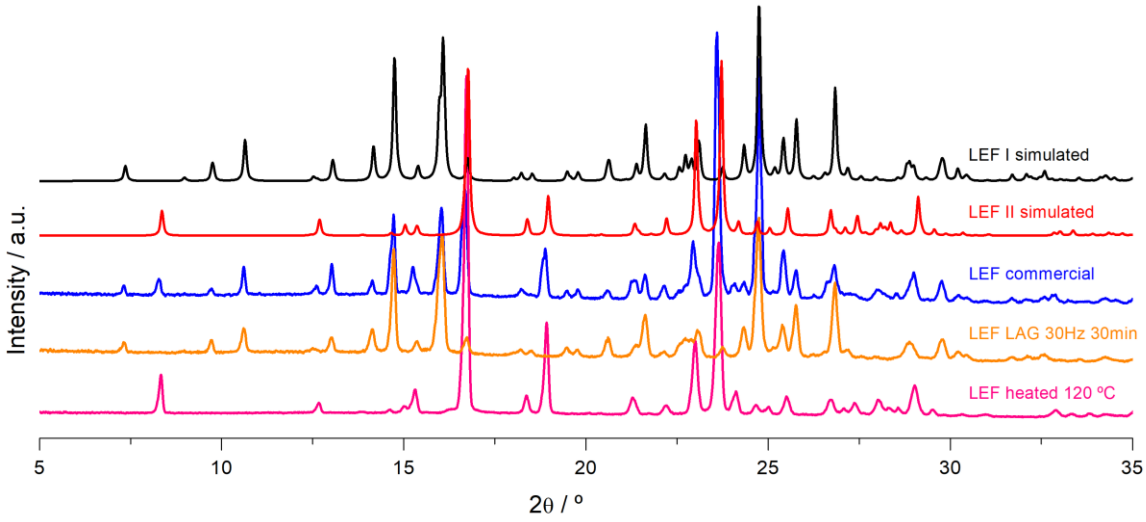

FIG. 29 – XRPD diffractogram of polymorphism studies conducted with LEF. Simulated data collected from CCDC (Vega 2006).

3.2.1.2 – IGU:LEF system study and characterization

An equimolar mixture of IGU and LEF was submitted to LAG, at 15Hz for 30min, with EtOAc, same conditions as those used in a previous study to obtain the 1:1 IGU:NA

cocrystal.[46] The analysis of the resulting solid by XRPD revealed some differences from the starting compounds and respective polymorphs, suggesting cocrystallization occurred. However, when the sample was heated by DSC, a single peak was not observed, but rather a series of successive fusion and crystallization events. This indicates not only the molar ratio used for obtaining the cocrystal was wrong, but also that part of the excess IGU and LEF originated an eutectic composition. The IGU:LEF system was studied by DSC, in molar ratios varying from 5:1 to 1:4.5, these being achieved with the same LAG conditions (**FIG. 30**). The DSC runs of the samples containing LEF were carried until 190 °C, since, in a TG analysis (**FIG. Apdx1-13**), this compound was found to start degrading before 200 °C.

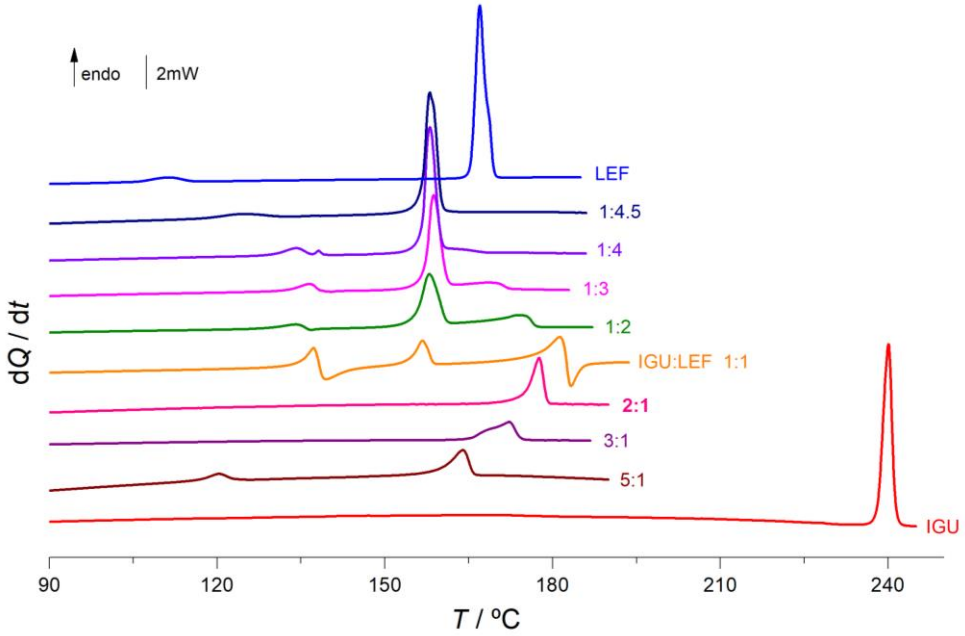

FIG. 30 – DSC curves of the various molar ratios used to study de IGU:LEF system. β = 10 °C/min.

The sample in a 2:1 molar ratio corresponds to the pure cocrystal. The DSC curve presents a single endothermic event, a fusion at T = 175 °C, which is situated in the middle of both API and coformer fusions, as is typical for these kinds of formulations.[41] FTIR-ATR spectra (**FIG. 31**) and XRPD diffractograms (**FIG. 32**) show significant differences between the cocrystal and the starting compounds and their polymorphs. Samples in **FIG. 30** were also studied by XRPD (**FIG. Apdx1-14**). It is possible to observe that the cocrystal was obtained (at least partially) in all compositions. However, excesses of IGU and LEF are observed for molar ratios other than 2:1.

IGU and LEF have been in the vanguard of scientific research on rheumatoid arthritis for over a decade. They proved effectiveness both in monotherapy, and in combinatory therapy with methotrexate.[105] This new API-API cocrystal could pave the way for discovering a possible synergetic effect between these two drugs. Further investigation on their physicochemical compatibility is, however, necessary.

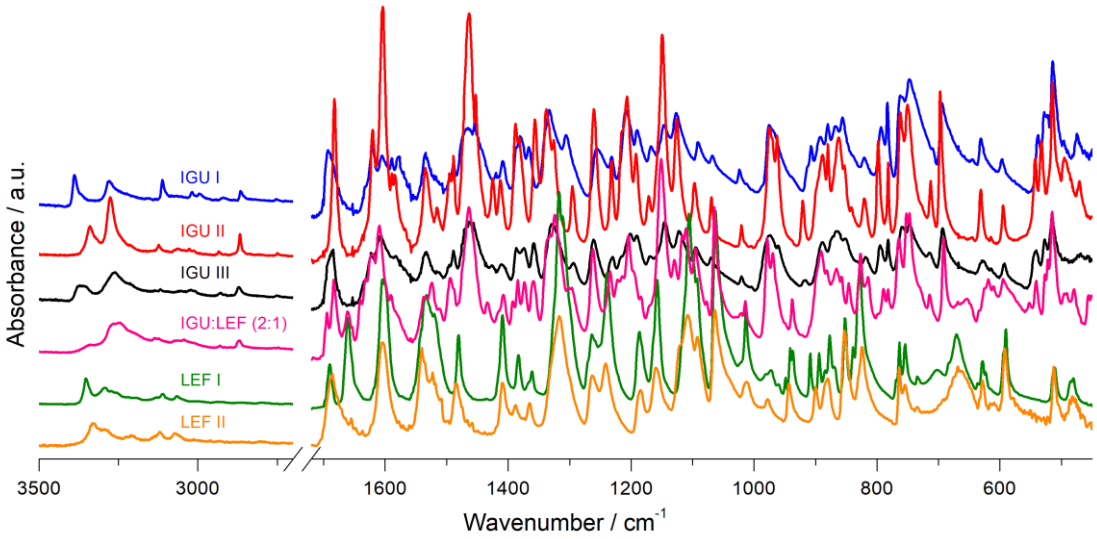

FIG. 31 – FTIR-ATR spectra of the IGU:LEF 2:1 cocrystal, and the known polymorphs of IGU and LEF.

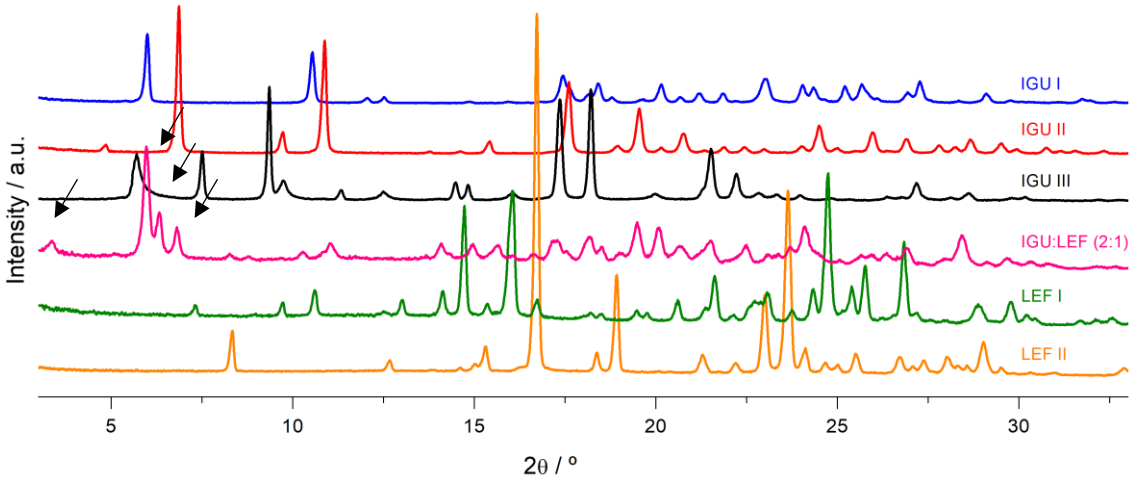

FIG. 32 – XRPD diffractogram of the IGU:LEF 2:1 cocrystal, and the known polymorphs of IGU and LEF. The arrows mark signals corresponding to the cocrystal.

The sample in a 1:4.5 molar ratio (χ_{IGU} = 0.18), as described in **FIG. 30**, presents a single fusion at $T \sim 152$ °C (following an endothermic transition), which is seen to also occur for the solids in a 1:1, 1:2, 1:3 and 1:4 molar ratio. An endothermic event is observed at $T \sim 120$ °C, which was found to be the solid-solid transition from polymorphs I to II of LEF. This was confirmed by preheating the sample until 130 °C and analysing it by XRPD, comparatively to LEF' known polymorphs (**FIG. Apdx1-15**). Since the 1:4.5 solid' diffractogram also shows peaks of the cocrystal (**FIG. Apdx1-14**), this is concluded to be an eutectic composition between the IGU:LEF cocrystal and LEF's form II.

PLTM images of both transition and fusion events were captured, and are displayed in **FIG. 33**. It is possible to observe that the entirety of the material melts, which corroborates the eutectic composition is in the right molar ratio.

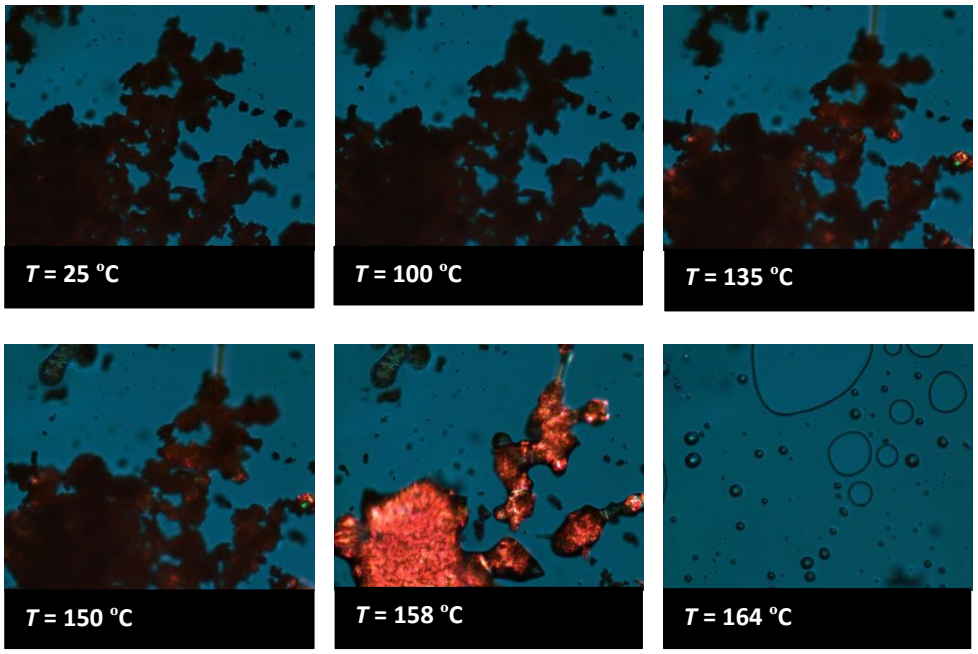

FIG. 33 – Images captured during a PLTM run with IGU:LEF 1:4.5. β = 10 °C/min.

3.2.1.3 – IGU:LEF NG study

As discussed in a chapter **3.1.2**, IGU turns amorphous with NG at 30 Hz for 60 minutes. In contrast, under these conditions, LEF does not. However, it was verified by XRPD that the 1:1 mixture with IGU fully turned amorphous, remaining unaltered over a period of at least 3 months (**FIG. 34**).

Furthermore, evidence of molecular interactions was found by FTIR-ATR (**FIG. Apdx1-16**), as the spectrum for this new solid shows several differences from those of the starting compounds (band shifts at 1205 cm^{-1}, 1016 cm^{-1} and 840 cm^{-1}). As such, this is concluded to be a coamorphous with interaction.

Similar to the IGU:LEF 2:1 cocrystal, this drug-drug coamorphous has potential for combinatory therapy in rheumatoid arthritis, but also for improving both component drugs' bioavailability by increasing their solubility, as amorphous materials are expected to be more water soluble than their crystalline counterparts. Additionally, coamorphous blends tend to remain stable over a longer period, meaning this could present as an advantage over IGU's amorphous.[62,63]

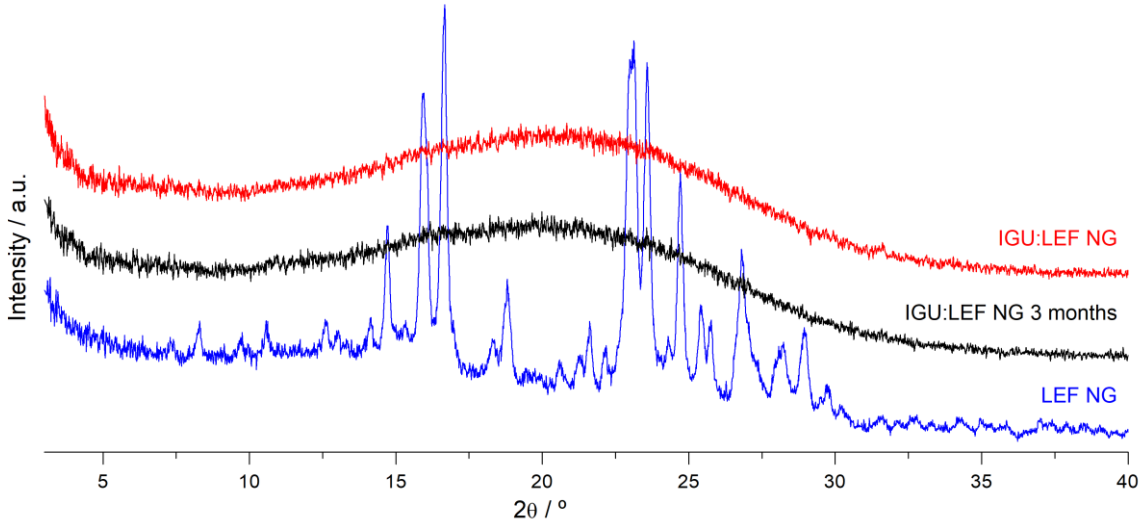

FIG. 34 – XRPD diffractogram of IGU, LEF and IGU:LEF 1:1, submitted to neat grinding at 30 Hz for 60 minutes.

3.2.2 - Sulfasalazine

3.2.2.1 – Preliminary studies with SSZ

A triclinic polymorph of sulfasalazine (SSZ) has been described by Lorena et al., which was obtained by recrystallization from EtOH. Besides the commercial form, this is the only known polymorph of SSZ. Furthermore, no form alterations have been reported to happen with mechanochemical grinding to date.[106]

SSZ, as well as the mixture with IGU in a 1:1 molar ratio, obtained by LAG at 15Hz for 30 minutes with EtOAc, were investigated with XRPD (**FIG. 35**) and FTIR-ATR (**FIG. Apdx1-17**). Through the analysis of these graphs, it was concluded that cocrystallization did not take place under the milling conditions used. The samples were also studied by PLTM (**FIG. 36**) and DSC (**FIG. Apdx1-18**), in order to assess their thermal behaviour. From PLTM analysis, it was verified that both SSZ and IGU:SSZ started to degrade immediately after fusion occurred. Although eutectic fusion was observed by both PLTM and DSC, investigation on this composition investigation was not conducted, as the observed degradation would have presented a great obstacle in further calorimetric studies.

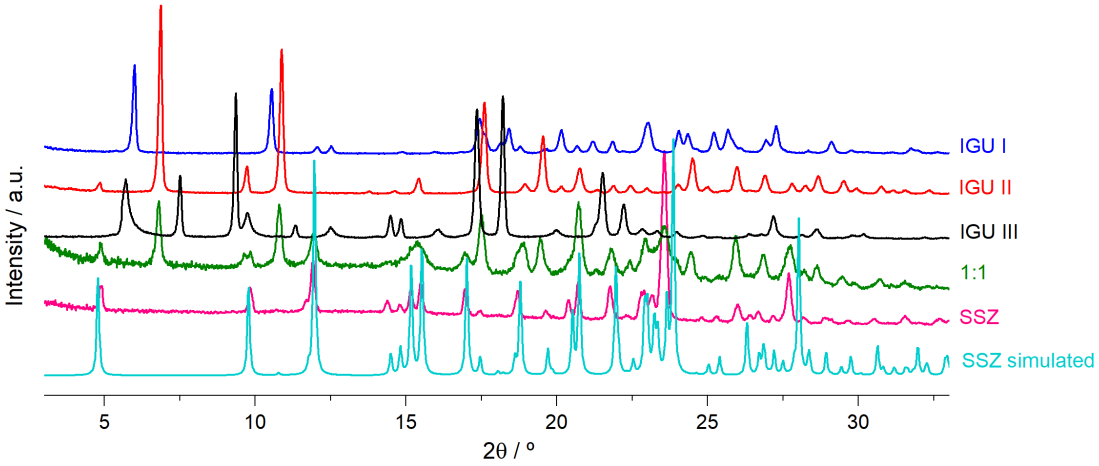

FIG. 35 – XRPD diffractogram of commercial and simulated SSZ, IGU' forms I, II and III, and the IGU:SSZ sample in a 1:1 molar ratio. Simulated data collected from CCDC (Filip 2001).

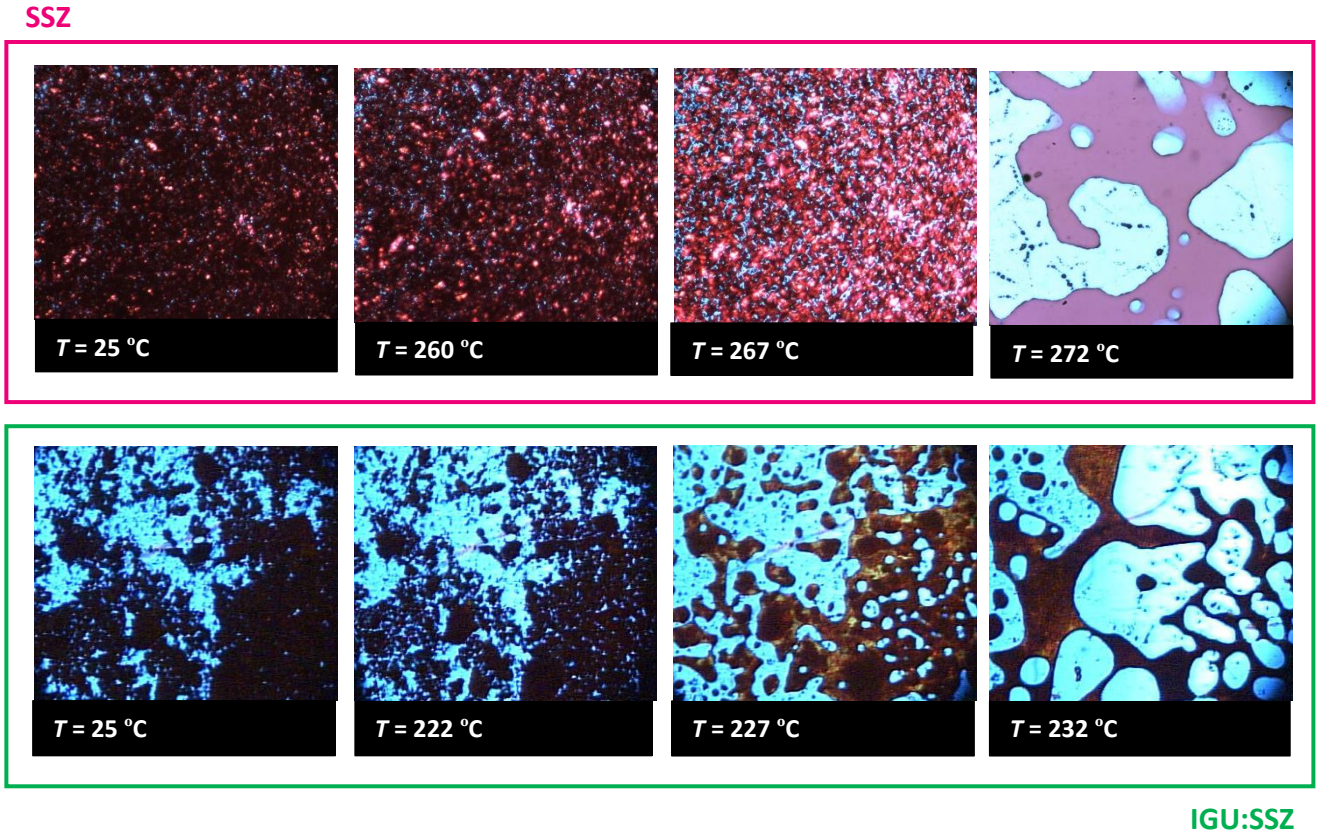

FIG. 36 – Images captured during a PLTM run with SSZ (pink) and the equimolar IGU:SSZ mixture (green) obtained through LAG. β = 10 °C/min.

3.2.2.2 – NG investigation with SSZ

A NG experiment was conducted, using a milling frequency of 30Hz, over a period of 60 minutes. SSZ was found to not fully turn amorphous in these conditions, even though

steel vessels were used. A similar result was observed with the IGU:SSZ 1:1 sample grinded in a zirconium vessel. In contrast, the 1:1 solid milled in a steel vessel produced a clear amorphous, as visible in the XRPD diffractograms in **FIG. 37**, demonstrating once more the overall better performance of steel vessels over zirconium vessels in amorphous obtention.

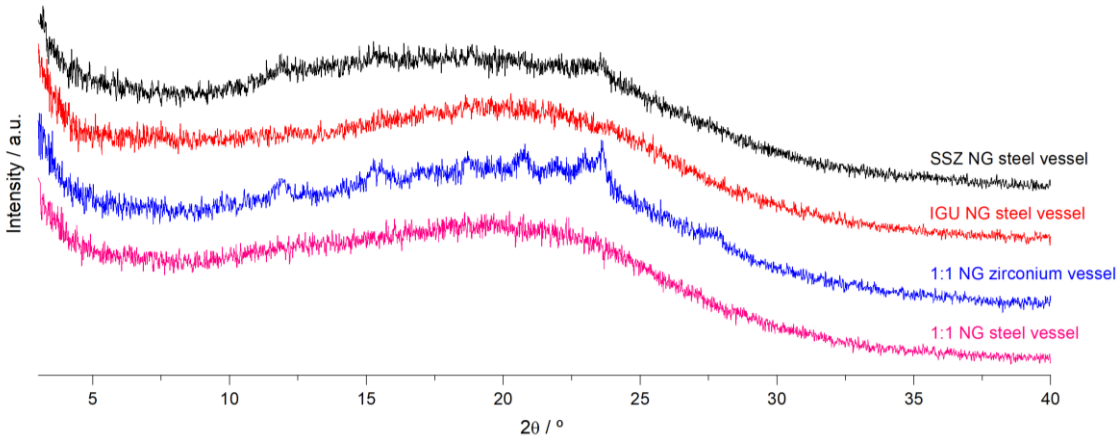

FIG. 37 – XRPD diffractogram of SSZ, IGU' forms II, and the IGU:SSZ sample in a 1:1 molar ratio, submitted to NG at 30Hz for 60 minutes.

3.2.3 – Folic Acid

3.2.3.1 – Analysis of FA's thermal behaviour

The study of folic acid dihydrate (FA) began with a thermal behaviour examination. Following heating by TG-DTA (**FIG. 38**), at a rate of β = 10 ºC/min, it is initially detectable a mass loss at $T \sim 100$ ºC. This was confirmed to correspond to the exit of two water molecules, by calculation with the percentage of lost mass, given by TG. The water exit process is also evident in the DSC analysis with a perforated capsule (**FIG. Apdx1-18**). Furthermore, Braga *et al.* found this step to be reversible, as by heating the sample to 150 ºC, and then cooling it to room temperature, the hydrated phase, as well as crystallinity, were restored over a certain period.[107] A first degradative process occurs at $T \sim 228$ ºC, which is represented by an endothermic event on the DTG curve. FA does not have an observable melting point.[108]

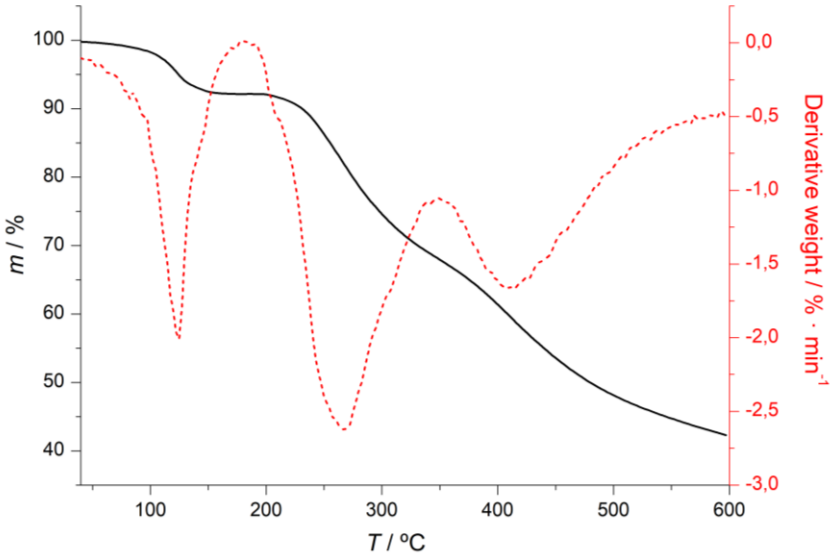

FIG. 38 – TG and DTA curves of a commercial FA sample. β = 10 °C/min.

Both water exit and degradation processes were observed by PLTM (**FIG. 39**), upon heating at β = 10 °C/min. Samples' loss of water is accompanied by a solid-solid transition to the anhydrous phase[107] (T = 130 °C). At higher temperatures, the colour fades (T = 184.5 °C) and the sample turns black (T = 220 °C), due to loss of crystallinity, which is caused by degradation.

Since FA degradation through heating was already characterized by Vora, *et al.*, no further investigation was made on this subject.[108]

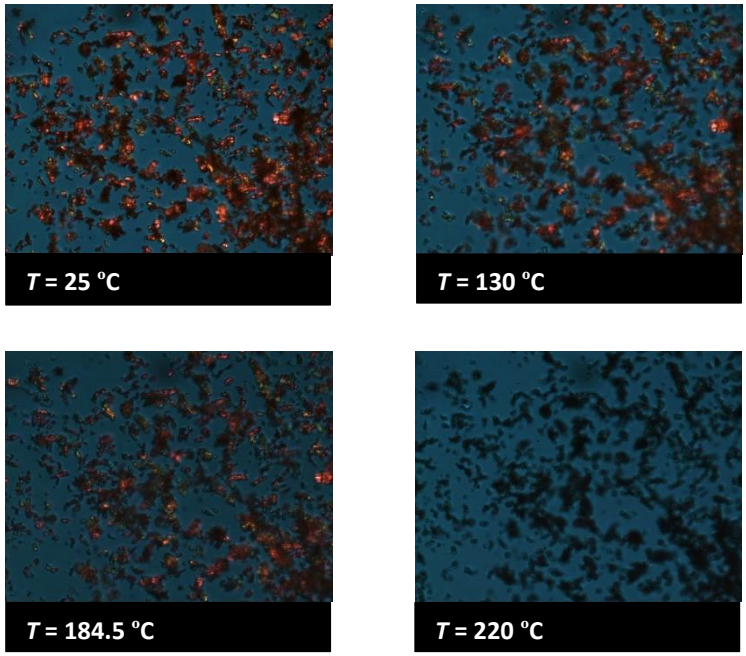

FIG. 39 – Images captured during a PLTM run with FA. β = 10 °C/min.

3.2.3.2 – IGU:FA system study with LAG and NG

As described by Braga *et al.*, FA dihydrate has two conformational polymorphs[109], FOL1 and FOL2, which differ in the conformation of the glutamic moiety. These were found to have a monotropic relationship, FOL1 being the more stable than FOL2. It is additionally stated that FA's anhydrous form is yet to be fully characterized, and there is no spectral data for it to date.[107] Since the early degradation complicates the study of FA with calorimetric techniques, and since there is still very little information on the anhydrous form, the focus of this study was instead placed in room temperature experiments.

An equimolar mixture of IGU and FA was submitted to LAG, at 15Hz for 30 minutes, with EtOAc. The resultant solid was analysed by XRPD (**FIG. 40**) and FTIR-ATR (**FIG. Apdx1-19**). From the analysis of the graphs, it was concluded that cocrystallization did not occur under these conditions.

In later attempts for the obtention of a cocrystal with IGU, higher milling frequencies and times were used. Although no improvements were observed on this matter, after a LAG run at 30Hz for 60 minutes, the 1:1 sample was found to turn amorphous, as visible in the diffractogram in **FIG. 41**. Hence, and since FA has been previously reported in successful coamorphous formulations[72,110], the amorphous form was further studied.

FA was found to fully turns amorphous with NG at 30Hz for 60minutes in steel vessels (**FIG. 41**). The observed bias for molecules with high molecular weight and flexibility, such as FA, to easily turn (and remain) amorphous is associated with the difficulty of the groups, that establish van der Waals interactions in the crystal lattice, realigning in proper order.

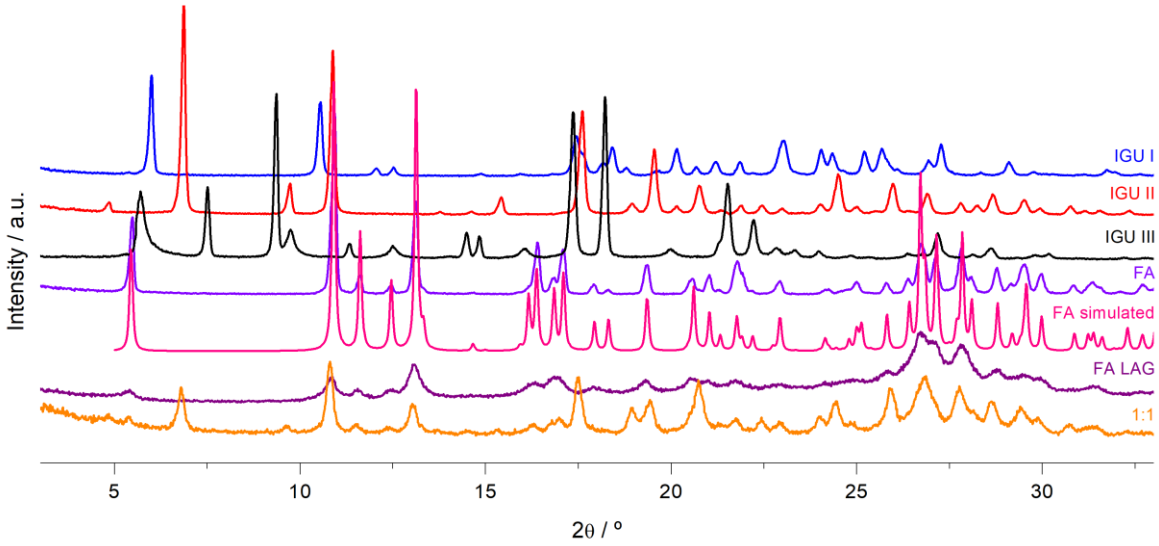

FIG. 40 – XRPD diffractogram of the three known IGU polymorphs, commercial FA, FA submitted to LAG at 15Hz for 30 minutes with EtOAc, and the equimolar mixture of IGU and FA, obtained in the same conditions.

A new 1:1 coamorphous with IGU and FA was also obtained with NG, in the same conditions used for FA. Moreover, the sample remained stable over a period of six months, which is also shown in the XRPD diffractogram in **FIG. 41**.

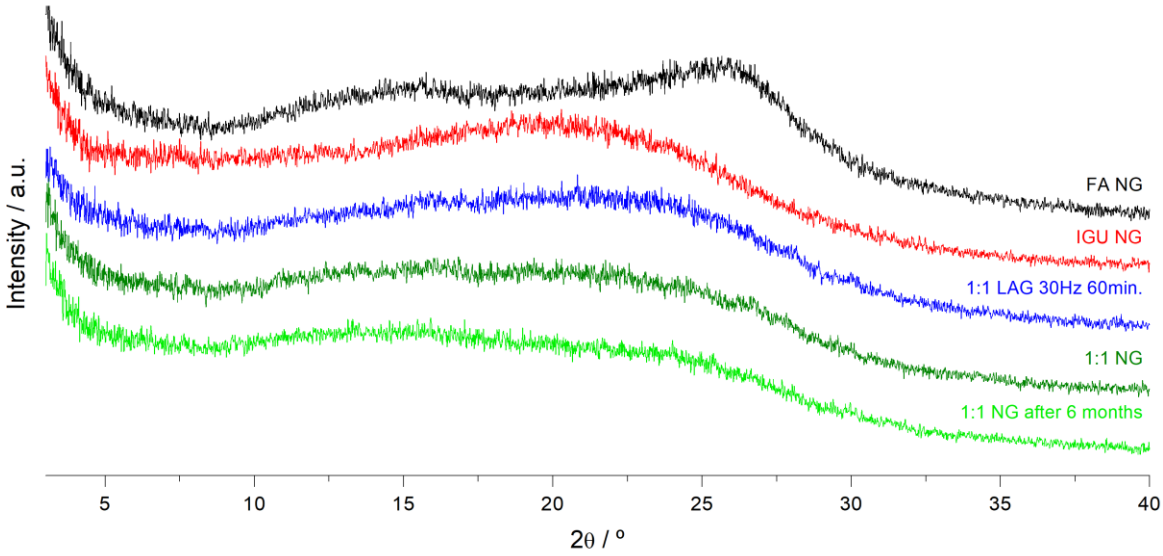

FIG. 41 – XRPD diffractogram of FA dihydrate and IGU, prepared with NG, and the IGU:FA sample in a 1:1 molar ratio, prepared by NG, and by LAG with EtOAc. NG was performed at 30Hz for 60 minutes, in steel vessels.

A later analysis of the IGU:FA 1:1 coamorphous by FTIR-ATR revealed no evidence of intermolecular interaction, as the 1:1 spectrum revealed a sum of the two component compounds' spectra (**FIG. Apdx1-20**). However, no qualitative conclusions can be taken from this, as several pharmaceutical coamorphous formulations, with no signs of molecular interactions between the constituent compounds, have been reported to significantly improve solubility and stability over the pure amorphous forms and the amorphous physical mixtures.[65–67]

3.2.4 – Nicotinamide

3.2.4.1 – Study of the IGU:NA system with NG

As mentioned in chapter **3.1.5**, the IGU:NA system has already been investigated with LAG, and a cocrystal in a 1:1 molar ratio was obtained. However, no coamorphous formation was observed in previous studies, and no other methods for obtaining this cocrystal were found. This chapter focuses on NG of IGU and NA, in order to complement the existing data on this system.

Coamorphous formation was studied by submitting two IGU:NA samples, in 1:1 and 1:2 molar ratios, to NG at 30Hz for 60 minutes, in steel vessels. NA amorphization was also

studied under the conditions mentioned. As shown in the XRPD diffractogram in **FIG. 43**, both 1:1 and 1:2 samples fully turned amorphous (unlike NA, which demonstrated to only become amorphous when grinded with IGU), this meaning coamorphous formation was successful.

Evidence of intermolecular interactions was found with for the 1:2 coamorphous, as is clear by analysing the FTIR-ATR spectra (**FIG. 42-A** and **FIG. 42-B**). This sample remained stable over a period of 3 months (**FIG. 43** – IGU 1:2 NG after 3 months).

The 1:1 spectrum showed a sum of IGU and NA's spectra, revealing no signs of interaction (**FIG. 42**). The 3 months later analysis by XRPD revealed the 1:1 coamorphous had crystallized in the cocrystal (**FIG. 44**). The transformation between coamorphous and cocrystal systems has been reported to occur for unstable coamorphous formulations, such as those in which the coformer has very low stability in the amorphous state, as is the case for NA.[111,112]

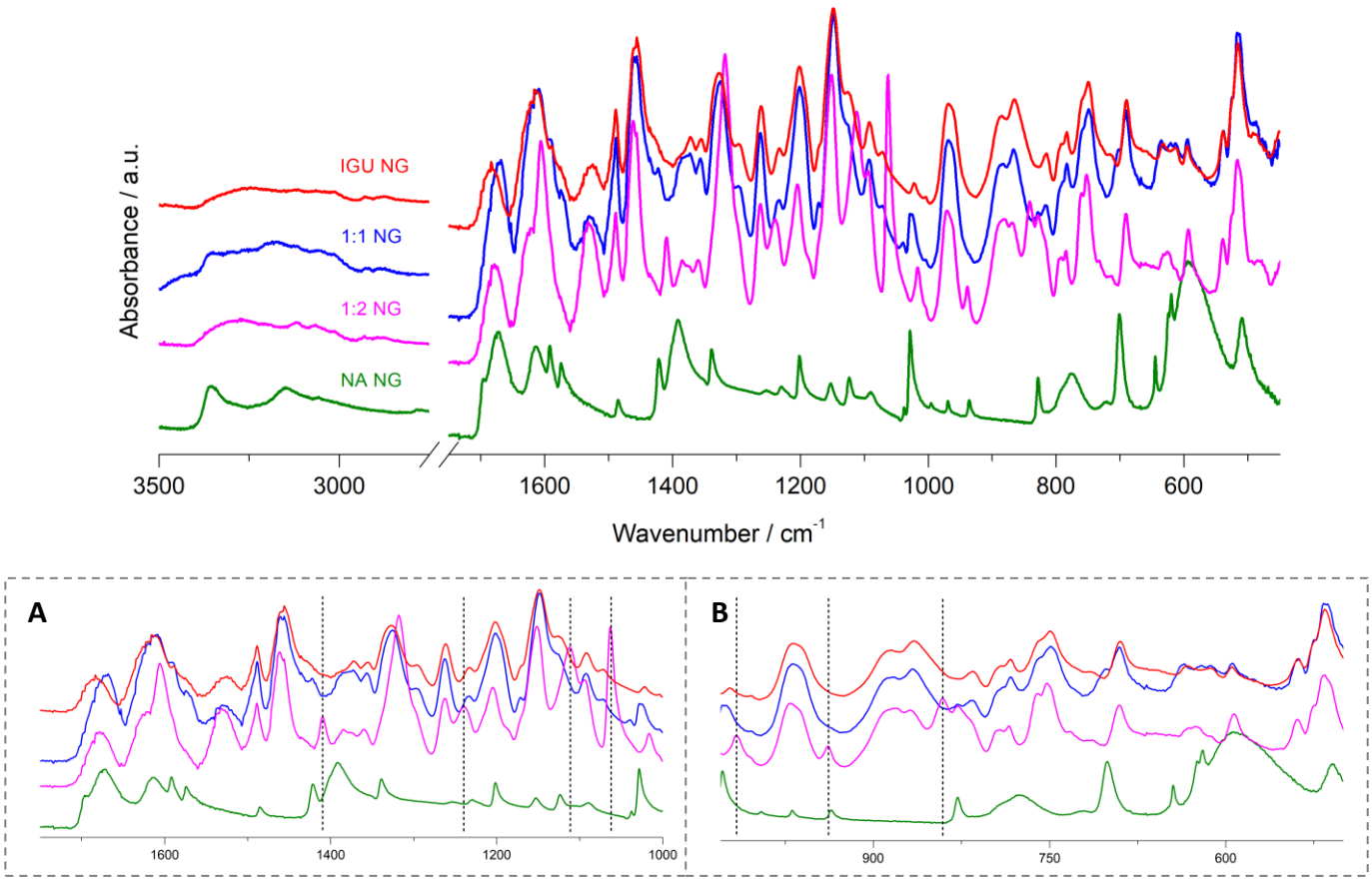

FIG. 42 – FTIR-ATR spectra of IGU, NA, and the samples in a 1:1 and 1:2 molar ratios, obtained with NG at 30Hz for 60 minutes in steel vessels. Panels **A** and **B** highlight the distinct peaks found on the 1:2 sample.

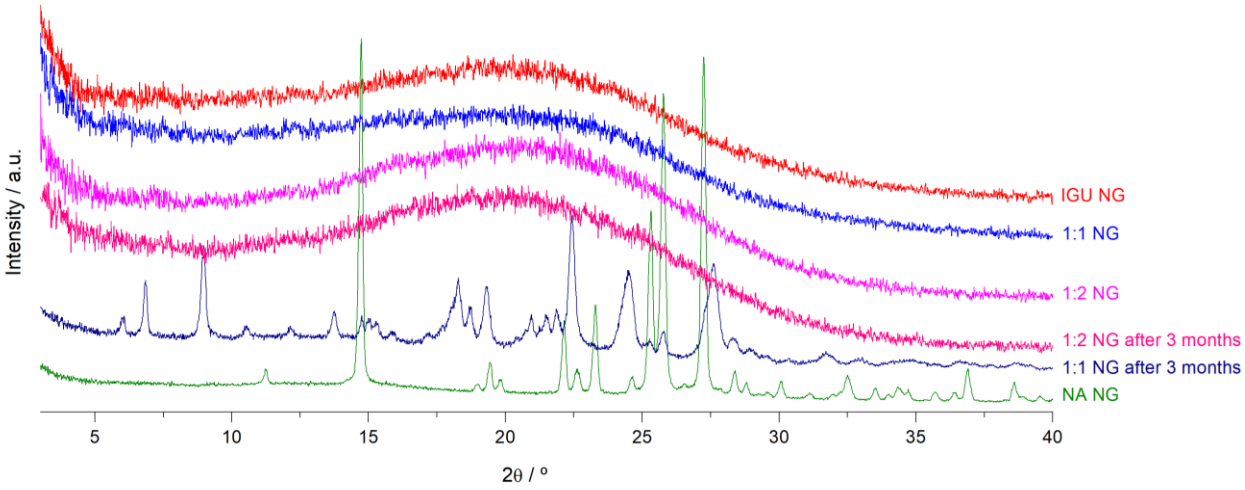

FIG. 43 – XRPD diffractogram IGU, NA, and the samples in a 1:1 and 1:2 molar ratios, obtained with NG at 30Hz for 60 minutes in steel vessels.

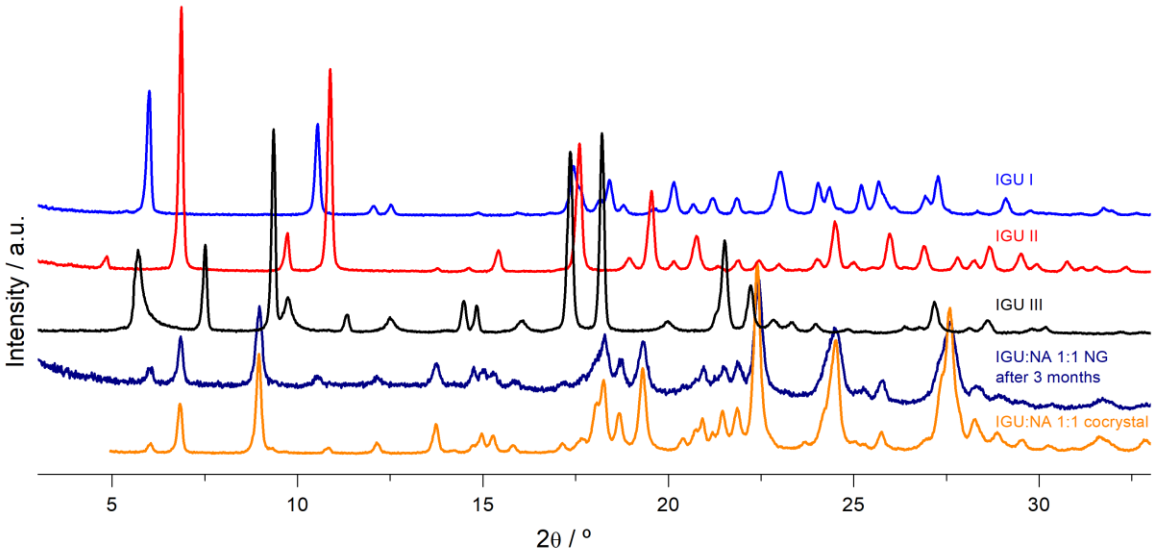

FIG. 44 – XRPD diffractogram of the known IGU polymorphs, the IGU:NA 1:1 cocrystal, and the IGU:NA 1:1 solid that crystalized from the amorphous 3 months after obtained.

Although the IGU:NA 1:1 cocrystal showed no solubility improvements over IGU[46], finding a method for stabilizing these new coamorphous could mark a turning point on the search for means to increase the oral bioavailability of this API.

3.2.5 – Metoclopramide and Omeprazole

3.2.5.1 – Calorimetric studies on MCP and OPZ

Metoclopramide (MCP) and Omeprazole (OPZ) cocrystal formation with IGU was investigated, the goal being the obtention of a dual-drug which improves IGU's solubility, while reducing its gastrointestinal side effects. However, the study with these compounds was abandoned at early stages, due to OPZ's degradation, and due to IGU:MCP's system high complexity, both being time consuming factors. Nonetheless, obtained results are briefly discussed in this chapter.

OPZ was submitted to LAG with IGU I, at 30Hz for 60 minutes, and with IGU II, at 15Hz for 30 minutes, with EtOAc. FTIR-ATR spectra (**FIG. Apdx1-21**) and XRPD diffractogram (**FIG. Apdx1-22**) analysis revealed cocrystallization was not achieved. DSC data on OPZ (**FIG. Apdx1-23**), as mentioned, showed signs on degradation immediately after fusion occurred, both for the pure API and the 1:1 mixture with IGU.

MCP was studied with IGU in various molar fraction, these being 1:1, 1:2.3 and 1:7.1. Mixtures were obtained with LAG, at 15Hz for 30 minutes, and at 30Hz for 30 minutes, using EtOAc as the solvent. XRPD diffractograms (**FIG. Apdx1-24**) showed no signs of cocrystal formation. Furthermore, DSC curves (**FIG. Apdx1-25**) revealed a series of fusion and crystallization events for each IGU:MCP composition, which indicated the presence of an eutectic composition. MCP's polymorph was also characterized with DSC and XRPD, by heating it past the solid-solid transition temperature.

3.3 – IGU in solution: determination of ε, pK_a and Φ_F

Beer-Lambert's law [88], shown in equation (4), describes a linear relationship between the concentration of a solution and its absorbance:

$$A = \varepsilon \cdot c \cdot l \tag{4}$$

Since the optical path (l) of the cuvette used equals 1 cm, the molar absorption coefficient (ε) can be calculated though a calibration curve of absorption versus concentration. **FIG. 45** shows the resultant plots.

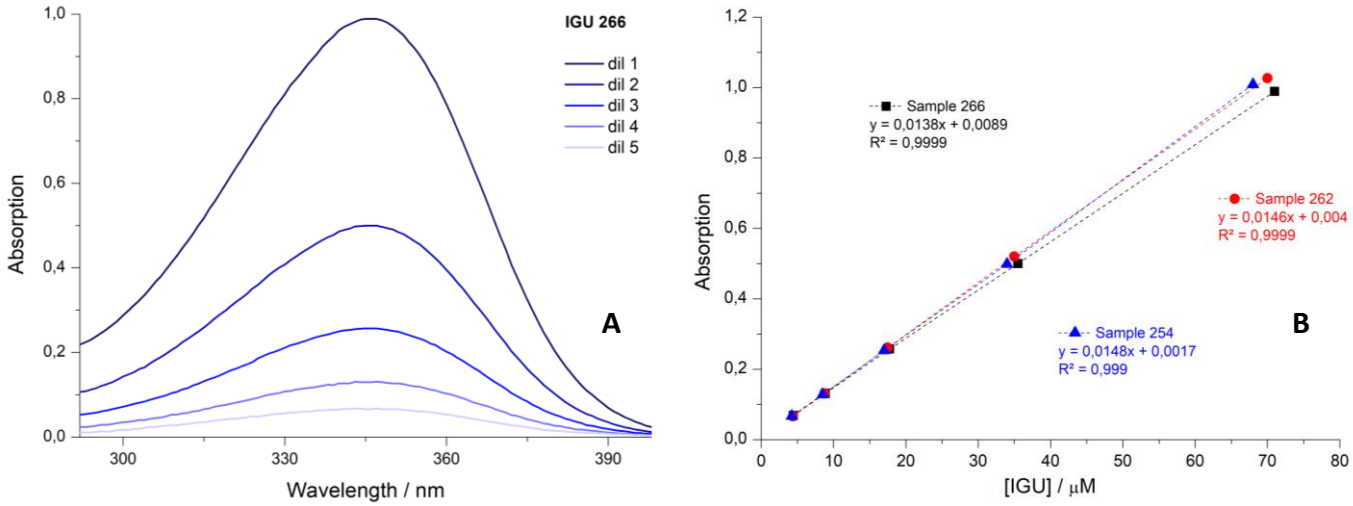

FIG. 45 – UV-vis spectra of dilutions 1 to 5 of "IGU 266" (**A**) and calibration curves of the three IGU samples: 266, 262 and 254 (**B**). Maximum absorbance values registered at λ = 347nm.

The molar absorption coefficient was calculated as the average value of the curve slopes. The obtained value was **ε_{IGU} (347 nm) = 1.44 x 10^4 $M^{-1}cm^{-1}$**, with a standard deviation of σ = 0.05 x 10^4 $M^{-1}cm^{-1}$, showing good reproducibility in the data set.

IGU was found to exist in two different species in solution: a neutral one, and a deprotonated one. This was firstly hypothesized when, while predicting the molecule's pK_a on the Marvin software [113], the N from the sulphonamide group was showed to lose its proton. This will be further discussed in this chapter, as well as substantiated with experimental data.

The pK_a value of IGU was characterized from the concentration of the neutral and deprotonated species, depending on pH. By analysing the UV-Vis spectra (**FIG. 46**), it is observable that, as the pH is decreased, the absorbance peak moves to lower wavelengths (**FIG. 46 - B**). It is also noticeable that the maximum registered absorbance reduces to approximately half its original value (**FIG. 46 - A**). This is due to the prevalence

increase of the neutral specie as the pH is lowered. Since concentration is kept constant, it can be inferred that ε also decreases.

The fluorescence spectra (**FIG. 47**) reveals a decrease in intensity as the pH is lowered, ult imately nearing zero, at pH = 3. This suggests only the deprotonated specie presents fluorescence, as will be discussed later in this chapter.

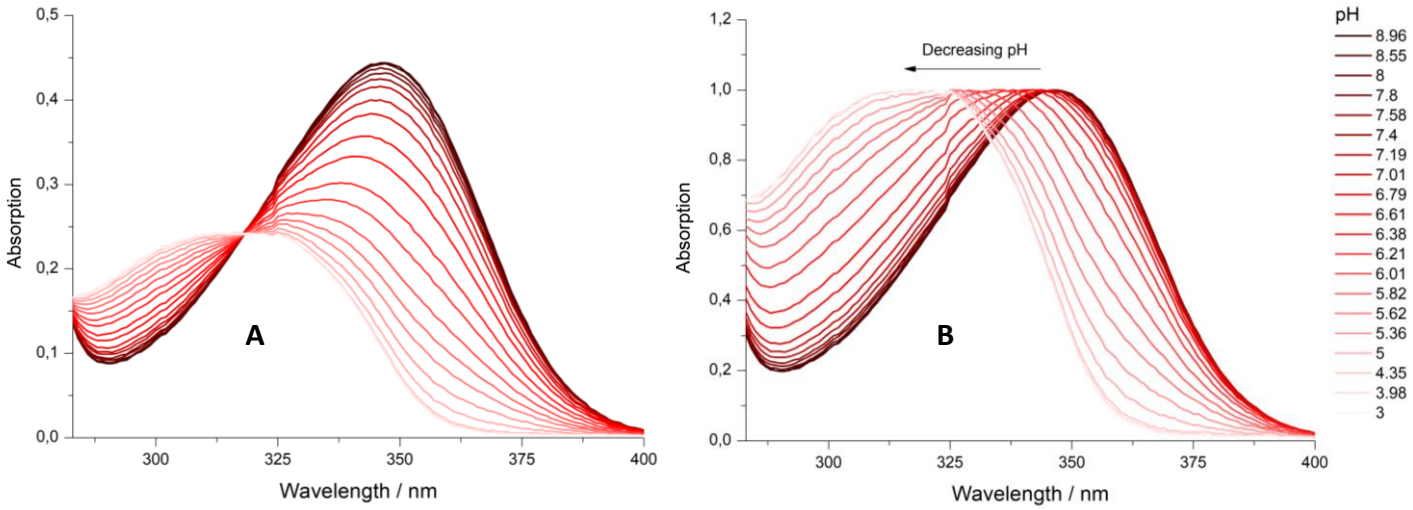

FIG. 46 – Raw UV-Vis spectra (**A**) and normalized UV-Vis spectra (**B**) of the pH titration of a IGU solution at 4.25 µM in PBS with 2% DMSO.

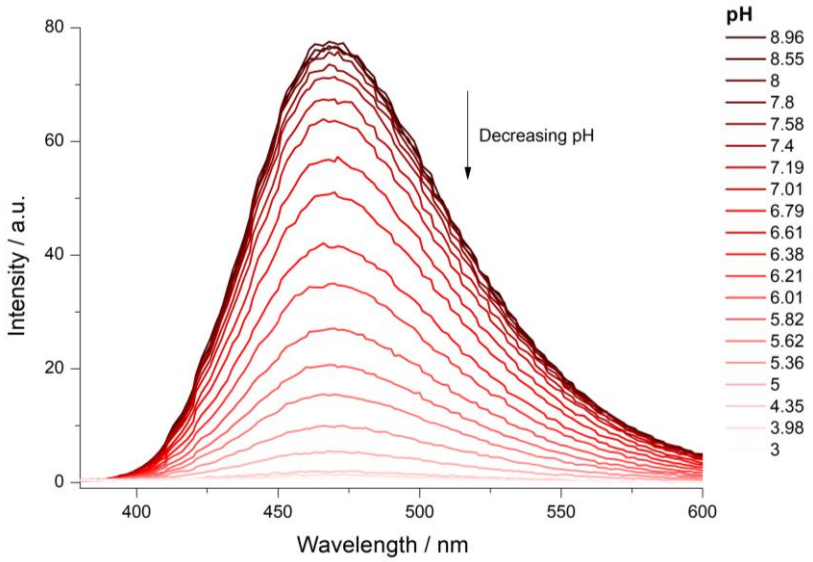

FIG. 47 – Fluorescence spectra of the pH titration of a IGU solution at 4.25 µM in PBS with 2% DMSO.

FIG. 48-A shows the curves for the maximum absorbance values, registered at 325 nm and at 346 nm, and **FIG. 48-B** shows the curve of the maximum fluorescence intensities, registered at 470 nm. The inflection point (IP) corresponds to the pK_a, the pH at which both species have an incidence of 50%.

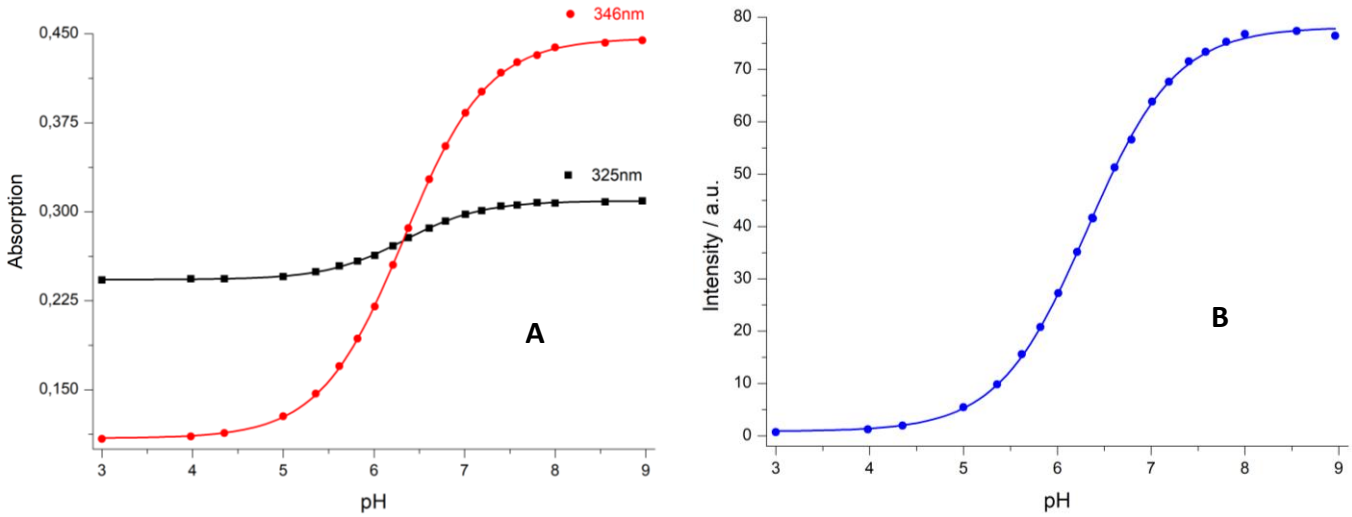

FIG. 48 – Best fit curves from the titration with IGU. Maximum registered absorbance (**A**) and fluorescence (**B**) values are plotted as a function of pH. IP(**A**)$_{346}$ = 6.33; IP(**A**)$_{325}$ = 6.33; IP(**B**) = 6.32.

Curves resulted from the best fit of equation (5) to the experimental values:

$$[\mathrm{A}] = \frac{[\mathrm{A}]_\mathrm{T} \times K_\mathrm{a}}{[\mathrm{H}^+] + K_\mathrm{a}} \qquad (3)$$

Where $[\mathrm{A}]$ is the concentration of the protonated/deprotonated specie in µM; $[\mathrm{A}]_\mathrm{T}$ is the total concentration of IGU in solution; K_a is the first dissociation constant; and $[\mathrm{H}^+]$ is the hydrogen ion concentration.

Species incidence (%) was plotted as a function of pH (**FIG. 49**), using the fluorescence pK$_a$ data (**FIG. 48-B**), allowing for a clearer insight on the prevalence of the deprotonated form at physiological pH.

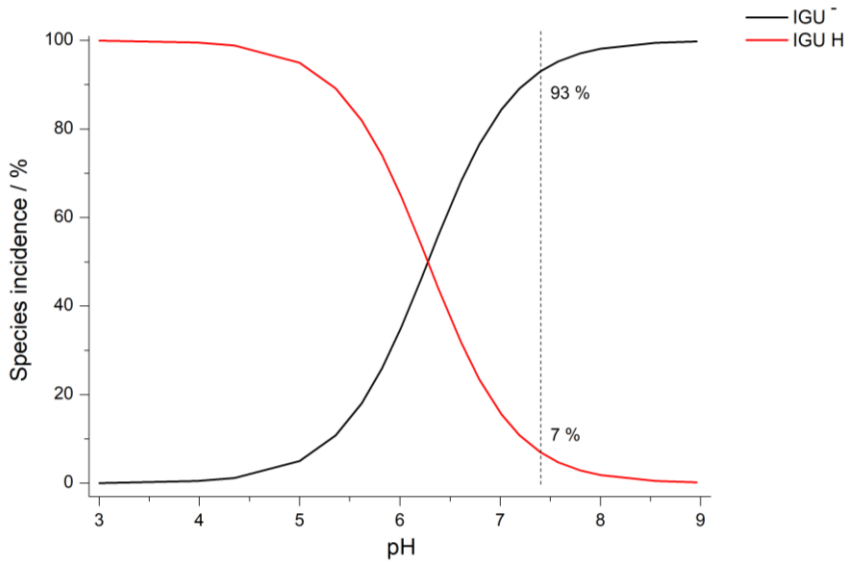

FIG. 49 – Incidence (%) of the neutral (IGU H) and deprotonated (IGU $^-$) species of IGU in solution. The arrows mark the % values at pH = 7.4.

The obtained value was **pK_a = 6.3**.

The fluorescence quantum yield was calculated for both neutral and deprotonated species of IGU, respectively by adjusting the pH of the solutions to 3 and to 9. At these pH values, the incidence of each one of these species is close to 100%, as was shown in **FIG. 49**.

For this calculation, equation (6) [91] was used:

$$\Phi_S = \Phi_R \times \left(\frac{F_S}{F_R} \times \frac{A_R}{A_S} \times \frac{{n_S}^2}{{n_R}^2} \right) \quad (6)$$

where Φ_R is the quantum yield of QS [89,91]; F_S and F_R are the integrated fluorescence intensities of the sample and the reference, respectively; A_R and A_S are the absorbance values at the excitation wavelengths (320 nm in the pH = 3 solution, and 346 nm in the pH = 9 solution); and ${n_S}^2$ and ${n_R}^2$ are the refractive indexes of water (1.333) and 0.5M H_2SO_4 (1.346).

The Φ_F value obtained was **0.0007** for the neutral specie, and **0.0779** for the deprotonated specie, confirming that only the deprotonated form of IGU is fluorescent. The fluorescence spectra of both forms is displayed in **FIG. Apdx2 - 1**, and is compared with QS, which has a Φ_F of 0.546.[89]

Fluorescence spectroscopy will be used in further chapters as the prime characterization technique for IGU, as it allows its monitoring at high pH values (deprotonated specie predominates), in relatively low concentrations, and without the interference of other non-fluorescent molecules in solution.

3.4 – IGU interaction with POPC and POPC:DDAB

IGU solutions were studied by fluorescence spectroscopy, while varying the lipid concentrations from 0 to 10 mM. The results obtained with POPC were compared with those of POPC:DDAB. The process for studying IGU's lipid interaction was based on the wavelength shift that occurs upon partitioning to the lipid bilayers [87] (**FIG. 50** and **FIG. 51**).

A simplified version of the equation used by Cardoso, *et al.*[87] was used for this partition model. Equation (7):

$$\lambda_{shift} = \frac{K_L \cdot 10^{-3} \cdot [L]}{1 + K_L \cdot 10^{-3} \cdot [L]} \quad (7)$$

where K_L is the partition coefficient K_P multiplied by the molar volume of POPC (0.795 dm^3/mol) [87], and $[L]$ is the concentration of lipid (POPC or POPC:DDAB). K_L values appear multiplied by 10^{-3} so the units match with those of $[L]$.

FIG. 50-A and **FIG.51-A** represent the best fit of equation (7) to the experimental results. At the pH value the experiment was conducted (7.4), IGU is mostly present in its ionized form (**FIG. 49**). This justifies the higher partitioning observed to the positively charged lipid (POPC:DDAB - **FIG. 51**). In comparison, IGU showed significantly lower partitioning to the neutral lipid (POPC – **FIG. 50**).

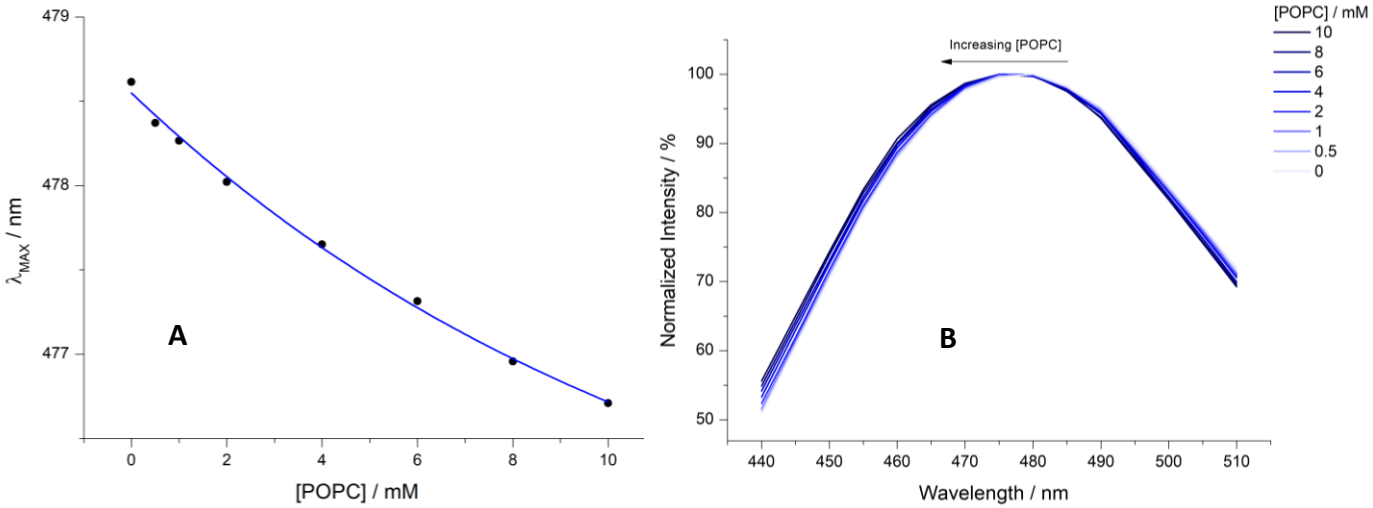

FIG. 50 – Best fit curve to the wavelength shift (**A**) and normalized fluorescence variation (**B**), with the increase of [POPC].

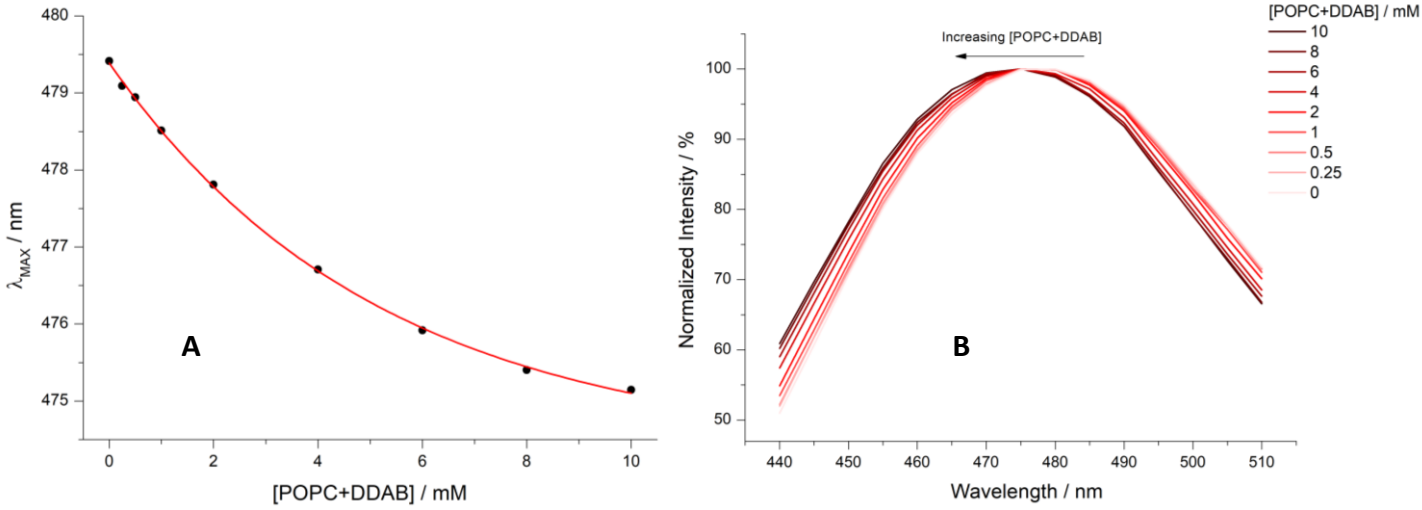

FIG. 51 – Best fit curve to the wavelength shift (**A**) and normalized fluorescence variation (**B**), with the increase of [POPC:DDAB] (9:1 molar ratio).

K_L was calculated from the best fit of equation (7). Confidence intervals (CI) at 75% and 90% were determined from the chi-square test (**FIG. Apdx2 - 2-A** and **FIG. Apdx2 - 2-B**).

The obtained result for POPC was 4.60 x 10^1 with a 75% CI of [7, 106], and for POPC:DDAB was 1.46 x 10^2 with a 90% CI of [107, 193]. This means that, at the maximum lipid concentration used (10mM), IGU was approximately 30% partitioned into the POPC lipid bilayer in the study with POPC, and 60% for lipid bilayer formed by POPC:DDAB (9:1 molar ratio).

3.5 – Permeation studies with LUVs of POPC

IGU's elution profile through the Zeba™ columns was studied with UV-Vis and fluorescence spectroscopy. Knowing the volume PBS that needs to be passed through the column in order for IGU to start eluting proves determining, as this behaviour is expected to be reproduced by the IGU that permeated the POPC LUVs bilayer in the following studies.

From **FIG. 52** it is noticeable that IGU starts exiting the column after roughly 3000 µL of PBS were passed through, the peak absorbance and fluorescence being registered around the 5000 µL mark. This behaviour should maintain in the permeation tests for the IGU that has permeated the LUVs, while the encapsulated IGU ought to exit first with the lipid vesicles. The performance of both columns was similar, which advocates for good performing conditions.

The analysis of the data from the separation of the non-encapsulated IGU brought some concerns. The UV-Vis spectra (**FIG. 53**) and absorbance versus volume curves (**FIG. 53**) showed the LUVs exited mainly after the first passage of PBS (500 mL). However, IGU left the column sooner than expected, as the peak absorbance was registered with the passage of 3500 mL of buffer, rather than 5000 mL.

This suggests the compound is being dragged by the LUVs, or even rapidly permeating the vesicles as they are crossing the resin gel, which results in an early exit. Furthermore, the exit of the LUVs is overlapped with that of IGU, as the curve does not go to zero (**FIG. 54**– 1500 mL PBS).

The pH of the IGU solution was adjusted to 9 (**FIG. 54-B**), as an attempt to lower its permeation velocity by increasing the incidence of the deprotonated specie. Yet, this produced no effect, for the results were similar to those at pH = 7.4 (**FIG. 54-A**).

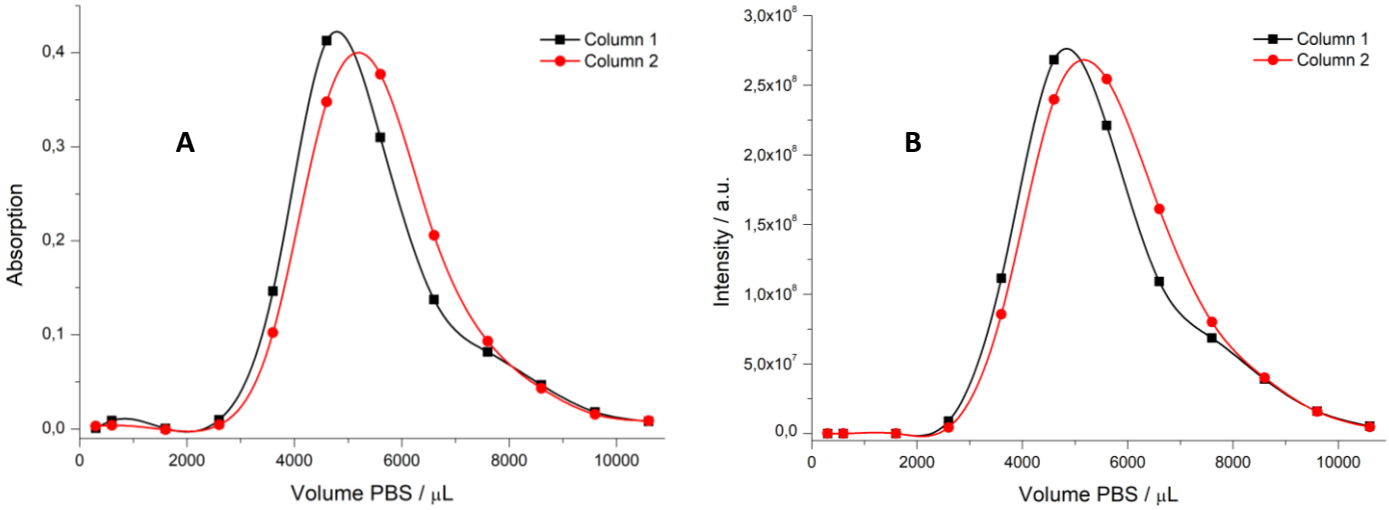

FIG. 52 – Absorbance at 345 nm (**A**) and fluorescence intensity at 480 nm (**B**), as a function of the volume of PBS passed through the size-exclusion chromatography columns, describing IGU's exit profile.

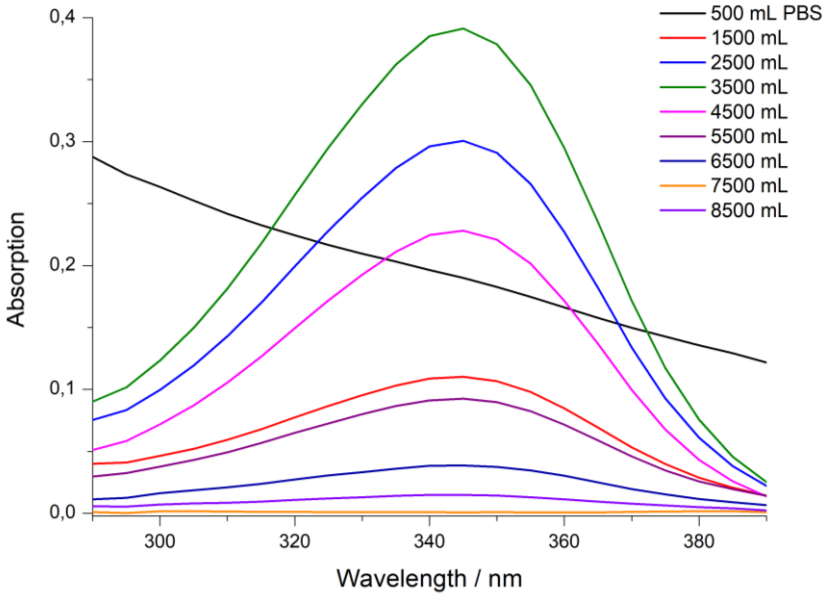

FIG. 53 – UV-Vis spectra from the separation of the non-encapsulated IGU.

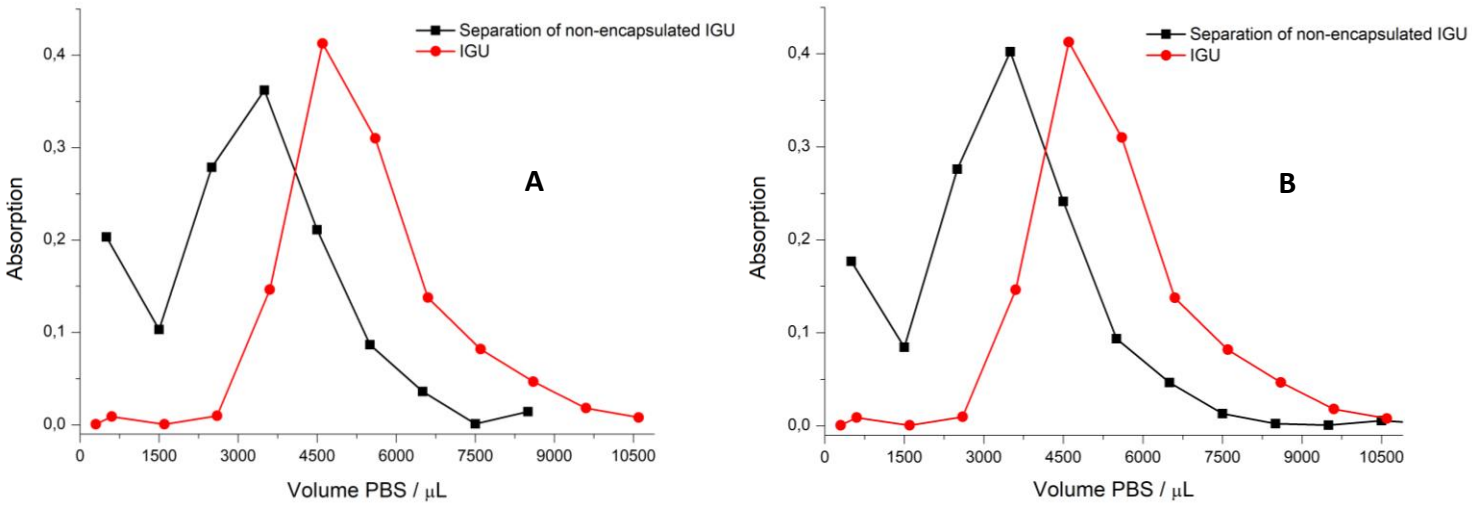

FIG. 54 – Absorbance at 345 nm, as a function of the volume of PBS passed through the size-exclusion chromatography columns, for IGU, and the separation of the non-encapsulated IGU from the LUVs, at pH = 7.4 (**A**) and at pH = 9 (**B**).

The overlapping of curves, and the suggested fast permeation through the LUVs bilayer, is incompatible with this assay, as it can only determine the permeation velocity for slow permeating compounds. As such, further results were inconclusive, showing only that IGU desorption from and permeation through the lipid bilayer of LUVs occurs in a time scale comparable to that of elution from the column (a few minutes).

3.6 – Dynamic light scattering studies

DLS was used to analyse the IGU dilutions prepared in section **2.6**, to evaluate eventual aggregation. Experimental data distribution fit (**FIG. 55**) reveals a rapid decrease in correlation, responsible for the small particles in the dispersion, as values are observed to start from 0.4 at around 1 us. The correlation function shows the presence of some particles with intermediate sizes, although it does not show a trend with concentration. It also reveals the presence of very large particles, with a weight that is higher for less diluted solutions, suggesting it is originated by IGU aggregates. However, the best fit of the correlation function for the larger aggregates is not good, for which the size distribution obtained for this region is not reliable.

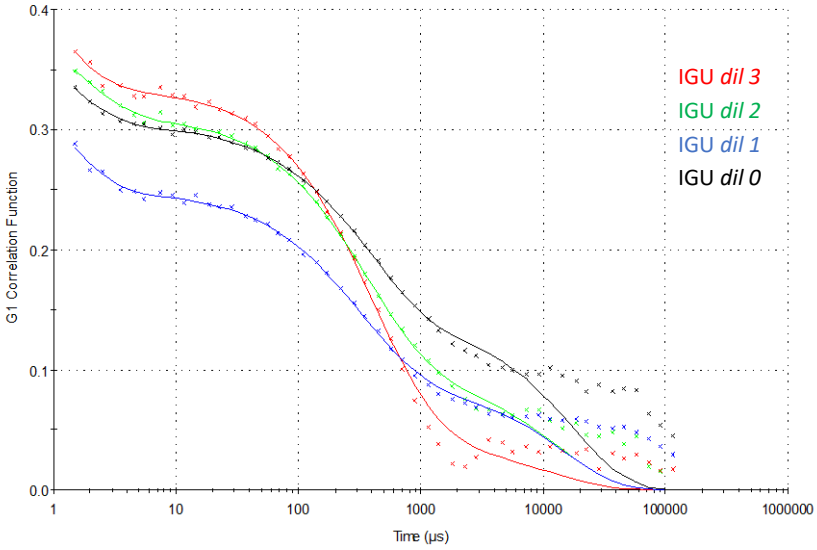

FIG. 55 – Correlation function and corresponding best fit for the four IGU solutions in PBS with 2 % DMSO, with concentrations of 67.4, 33.7, 16.9, and 8.4 µM (*dil* 0 to *dil* 3).

The volume distribution is showed in **FIG. 56**, revealing a prevalence of smaller particles in solution. The size of those small particles is not well defined, because it is obtained from the best fit of the correlation function at times smaller than 4 us, where there are few experimental values. Nevertheless, the value obtained (around 0.6 nm) is compatible with IGU monomers is solution.

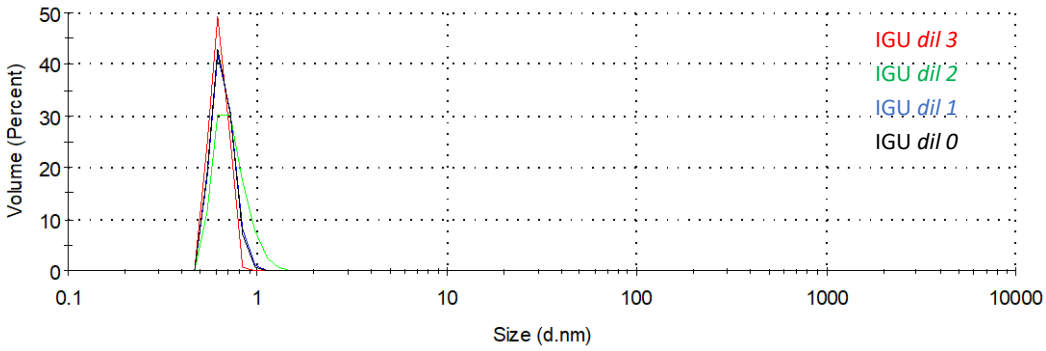

FIG. 56 – Size distribution by volume of the four IGU solutions studied.

From the analysis of the scattering intensity of the IGU solutions (**FIG. Apdx2 - 3**) it is possible to evaluate the global variation in the scatter contribution for particles in solution and their relative size. Comparing these results with those obtained for PBS (**FIG. Apdx2 - 4**), it is observable that most of the scattered light for particle sizes greater than 1000 nm comes from the solvent, which suggests it might have contained traces of dust.

Since the voltage was maintained throughout the analysis, the count rate for each sample is directly proportional to the intensity of scattered light. The derived count rate of the four samples and the stock solution in DMSO is represented in **FIG. 57**. It is observable that the first three samples (*dil 3*, *dil 2* and *dil 1*) appear to be similar, while

having a count rate slightly higher to that of the solvent. However, a big increase is verified from *dil 1* to *dil 0* (record index 3 to 4), followed by an even bigger increase from *dil 0* to the stock solution (record index 4 to 5). These increases in the intensity of scattered light for higher IGU concentrations suggest the formation of aggregates, as IGU significantly contributes for the overall dispersion of the sample.

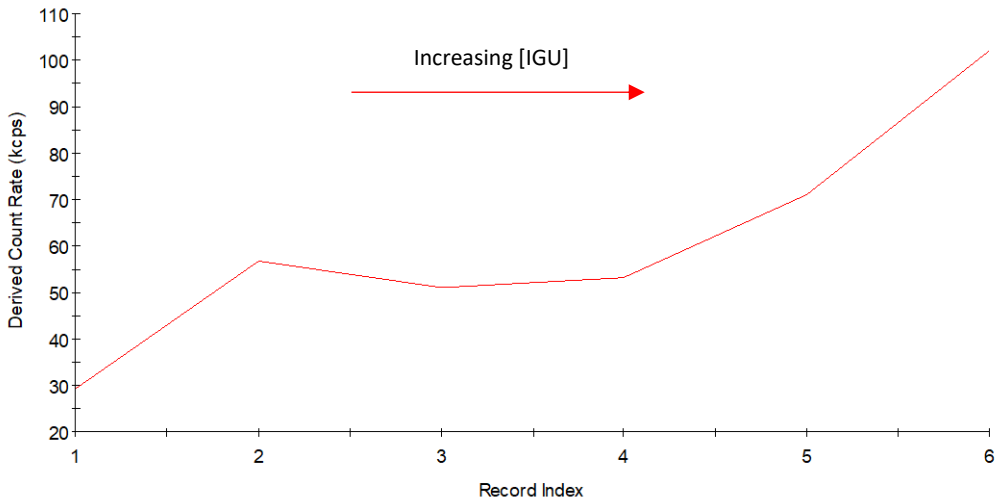

FIG. 57 – Derived count rate of PBS, the IGU stock solution in DMSO, and the four IGU solutions studied. Record index number 1 corresponds to PBS, numbers 2 to 5 correspond to IGU *dil 3* to *dil 0*, and number 6 corresponds to the stock solution.

The LUVs were also analysed by DLS, after the extrusion process. The distribution fit (**FIG 58**) revealed a much slower loss of correlation when compared **FIG. 55**, due to the presence of large particles in the suspension (POPC vesicles).
The resulting average size calculated for the POPC vesicles from the size distribution by volume data (**FIG. 59)** was **114.7 nm**, which matches the expected diameter for a LUV, meaning extrusion was successful.

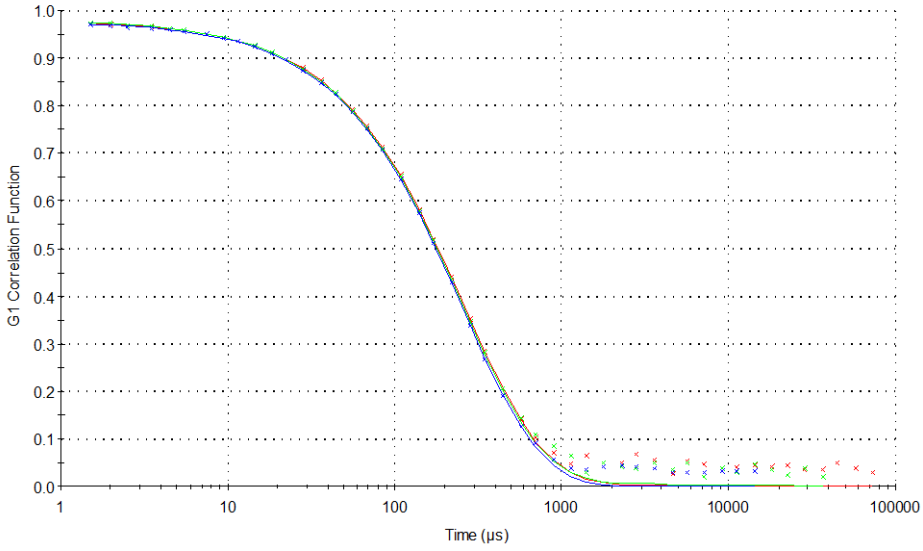

FIG. 58 – Correlation function and corresponding best fit for the POPC LUVs collected from extrusion.

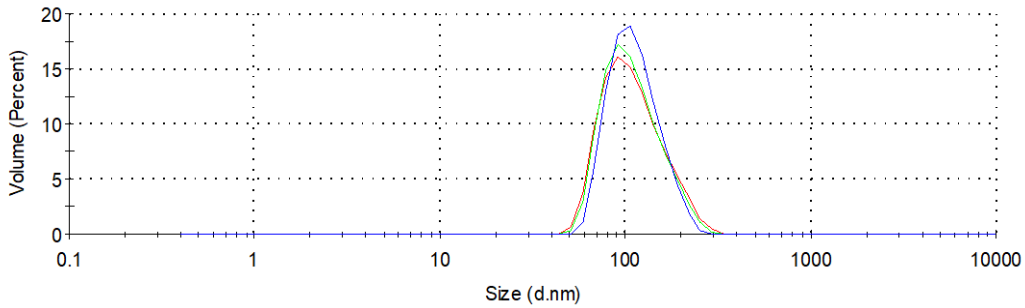

FIG. 59 – Size distribution by volume of the POPC LUVs collected from extrusion.

3.6.1 – Zeta potential determination

The zeta potential of POPC LUVs was measured, and compared with the value for the POPC LUVs in the presence of IGU. The obtained values are summarized in **Table 5**. The average potential obtained for POPC was -1.72 mV. However, in the presence of IGU, the potential significantly changed, taking the value -16.7 mV. This is due to IGU's deprotonated specie, which is prevalent at pH = 7.4. Furthermore, this severe change in potential also advocates for the interaction between IGU and the lipid, discussed in section **3.6**.

Table 5 – Zeta potentials calculated for the POPC samples

Sample	Zeta Potential (mV)
POPC LUVs + IGU (1)	-14.9
POPC LUVs + IGU (2)	-18.7
POPC LUVs + IGU (3)	-16.4
POPC LUVs (1)	-1.44
POPC LUVs (2)	-2.15
POPC LUVs (3)	-1.58

CONCLUSIONS AND FUTURE WORK

IGU solid state proved to be an interesting, yet complex subject matter. In the present work, six compounds, used in modern medicine practice for three distinct therapeutical purposes, were investigated with IGU: LEF, SSZ, NA, FA, OPZ and MCP. Mechanochemistry was used as the prime technique for cocrystal, amorphous and coamorphous production. After ball milling, samples were characterized by calorimetric methods, namely DSC, PLTM, and TG-DTA; and spectroscopic methods, these being FTIR-ATR, XRPD and SCXRD.

Solvates were obtained with ACN, MeOH and DMF, but not with Ace, EtOH, EtOAc, and DMSO. Additionally, the structure of IGU:DMF was solved with SCXRD, following obtention of monocrystalline crystals. Since the pharmaceutical applicability of these forms is usually limited, due to non-ideal physicochemical property modifications upon solvate formation, and heavy legislation limitations on the commercialization of drugs with residual solvents, solvate formation was mostly addressed for characterization purposes.

A new IGU polymorphic form was also found, although as a mixture of forms, by crystallization in DMSO, this being the first polymorph obtained by solvent evaporation. Finding a more efficient method for replicating this polymorph is crucial for further characterizing it, as solvent evaporation methods with DMSO are not practical.

A cocrystal was successfully obtained with LEF, in a molar ratio of 2:1 (IGU:LEF), by LAG at 15 Hz for 30 minutes with EtOAc. This new solid form is a dual drug cocrystal, being that both of these drugs are DMARDs used in treatment of RA, and have shown positive results in monotherapy, and in combinatory therapy, together with methotrexate. This new solid form has significant pharmaceutical potential for treatment of RA, as it could not only show improved physicochemical characteristics over its pure components, but also pave the way for discovering a possible synergetic effect between these two drugs.

Coamorphous formation was achieved with LEF (1:1), SSZ (1:1), NA (1:1 and 1:2), and FA (1:1), with NG in steel vessels at 30 Hz for 60 minutes. The solid with LEF remained stable for a period of 3 months, and the one with FA was stable after 6 months. The 1:2 solid with NA proved stable also after 3 months, unlike the one in a 1:1 molar ratio, which crystallized during the 3 months process, resulting in a 1:1 cocrystal, which had been studied in a previous work. The higher stability of the 1:2 coamorphous over the 1:1 was attributed to molecular interactions, of which evidence was found for the 1:2 solid, but not for the 1:1 solid, suggesting these helped stabilize the amorphous form.

Future investigation on the developed cocrystal and coamorphous systems with IGU could involve proper stability tests, performed under controlled temperature, pressure, and humidity conditions, over extended periods of time. These will help to determine their pharmaceutical potential. Also, finding effective methodologies for amorphous form stabilization is pivotal for upcoming studies with these forms. Dissolution studies

would also be of interest, not only with the cocrystal and the coamorphous, but also with IGU in amorphous form, as they would give a direct insight into possible solubility enhancements from these formulations.

For the IGU studies in solution, an initial characterization was made. It was discovered that this compound exists in two different species while in solution: a neutral one, and a deprotonated one. Furthermore, the deprotonated form was found to be fluorescent (Φ_F = 0.0779), while the neutral form showed not to be (Φ_F = 0.0007). From calculated pK_a (pK_a = 6.3), species incidence was calculated as a function of pH, showing that the deprotonated form has an incidence of 93% at physiological pH. This was thought to hinder IGU's partition to and permeation through biologic membranes, as charged molecules tend to have lower lipophilicity. Following studies, however, contradicted this theory. The molar absorption coefficient was also calculated, with UV-Vis (ε_{IGU} (347 nm) = 1.44 x 10^4 $M^{-1}cm^{-1}$).

Lipid interactions studies were performed with POPC and POPC:DDAB (9:1), following a partition model. IGU showed good partitioning to POPC (K_L = 4.60 x 10^1 [7, 106]), and even better partitioning to POPC:DDAB (9:1) (K_L = 1.46 x 10^2 [107, 193]), which was expected, since IGU is mostly negatively charged at the pH value that these studies were conducted (pH = 7.4), and POPC:DDAB forms positively charged vesicles in solution.

Permeation through POPC large unilamellar vesicles was also studied. Data collected suggested that IGU rapidly permeated the POPC LUVs, which rendered most of the results obtained in this experiment as inconclusive, as it was design to determine the permeation velocity for slow permeating compounds. IGU desorption from and permeation through the lipid bilayer was showed to occur in a time scale comparable to that of elution from the chromatographic columns.

Alternative methodologies for quantifying the permeation rate of IGU may comprise the use of fluorescent probes, sensitive to the pH of the liquid environment, as these would enable following IGU's permeation though the LUVs overtime, since it is mostly negatively charged at physiological pH, and consequently lowers the pH of the surrounding medium.

REFERENCES

(1) Samhouri, B. F.; Vassallo, R.; Achenbach, S. J.; Kronzer, V. L.; Davis, J. M.; Myasoedova, E.; Crowson, C. S. Incidence, Risk Factors, and Mortality of Clinical and Subclinical Rheumatoid Arthritis–Associated Interstitial Lung Disease: A Population-Based Cohort. *Arthritis Care Res (Hoboken)* **2022**. https://doi.org/10.1002/acr.24856.

(2) Gaffo, A.; Saag, K. G.; Curtis, J. R. Treatment of Rheumatoid Arthritis. *American Journal of Health-System Pharmacy* **2006**, *63* (24), 2451–2465. https://doi.org/10.2146/ajhp050514.

(3) Burmester, G. R.; Pope, J. E. Novel Treatment Strategies in Rheumatoid Arthritis. *The Lancet* **2017**, *389* (10086), 2338–2348. https://doi.org/10.1016/S0140-6736(17)31491-5.

(4) Koncz, T.; Pentek, M.; Brodszky, V.; Ersek, K.; Orlewska, E.; Gulacsi, L. Adherence to Biologic DMARD Therapies in Rheumatoid Arthritis. *Expert Opin Biol Ther* **2010**, *10* (9), 1367–1378. https://doi.org/10.1517/14712598.2010.510508.

(5) Prasad, P.; Verma, S.; Surbhi; Ganguly, N. K.; Chaturvedi, V.; Mittal, S. A. Rheumatoid Arthritis: Advances in Treatment Strategies. *Mol Cell Biochem* **2022**. https://doi.org/10.1007/s11010-022-04492-3.

(6) Tanaka, K.; Yamaguchi, T.; Hara, M. Iguratimod for the Treatment of Rheumatoid Arthritis in Japan. *Expert Rev Clin Immunol* **2015**, *11* (5), 565–573. https://doi.org/10.1586/1744666X.2015.1027151.

(7) Yoshikawa, A.; Kotani, T.; Matsuda, S.; Hata, K.; Matsumura, Y.; Takeuchi, T. The Addition of Iguratimod Can Reduce Methotrexate Dose in Rheumatoid Arthritis with Clinical Remission. *Mod Rheumatol* **2022**, *32* (1), 68–73. https://doi.org/10.1080/14397595.2021.1892945.

(8) Hu, C.-J.; Zhang, L.; Zhou, S.; Jiang, N.; Zhao, J.-L.; Wang, Q.; Tian, X.-P.; Zeng, X.-F. Effectiveness of Iguratimod as Monotherapy or Combined Therapy in Patients with Rheumatoid Arthritis: A Systematic Review and Meta-Analysis of RCTs. *J Orthop Surg Res* **2021**, *16* (1), 457. https://doi.org/10.1186/s13018-021-02603-2.

(9) Hara, M.; Ishiguro, N.; Katayama, K.; Kondo, M.; Sumida, T.; Mimori, T.; Soen, S.; Nagai, K.; Yamaguchi, T.; Yamamoto, K. Safety and Efficacy of Combination Therapy of Iguratimod with Methotrexate for Patients with Active Rheumatoid Arthritis with an Inadequate Response to Methotrexate: An Open-Label Extension of a Randomized, Double-Blind, Placebo-Controlled Trial. *Mod Rheumatol* **2014**, *24* (3), 410–418. https://doi.org/10.3109/14397595.2013.843756.

(10) Duan, X.-W.; Zhang, X.-L.; Mao, S.-Y.; Shang, J.-J.; Shi, X.-D. Efficacy and Safety Evaluation of a Combination of Iguratimod and Methotrexate Therapy for Active Rheumatoid Arthritis Patients: A Randomized Controlled Trial. *Clin Rheumatol* **2015**, *34* (9), 1513–1519. https://doi.org/10.1007/s10067-015-2999-6.

(11) Xiao, F.; Zhang, F.; Zhang, L. ling; Wei, W. A Randomized Phase I Study to Evaluate the Safety, Tolerability, Pharmacokinetics and Food-Effect of Iguratimod in Healthy Adult Volunteers. *Eur J Clin Pharmacol* **2018**, *74* (1), 69–77. https://doi.org/10.1007/s00228-017-2342-z.

(12) Li, Y.; Li, K.; Zhao, Z.; Wang, Y.; Jin, J.; Guo, J.; Zhang, J.; Zhang, J.; Zhu, J.; Huang, F. Randomised, Double-Blind, Placebo-Controlled Study of Iguratimod in the Treatment of Active Spondyloarthritis. *Front Med (Lausanne)* **2021**, *8*. https://doi.org/10.3389/fmed.2021.678864.

(13) Xia, Z.; Lyu, J.; Hou, N.; Song, L.; Li, X.; Liu, H. Iguratimod in Combination with Methotrexate in Active Rheumatoid Arthritis. *Z Rheumatol* **2016**, *75* (8), 828–833. https://doi.org/10.1007/s00393-015-1641-y.

(14) Jiang, H.; Gao, H.; Wang, Q.; Wang, M.; Wu, B. Molecular Mechanisms and Clinical Application of Iguratimod: A Review. *Biomedicine and Pharmacotherapy* **2020**, *122* (September 2019), 109704. https://doi.org/10.1016/j.biopha.2019.109704.

(15) Pu, J.; Wang, X.; Riaz, F.; Zhang, T.; Gao, R.; Pan, S.; Wu, Z.; Liang, Y.; Zhuang, S.; Tang, J. Effectiveness and Safety of Iguratimod in Treating Primary Sjögren's Syndrome: A Systematic Review and Meta-Analysis. *Front Pharmacol* **2021**, *12*. https://doi.org/10.3389/fphar.2021.621208.

(16) Kang, Y.; Yan, Q.; Fu, Q.; Wang, R.; Dai, M.; Du, F.; Dai, Q.; Ye, P.; Wu, C.; Lu, L.; Bao, C. Iguratimod as an Alternative Induction Therapy for Refractory Lupus Nephritis: A Preliminary Investigational Study. *Arthritis Res Ther* **2020**, *22* (1), 65. https://doi.org/10.1186/s13075-020-02154-7.

(17) 梅林雨; 梁忠信; 王杏林; 高晶. Iguratimod Crystal Form and Its Composition. CN1944420A, 2005.

(18) Song, J.; Liu, H.; Zhu, Q.; Miao, Y.; Wang, F.; Yang, F.; Cheng, W.; Xi, Y.; Niu, X.; He, D.; Chen, G. T-614 Promotes Osteoblastic Cell Differentiation by Increasing Dlx5 Expression and Regulating the Activation of P38 and NF- κ B. *Biomed Res Int* **2018**, *2018*, 1–8. https://doi.org/10.1155/2018/4901591.

(19) Li, J.; Bao, J.; Zeng, J.; Yan, A.; Zhao, C.; Shu, Q. Iguratimod: A Valuable Remedy from the Asia Pacific Region for Ameliorating Autoimmune Diseases and Protecting Bone Physiology. *Bone Res* **2019**, *7* (1), 27. https://doi.org/10.1038/s41413-019-0067-6.

(20) Mu, R.; Li, C.; Li, X.; Ke, Y.; Zhao, L.; Chen, L.; Wu, R.; Wu, Z.; Zuo, X.; Xie, Y.; Chen, J.; Wei, W.; Liu, Y.; Li, Z.; Dai, L.; Sun, L.; Liu, X.; Li, Z. Effectiveness and Safety of Iguratimod Treatment in Patients with Active Rheumatoid Arthritis in Chinese: A Nationwide, Prospective Real-World Study. *Lancet Reg Health West Pac* **2021**, *10* (49), 100128. https://doi.org/10.1016/j.lanwpc.2021.100128.

(21) Liu, T.; Zhang, L.; Joo, D.; Sun, S. C. NF-KB Signaling in Inflammation. *Signal Transduct Target Ther* **2017**, *2* (April). https://doi.org/10.1038/sigtrans.2017.23.

(22) Wu, L.; Zepp, J.; Li, X. Function of Act1 in IL-17 Family Signaling and Autoimmunity. In *Advances in Experimental Medicine and Biology*; 2012; Vol. 946, pp 223–235. https://doi.org/10.1007/978-1-4614-0106-3_13.

(23) Tanaka, K. Inhibitory Effects of an Anti-Rheumatic Agent T-614 on Immunoglobulin Production by Cultured B Cells and Rheumatoid Synovial Tissues Engrafted into SCID Mice. *Rheumatology* **2003**, *42* (11), 1365–1371. https://doi.org/10.1093/rheumatology/keg381.

(24) Yan, Q.; Du, F.; Huang, X.; Fu, Q.; Chen, S.; Dai, D.; Bao, C. Prevention of Immune Nephritis by the Small Molecular Weight Immunomodulator Iguratimod in MRL/Lpr Mice. *PLoS One* **2014**, *9* (10), e108273. https://doi.org/10.1371/journal.pone.0108273.
(25) Sakai, JB. Pharmacokinetics: The Absorption, Distribution, and Excretion of Drugs. In *Practical Pharmacology for the Pharmacy Technician*; 2009; pp 27–40.
(26) Doogue, M. P.; Polasek, T. M. The ABCD of Clinical Pharmacokinetics. *Ther Adv Drug Saf* **2013**, *4* (1), 5–7. https://doi.org/10.1177/2042098612469335.
(27) Lipka, E.; Amidon, G. L. Setting Bioequivalence Requirements for Drug Development Based on Preclinical Data: Optimizing Oral Drug Delivery Systems. *Journal of Controlled Release* **1999**, *62* (1–2), 41–49. https://doi.org/10.1016/S0168-3659(99)00022-X.
(28) Lindenberg, M.; Kopp, S.; Dressman, J. B. Classification of Orally Administered Drugs on the World Health Organization Model List of Essential Medicines According to the Biopharmaceutics Classification System. *European Journal of Pharmaceutics and Biopharmaceutics* **2004**, *58* (2), 265–278. https://doi.org/10.1016/j.ejpb.2004.03.001.
(29) Mehta, M. *Biopharmaceutics Classification System Bcs: Development, Implementation, and Growth*; Inc, J. W. & S., Ed.; 2017.
(30) Dave, R. A.; Morris, M. E. Novel High/Low Solubility Classification Methods for New Molecular Entities. *Int J Pharm* **2016**, *511* (1), 111–126. https://doi.org/10.1016/j.ijpharm.2016.06.060.
(31) GONG, Y.; GRANT, D. J. W.; BRITTAIN, H. G. Principles of Solubility. In *Solvent Systems and Their Selection in Pharmaceutics and Biopharmaceutics*; Springer New York: New York, NY; pp 1–27. https://doi.org/10.1007/978-0-387-69154-1_1.
(32) Lorimer, J. W.; Cohen-Adad, R. Thermodynamics of Solubility. In *The Experimental Determination of Solubilities*; John Wiley & Sons, Ltd: Chichester, UK, 2004; pp 17–76. https://doi.org/10.1002/0470867833.ch1.
(33) Burger, A.; Ramberger, R. On the Polymorphism of Pharmaceuticals and Other Molecular Crystals. I. *Mikrochim Acta* **1979**, *72* (3–4), 259–271. https://doi.org/10.1007/BF01197379.
(34) Burger, A.; Ramberger, R. On the Polymorphism of Pharmaceuticals and Other Molecular Crystals. II. *Mikrochim Acta* **1979**, *72* (3–4), 273–316. https://doi.org/10.1007/BF01197380.
(35) Raza, K. Polymorphism: The Phenomenon Affecting the Performance of Drugs. *SOJ Pharm Pharm Sci* **2014**. https://doi.org/10.15226/2374-6866/1/2/00111.
(36) Kawakami, K. Reversibility of Enantiotropically Related Polymorphic Transformations from a Practical Viewpoint: Thermal Analysis of Kinetically Reversible/Irreversible Polymorphic Transformations. *J Pharm Sci* **2007**, *96* (5), 982–989. https://doi.org/10.1002/jps.20748.
(37) Caira, M. R. Sulfa Drugs as Model Cocrystal Formers. *Mol Pharm* **2007**, *4* (3), 310–316. https://doi.org/10.1021/mp070003j.
(38) Kumar, S.; Nanda, A. Pharmaceutical Cocrystals: An Overview. *Indian J Pharm Sci* **2017**, *79* (6). https://doi.org/10.4172/pharmaceutical-sciences.1000302.

(39) Yadav, A.; Shete, A.; Dabke, A.; Kulkarni, P.; Sakhare, S. Co-Crystals: A Novel Approach to Modify Physicochemical Properties of Active Pharmaceutical Ingredients. *Indian J Pharm Sci* **2009**, *71* (4), 359. https://doi.org/10.4103/0250-474X.57283.

(40) Karimi-Jafari, M.; Padrela, L.; Walker, G. M.; Croker, D. M. Creating Cocrystals: A Review of Pharmaceutical Cocrystal Preparation Routes and Applications. *Cryst Growth Des* **2018**, *18* (10), 6370–6387. https://doi.org/10.1021/acs.cgd.8b00933.

(41) Perlovich, G. L. Thermodynamic Characteristics of Cocrystal Formation and Melting Points for Rational Design of Pharmaceutical Two-Component Systems. *CrystEngComm* **2015**, *17* (37), 7019–7028. https://doi.org/10.1039/C5CE00992H.

(42) Kumar Bandaru, R.; Rout, S. R.; Kenguva, G.; Gorain, B.; Alhakamy, N. A.; Kesharwani, P.; Dandela, R. Recent Advances in Pharmaceutical Cocrystals: From Bench to Market. *Front Pharmacol* **2021**, *12*. https://doi.org/10.3389/fphar.2021.780582.

(43) Fukte, S. R.; Wagh, M. P.; Rawat, S. COFORMER SELECTION: AN IMPORTANT TOOL IN COCRYSTAL FORMATION. *Int J Pharm Pharm Sci* **2014**, *6* (7 SE-Review Article(s)), 9–14.

(44) Koranne, S.; Krzyzaniak, J. F.; Luthra, S.; Arora, K. K.; Suryanarayanan, R. Role of Coformer and Excipient Properties on the Solid-State Stability of Theophylline Cocrystals. *Cryst Growth Des* **2019**, *19* (2), 868–875. https://doi.org/10.1021/acs.cgd.8b01430.

(45) Yuliandra, Y.; Zaini, E.; Syofyan, S.; Pratiwi, W.; Putri, L.; Pratiwi, Y.; Arifin, H. Cocrystal of Ibuprofen–Nicotinamide: Solid-State Characterization and In Vivo Analgesic Activity Evaluation. *Sci Pharm* **2018**, *86* (2), 23. https://doi.org/10.3390/scipharm86020023.

(46) Silva, P. N. S. L.; Maria, T. M. R.; Eusébio, M. E. S. Investigação de Formas Sólidas de Um Fármaco Usado No Tratamento Da Artrite Reumatoide: Iguratimode - Internship Report for the Subject "Estágio." **2019**.

(47) E. Castro, R. A.; Ribeiro, J. D. B.; Maria, T. M. R.; Ramos Silva, M.; Yuste-Vivas, C.; Canotilho, J.; Eusébio, M. E. S. Naproxen Cocrystals with Pyridinecarboxamide Isomers. *Cryst Growth Des* **2011**, *11* (12), 5396–5404. https://doi.org/10.1021/cg2009946.

(48) Wang, X.; Du, S.; Zhang, R.; Jia, X.; Yang, T.; Zhang, X. Drug-Drug Cocrystals: Opportunities and Challenges. *Asian J Pharm Sci* **2021**, *16* (3), 307–317. https://doi.org/10.1016/j.ajps.2020.06.004.

(49) Ngilirabanga, J. B.; Rosa, P. P.; Aucamp, M.; Kippie, Y.; Samsodien, H. Dual-Drug Co-Crystal Synthesis for Synergistic in Vitro Effect of Three Key First-Line Antiretroviral Drugs. *J Drug Deliv Sci Technol* **2020**, *60*, 101958. https://doi.org/10.1016/j.jddst.2020.101958.

(50) Guo, C.; Zhang, Q.; Zhu, B.; Zhang, Z.; Ma, X.; Dai, W.; Gong, X.; Ren, G.; Mei, X. Drug–Drug Cocrystals Provide Significant Improvements of Drug Properties in Treatment with Progesterone. *Cryst Growth Des* **2020**, *20* (5), 3053–3063. https://doi.org/10.1021/acs.cgd.9b01688.

(51) Hasa, D.; Schneider Rauber, G.; Voinovich, D.; Jones, W. Cocrystal Formation through Mechanochemistry: From Neat and Liquid-Assisted Grinding to Polymer-Assisted Grinding. *Angewandte Chemie International Edition* **2015**, *54* (25), 7371–7375. https://doi.org/10.1002/anie.201501638.
(52) Hossain Mithu, M. S.; Ross, S. A.; Hurt, A. P.; Douroumis, D. Effect of Mechanochemical Grinding Conditions on the Formation of Pharmaceutical Cocrystals and Co-Amorphous Solid Forms of Ketoconazole – Dicarboxylic Acid. *J Drug Deliv Sci Technol* **2021**, *63*, 102508. https://doi.org/10.1016/j.jddst.2021.102508.
(53) Chadha, R.; Kuhad, A.; Arora, P.; Kishor, S. Characterisation and Evaluation of Pharmaceutical Solvates of Atorvastatin Calcium by Thermoanalytical and Spectroscopic Studies. *Chem Cent J* **2012**, *6* (1), 1–15. https://doi.org/10.1186/1752-153X-6-114.
(54) Healy, A. M.; Worku, Z. A.; Kumar, D.; Madi, A. M. Pharmaceutical Solvates, Hydrates and Amorphous Forms: A Special Emphasis on Cocrystals. *Adv Drug Deliv Rev* **2017**, *117*, 25–46. https://doi.org/10.1016/j.addr.2017.03.002.
(55) Karki, S.; Friščić, T.; Jones, W.; Motherwell, W. D. S. Screening for Pharmaceutical Cocrystal Hydrates via Neat and Liquid-Assisted Grinding. *Mol Pharm* **2007**, *4* (3), 347–354. https://doi.org/10.1021/mp0700054.
(56) Qi, S.; McAuley, W. J.; Yang, Z.; Tipduangta, P. Physical Stabilization of Low-Molecular-Weight Amorphous Drugs in the Solid State: A Material Science Approach. *Ther Deliv* **2014**, *5* (7), 817–841. https://doi.org/10.4155/tde.14.39.
(57) Gurunath, S.; Pradeep Kumar, S.; Basavaraj, N. K.; Patil, P. A. Amorphous Solid Dispersion Method for Improving Oral Bioavailability of Poorly Water-Soluble Drugs. *J Pharm Res* **2013**, *6* (4), 476–480. https://doi.org/10.1016/j.jopr.2013.04.008.
(58) Murdande, S. B.; Pikal, M. J.; Shanker, R. M.; Bogner, R. H. Solubility Advantage of Amorphous Pharmaceuticals: I. A Thermodynamic Analysis. *J Pharm Sci* **2010**, *99* (3), 1254–1264. https://doi.org/10.1002/jps.21903.
(59) Turnbull, D. Under What Conditions Can A Glass Be Formed? *Contemp Phys* **1969**, *10* (5), 473–488. https://doi.org/10.1080/00107516908204405.
(60) Debenedetti, P. G.; Stillinger, F. H. Supercooled Liquids and the Glass Transition. *Nature* **2001**, *410* (6825), 259–267. https://doi.org/10.1038/35065704.
(61) Uhlmann, D. R. Crystallization and Glass Formation. *J Non Cryst Solids* **1985**, *73* (1–3), 585–592. https://doi.org/10.1016/0022-3093(85)90377-1.
(62) Dengale, S. J.; Grohganz, H.; Rades, T.; Löbmann, K. Recent Advances in Co-Amorphous Drug Formulations. *Adv Drug Deliv Rev* **2016**, *100*, 116–125. https://doi.org/10.1016/j.addr.2015.12.009.
(63) Han, J.; Wei, Y.; Lu, Y.; Wang, R.; Zhang, J.; Gao, Y.; Qian, S. Co-Amorphous Systems for the Delivery of Poorly Water-Soluble Drugs: Recent Advances and an Update. *Expert Opin Drug Deliv* **2020**, *17* (10), 1411–1435. https://doi.org/10.1080/17425247.2020.1796631.

(64) Liu, J.; Grohganz, H.; Löbmann, K.; Rades, T.; Hempel, N.-J. Co-Amorphous Drug Formulations in Numbers: Recent Advances in Co-Amorphous Drug Formulations with Focus on Co-Formability, Molar Ratio, Preparation Methods, Physical Stability, In Vitro and In Vivo Performance, and New Formulation Strategies. *Pharmaceutics* **2021**, *13* (3), 389. https://doi.org/10.3390/pharmaceutics13030389.

(65) Su, M.; Xia, Y.; Shen, Y.; Heng, W.; Wei, Y.; Zhang, L.; Gao, Y.; Zhang, J.; Qian, S. A Novel Drug–Drug Coamorphous System without Molecular Interactions: Improve the Physicochemical Properties of Tadalafil and Repaglinide. *RSC Adv* **2020**, *10* (1), 565–583. https://doi.org/10.1039/C9RA07149K.

(66) Löbmann, K.; Strachan, C.; Grohganz, H.; Rades, T.; Korhonen, O.; Laitinen, R. Co-Amorphous Simvastatin and Glipizide Combinations Show Improved Physical Stability without Evidence of Intermolecular Interactions. *European Journal of Pharmaceutics and Biopharmaceutics* **2012**, *81* (1), 159–169. https://doi.org/10.1016/j.ejpb.2012.02.004.

(67) Dengale, S. J.; Ranjan, O. P.; Hussen, S. S.; Krishna, B. S. M.; Musmade, P. B.; Gautham Shenoy, G.; Bhat, K. Preparation and Characterization of Co-Amorphous Ritonavir–Indomethacin Systems by Solvent Evaporation Technique: Improved Dissolution Behavior and Physical Stability without Evidence of Intermolecular Interactions. *European Journal of Pharmaceutical Sciences* **2014**, *62*, 57–64. https://doi.org/10.1016/j.ejps.2014.05.015.

(68) Dendooven, A. Leflunomide and Methotrexate Combination Therapy in Daily Clinical Practice. *Ann Rheum Dis* **2006**, *65* (6), 833–834. https://doi.org/10.1136/ard.2005.043620.

(69) Capell, H. A.; Madhok, R.; Porter, D. R.; Munro, R. A. L.; McInnes, I. B.; Hunter, J. A.; Steven, M.; Zoma, A.; Morrison, E.; Sambrook, M.; Wui Poon, F.; Hampson, R.; McDonald, F.; Tierney, A.; Henderson, N.; Ford, I. Combination Therapy with Sulfasalazine and Methotrexate Is More Effective than Either Drug Alone in Patients with Rheumatoid Arthritis with a Suboptimal Response to Sulfasalazine: Results from the Double-Blind Placebo-Controlled MASCOT Study. *Ann Rheum Dis* **2006**, *66* (2), 235–241. https://doi.org/10.1136/ard.2006.057133.

(70) Cadden, J.; Klooster, W. T.; Coles, S. J.; Aitipamula, S. Cocrystals of Leflunomide: Design, Structural, and Physicochemical Evaluation. *Cryst Growth Des* **2019**, *19* (7), 3923–3933. https://doi.org/10.1021/acs.cgd.9b00335.

(71) Shea, B.; Swinden, M. V; Tanjong Ghogomu, E.; Ortiz, Z.; Katchamart, W.; Rader, T.; Bombardier, C.; Wells, G. A.; Tugwell, P. Folic Acid and Folinic Acid for Reducing Side Effects in Patients Receiving Methotrexate for Rheumatoid Arthritis. *Cochrane Database of Systematic Reviews* **2013**, *2014* (7). https://doi.org/10.1002/14651858.CD000951.pub2.

(72) Skieneh, J. M.; Sathisaran, I.; Dalvi, S. V.; Rohani, S. Co-Amorphous Form of Curcumin–Folic Acid Dihydrate with Increased Dissolution Rate. *Cryst Growth Des* **2017**, *17* (12), 6273–6280. https://doi.org/10.1021/acs.cgd.7b00947.

(73) ALBIBI, R. Metoclopramide: Pharmacology and Clinical Application. *Ann Intern Med* **1983**, *98* (1), 86. https://doi.org/10.7326/0003-4819-98-1-86.

(74) Wallmark, B. Mechanism of Action of Omeprazole. *Scand J Gastroenterol* **1986**, *21* (sup118), 11–16. https://doi.org/10.3109/00365528609090881.

(75) Watson, H. Biological Membranes. *Essays Biochem* **2015**, *59*, 43–69. https://doi.org/10.1042/bse0590043.
(76) Zeno, W. F.; Day, K. J.; Gordon, V. D.; Stachowiak, J. C. Principles and Applications of Biological Membrane Organization. *Annu Rev Biophys* **2020**, *49* (1), 19–39. https://doi.org/10.1146/annurev-biophys-121219-081637.
(77) Fernández-Vidal, M.; White, S. H.; Ladokhin, A. S. Membrane Partitioning: "Classical" and "Nonclassical" Hydrophobic Effects. *J Membr Biol* **2011**, *239* (1–2), 5–14. https://doi.org/10.1007/s00232-010-9321-y.
(78) Frolov, V. A.; Zimmerberg, J. Cooperative Elastic Stresses, the Hydrophobic Effect, and Lipid Tilt in Membrane Remodeling. *FEBS Lett* **2010**, *584* (9), 1824–1829. https://doi.org/10.1016/j.febslet.2010.01.039.
(79) Drescher, S.; van Hoogevest, P. The Phospholipid Research Center: Current Research in Phospholipids and Their Use in Drug Delivery. *Pharmaceutics* **2020**, *12* (12), 1235. https://doi.org/10.3390/pharmaceutics12121235.
(80) Vaz, W. L. C. Lipid Bilayers: Properties. In *Wiley Encyclopedia of Chemical Biology*; John Wiley & Sons, Inc.: Hoboken, NJ, USA, 2008. https://doi.org/10.1002/9780470048672.wecb281.
(81) Thakur, R.; Das, A.; Chakraborty, A. Interaction of Human Serum Albumin with Liposomes of Saturated and Unsaturated Lipids with Different Phase Transition Temperatures: A Spectroscopic Investigation by Membrane Probe PRODAN. *RSC Adv.* **2014**, *4* (28), 14335–14347. https://doi.org/10.1039/C4RA01214C.
(82) Rawicz, W.; Olbrich, K. C.; McIntosh, T.; Needham, D.; Evans, E. Effect of Chain Length and Unsaturation on Elasticity of Lipid Bilayers. *Biophys J* **2000**, *79* (1), 328–339. https://doi.org/10.1016/S0006-3495(00)76295-3.
(83) Mälkiä, A.; Murtomäki, L.; Urtti, A.; Kontturi, K. Drug Permeation in Biomembranes: In Vitro and in Silico Prediction and Influence of Physicochemical Properties. *European Journal of Pharmaceutical Sciences* **2004**, *23* (1), 13–47. https://doi.org/10.1016/j.ejps.2004.05.009.
(84) Moreno, M.; Teles Martins, P.; Bernardino, E.; Abel, B.; Ambudkar, S. Characterization of the Lipidome and Biophysical Properties of Membranes from High Five Insect Cells Expressing Mouse P-Glycoprotein. *Biomolecules* **2021**, *11* (3), 426. https://doi.org/10.3390/biom11030426.
(85) Feitosa, E.; Adati, R. D.; Alves, F. R. Thermal and Phase Behavior of Didodecyldimethylammonium Bromide Aqueous Dispersions. *Colloids Surf A Physicochem Eng Asp* **2015**, *480*, 253–259. https://doi.org/10.1016/j.colsurfa.2015.01.086.
(86) Engström, S.; Nordén, T. P.; Nyquist, H. Cubic Phases for Studies of Drug Partition into Lipid Bilayers. *European Journal of Pharmaceutical Sciences* **1999**, *8* (4), 243–254. https://doi.org/10.1016/S0928-0987(99)00012-3.
(87) Cardoso, R. M. S.; Filipe, H. A. L.; Gomes, F.; Moreira, N. D.; Vaz, W. L. C.; Moreno, M. J. Chain Length Effect on the Binding of Amphiphiles to Serum Albumin and to POPC Bilayers. *Journal of Physical Chemistry B* **2010**, *114* (49), 16337–16346. https://doi.org/10.1021/jp105163k.
(88) McNaught, A. D.; Wilkinson, A. *Compendium of Chemical Terminology*; Blackwell Science Oxford, 1997; Vol. 1669. https://doi.org/10.1351/goldbook.B00626.

(89) FLETCHER, A. N. QUININE SULFATE AS A FLUORESCENCE QUANTUM YIELD STANDARD. *Photochem Photobiol* **1969**, *9* (5), 439–444. https://doi.org/10.1111/j.1751-1097.1969.tb07311.x.
(90) Williams, A. T. R.; Winfield, S. A.; Miller, J. N. Relative Fluorescence Quantum Yields Using a Computer-Controlled Luminescence Spectrometer. *Analyst* **1983**, *108* (1290), 1067–1071. https://doi.org/10.1039/AN9830801067.
(91) Würth, C.; Grabolle, M.; Pauli, J.; Spieles, M.; Resch-Genger, U. Relative and Absolute Determination of Fluorescence Quantum Yields of Transparent Samples. *Nat Protoc* **2013**, *8* (8), 1535–1550. https://doi.org/10.1038/nprot.2013.087.
(92) Tan, C.-Y.; Huang, Y.-X. Dependence of Refractive Index on Concentration and Temperature in Electrolyte Solution, Polar Solution, Nonpolar Solution, and Protein Solution. *J Chem Eng Data* **2015**, *60* (10), 2827–2833. https://doi.org/10.1021/acs.jced.5b00018.
(93) Ferreira, T. M.; Coreta-Gomes, F.; Ollila, O. H. S.; Moreno, M. J.; Vaz, W. L. C.; Topgaard, D. Cholesterol and POPC Segmental Order Parameters in Lipid Membranes: Solid State 1 H– 13 C NMR and MD Simulation Studies. *Phys. Chem. Chem. Phys.* **2013**, *15* (6), 1976–1989. https://doi.org/10.1039/C2CP42738A.
(94) Martins, P. T.; Velazquez-Campoy, A.; Vaz, W. L. C.; Cardoso, R. M. S.; Valério, J.; Moreno, M. J. Kinetics and Thermodynamics of Chlorpromazine Interaction with Lipid Bilayers: Effect of Charge and Cholesterol. *J Am Chem Soc* **2012**, *134* (9), 4184–4195. https://doi.org/10.1021/ja209917q.
(95) Angelini, G.; Chiarini, M.; De Maria, P.; Fontana, A.; Gasbarri, C.; Siani, G.; Velluto, D. Characterization of Cationic Liposomes. Influence of the Bilayer Composition on the Kinetics of the Liposome Breakdown. *Chem Phys Lipids* **2011**, *164* (7), 680–687. https://doi.org/10.1016/j.chemphyslip.2011.07.002.
(96) Coppola, L.; Youssry, M.; Nicotera, I.; Gentile, L. Rheological Investigation of Thermal Transitions in Vesicular Dispersion. *J Colloid Interface Sci* **2009**, *338* (2), 550–557. https://doi.org/10.1016/j.jcis.2009.06.054.
(97) Hope, M. J.; Bally, M. B.; Webb, G.; Cullis, P. R. Production of Large Unilamellar Vesicles by a Rapid Extrusion Procedure. Characterization of Size Distribution, Trapped Volume and Ability to Maintain a Membrane Potential. *Biochimica et Biophysica Acta (BBA) - Biomembranes* **1985**, *812* (1), 55–65. https://doi.org/10.1016/0005-2736(85)90521-8.
(98) Prapulla, S. G.; Karanth, N. G. FERMENTATION (INDUSTRIAL) | Recovery of Metabolites. In *Encyclopedia of Food Microbiology*; Elsevier, 2014; pp 822–833. https://doi.org/10.1016/B978-0-12-384730-0.00109-9.
(99) Stetefeld, J.; McKenna, S. A.; Patel, T. R. Dynamic Light Scattering: A Practical Guide and Applications in Biomedical Sciences. *Biophys Rev* **2016**, *8* (4), 409–427. https://doi.org/10.1007/s12551-016-0218-6.
(100) Bhattacharjee, S. DLS and Zeta Potential – What They Are and What They Are Not? *Journal of Controlled Release* **2016**, *235*, 337–351. https://doi.org/10.1016/j.jconrel.2016.06.017.
(101) Yuan, L.; Lorenz, H. Solvate Formation of Bis(Demethoxy)Curcumin: Screening and Characterization. *Crystals (Basel)* **2018**, *8* (11), 407. https://doi.org/10.3390/cryst8110407.

(102) Caira, M. R.; Bettinetti, G.; Sorrenti, M.; Catenacci, L. PHARMACEUTICS, PREFORMULATION ANDDRUG DELIVERY. *J Pharm Sci* **2007**, *96* (5), 996–1007. https://doi.org/10.1002/jps.20934.
(103) Chadha, R.; Arora, P.; Kaur, R.; Saini, A.; Singla, M.; Jain, D. Characterization of Solvatomorphs of Methotrexate Using Thermoanalytical and Other Techniques. *Acta Pharmaceutica* **2009**, *59* (3). https://doi.org/10.2478/v10007-009-0024-9.
(104) Vega, D.; Petragalli, A.; Fernández, D.; Ellena, J. A. Polymorphism on Leflunomide: Stability and Crystal Structures. *J Pharm Sci* **2006**, *95* (5), 1075–1083. https://doi.org/10.1002/jps.20382.
(105) Luo, Q.; Sun, Y.; Liu, W.; Qian, C.; Jin, B.; Tao, F.; Gu, Y.; Wu, X.; Shen, Y.; Xu, Q. A Novel Disease-Modifying Antirheumatic Drug, Iguratimod, Ameliorates Murine Arthritis by Blocking IL-17 Signaling, Distinct from Methotrexate and Leflunomide. *The Journal of Immunology* **2013**, *191* (10), 4969–4978. https://doi.org/10.4049/jimmunol.1300832.
(106) Filip, L. A.; Caira, M. R.; Farcaş, S. I.; Bojiţa, M. T. Triclinic Polymorph of Sulfasalazine. *Acta Crystallogr C* **2001**, *57* (4), 435–436. https://doi.org/10.1107/S0108270100020771.
(107) Braga, D.; Chelazzi, L.; Grepioni, F.; Maschio, L.; Nanna, S.; Taddei, P. Folic Acid in the Solid State: A Synergistic Computational, Spectroscopic, and Structural Approach. *Cryst Growth Des* **2016**, *16* (4), 2218–2224. https://doi.org/10.1021/acs.cgd.6b00043.
(108) Vora, A.; Riga, A.; Dollimore, D.; Alexander, K. S. Thermal Stability of Folic Acid. *Thermochim Acta* **2002**, *392–393*, 209–220. https://doi.org/10.1016/S0040-6031(02)00103-X.
(109) Cruz-Cabeza, A. J.; Bernstein, J. Conformational Polymorphism. *Chem Rev* **2014**, *114* (4), 2170–2191. https://doi.org/10.1021/cr400249d.
(110) Martins, I. C. B.; Forte, A.; Diogo, H. P.; Raposo, L. R.; Baptista, P. V.; Fernandes, A. R.; Branco, L. C.; Duarte, M. T. A Solvent-free Strategy to Prepare Amorphous Salts of Folic Acid with Enhanced Solubility and Cell Permeability. *Chemistry–Methods* **2022**, *2* (6). https://doi.org/10.1002/cmtd.202100104.
(111) Wu, W.; Wang, Y.; Löbmann, K.; Grohganz, H.; Rades, T. Transformations between Co-Amorphous and Co-Crystal Systems and Their Influence on the Formation and Physical Stability of Co-Amorphous Systems. *Mol Pharm* **2019**, *16* (3), 1294–1304. https://doi.org/10.1021/acs.molpharmaceut.8b01229.
(112) Bi, Y.; Xiao, D.; Ren, S.; Bi, S.; Wang, J.; Li, F. The Binary System of Ibuprofen-Nicotinamide Under Nanoscale Confinement: From Cocrystal to Coamorphous State. *J Pharm Sci* **2017**, *106* (10), 3150–3155. https://doi.org/10.1016/j.xphs.2017.06.005.
(113) Toure, O.; Dussap, C.-G.; Lebert, A. Comparison of Predicted PK a Values for Some Amino-Acids, Dipeptides and Tripeptides, Using COSMO-RS, ChemAxon and ACD/Labs Methods. *Oil & Gas Science and Technology – Revue d'IFP Energies nouvelles* **2013**, *68* (2), 281–297. https://doi.org/10.2516/ogst/2012094.

APPENDIX 1

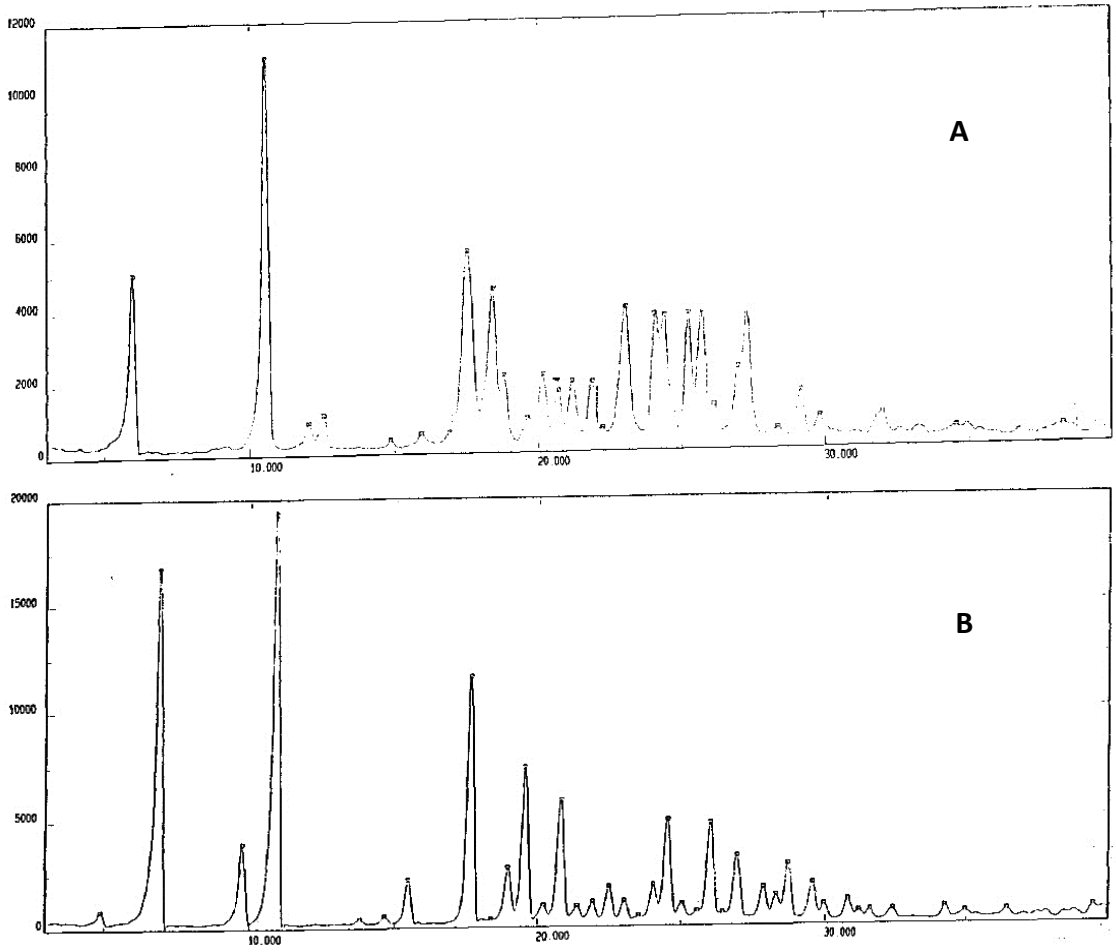

FIG. Apdx1-1 – XRPD diffractograms of IGU's forms I (**A**) and II (**B**). Adapted from REF.

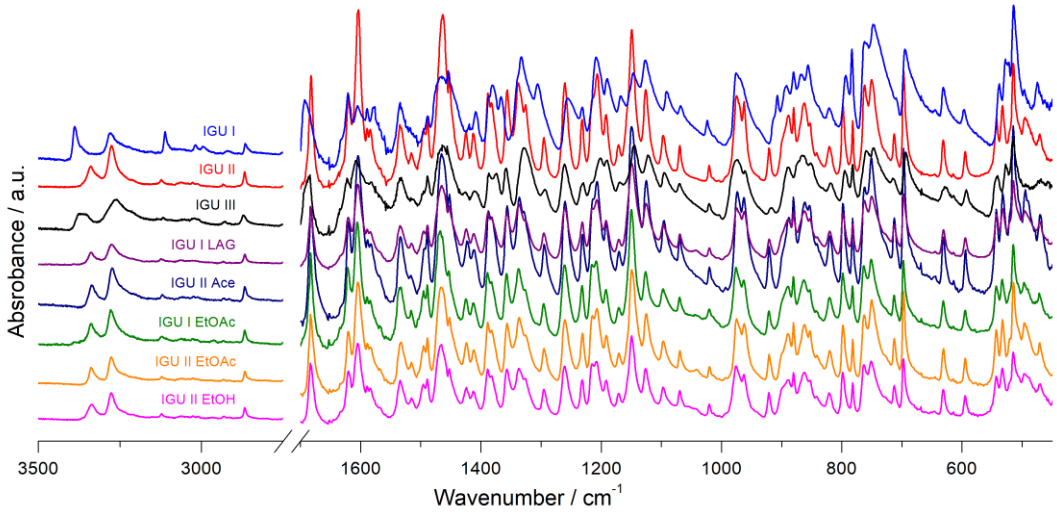

FIG. Apdx1-2 – FTIR-ATR spectra of various experiments in which IGU's form II was obtained.

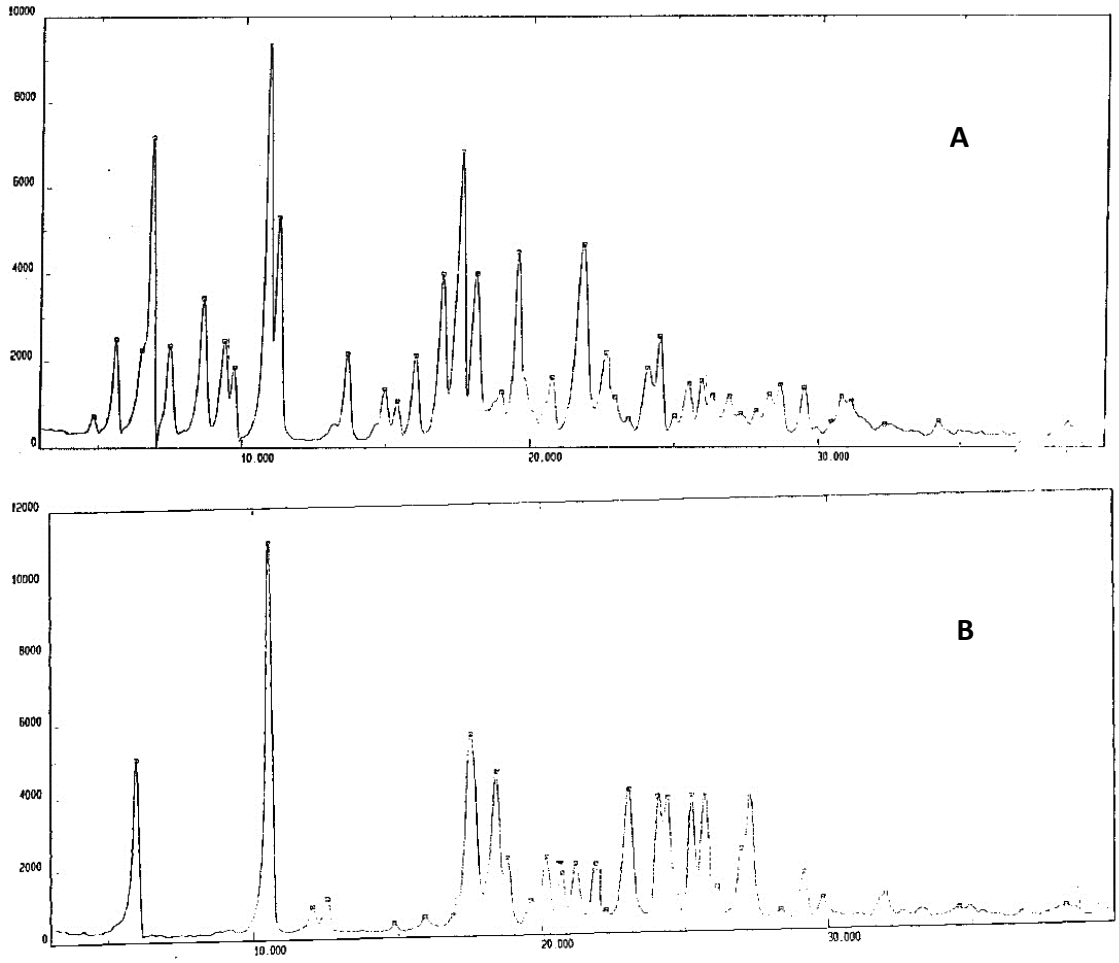

FIG. Apdx1-3 – XRPD diffractograms of IGU solvates with ACN (**A**) and DMF (**B**). Adapted from REF.

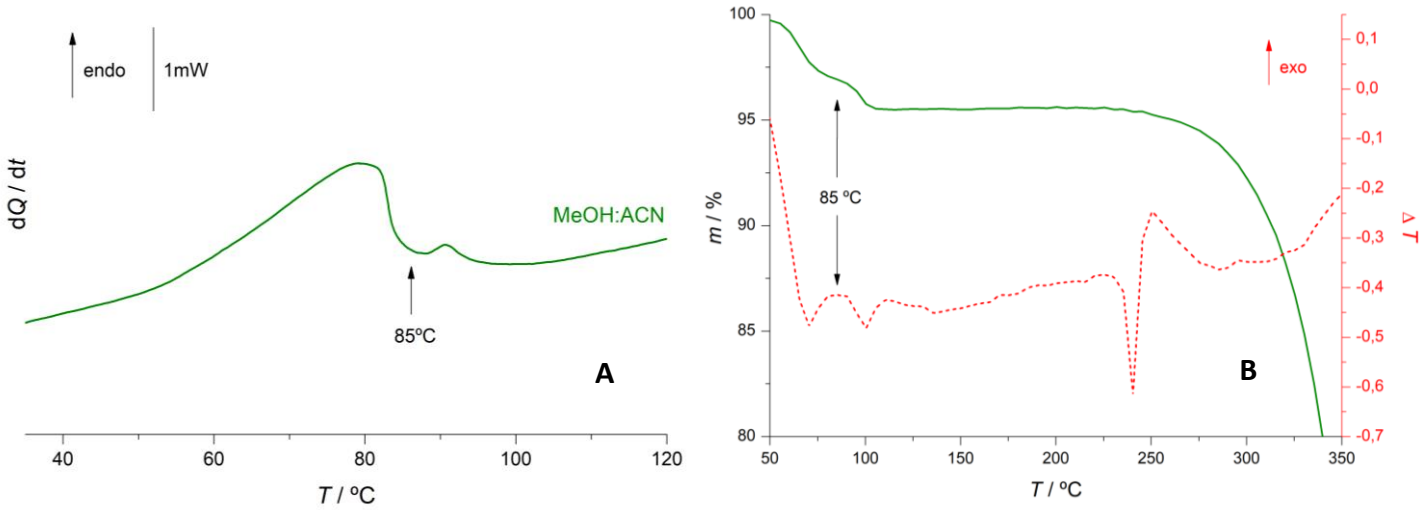

FIG. Apdx1-4 – DSC (**A**) and TG-DTA (**B**) curves of IGU crystallized from MeOH:ACN. β = 10 °C/min.

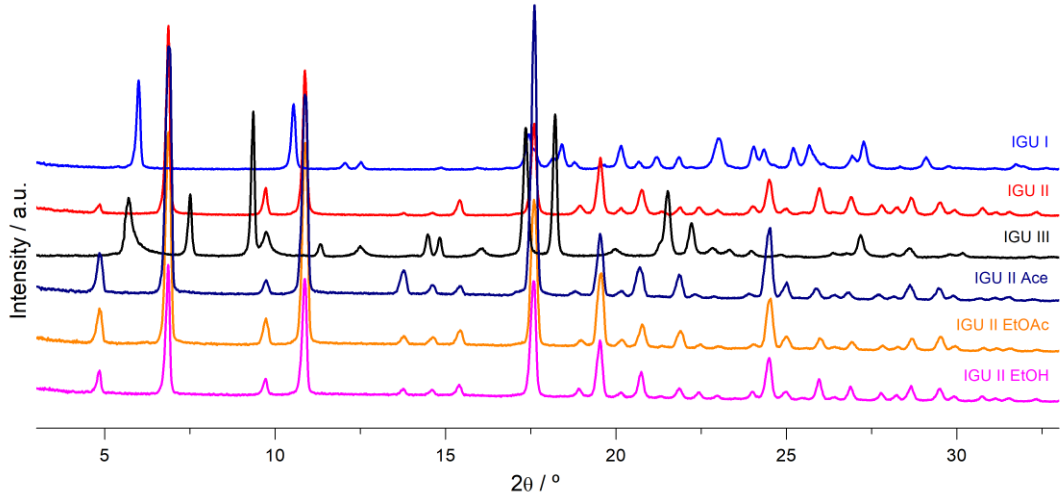

FIG. Apdx 1-5 – XRPD diffractogram of crystallizations from solvent, which resulted in IGU's form II.

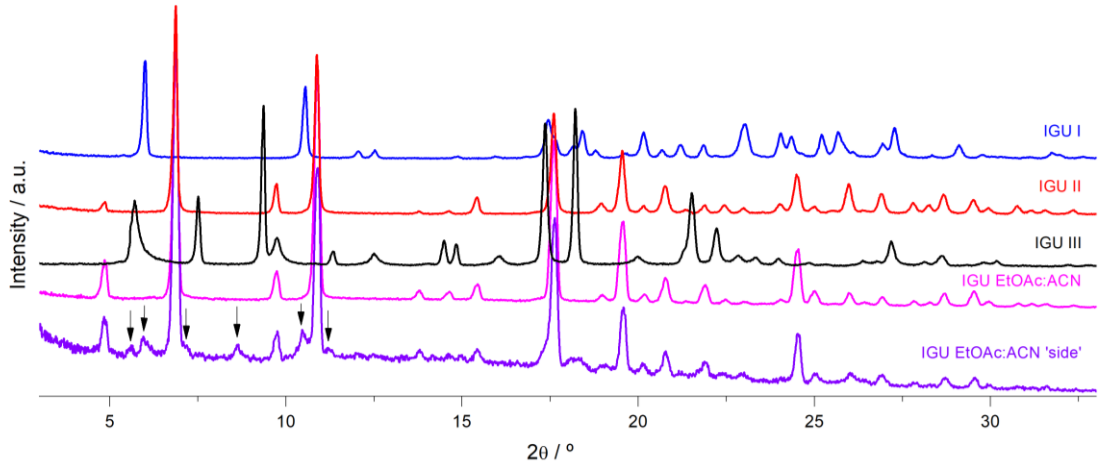

FIG. Apdx1-6 – XRPD diffractogram of IGU crystallizations with EtOAc and forms I, II and III. The 'side' crystal's distinct signals are marked by arrows.

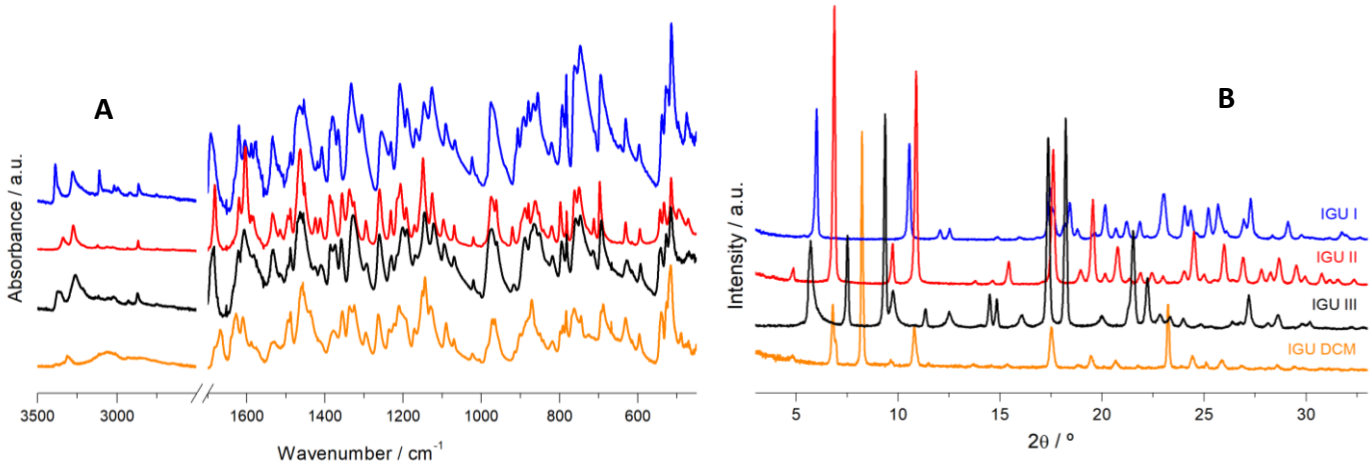

FIG. Apdx 1-7 – FTIR-ATR spectra (**A**) and XRPD diffractograms (**B**) of the solid crystallized from DCM and IGU's forms I, II and III.

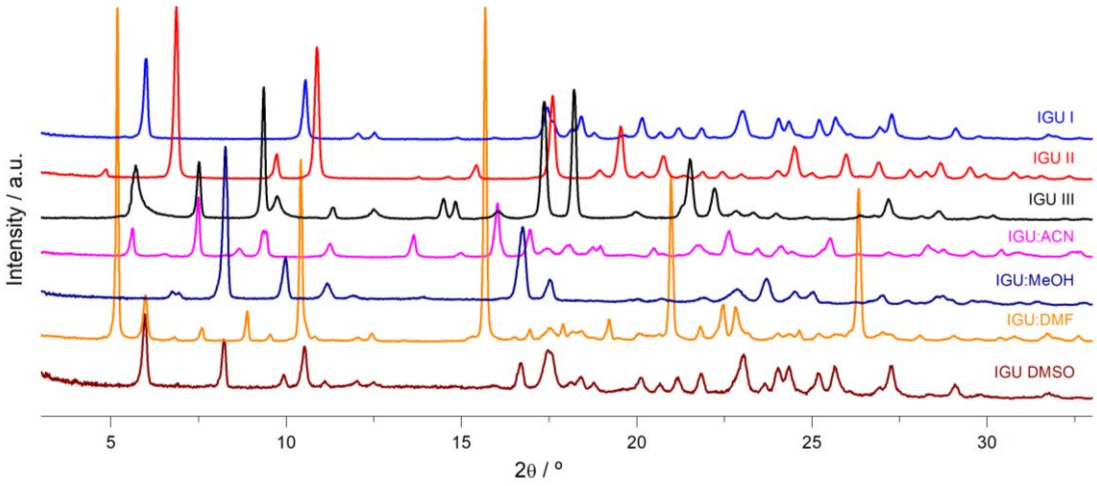

FIG. Apdx1-8 – XRPD diffractogram of IGU's forms I, II and III, the IGU solvates obtained with ACN, MeOH and DMF, and the solid crystallized from DMSO.

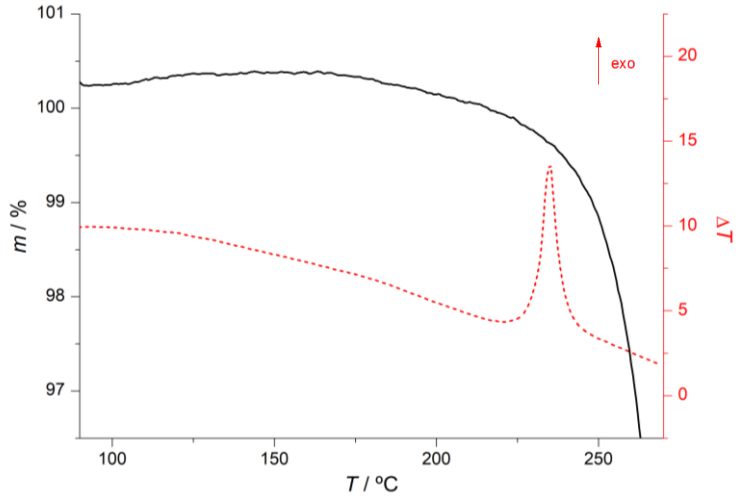

FIG. Apdx1-9 – TG and DTA curves of the IGU crystallized from DMSO (second run). β = 10 °C/min.

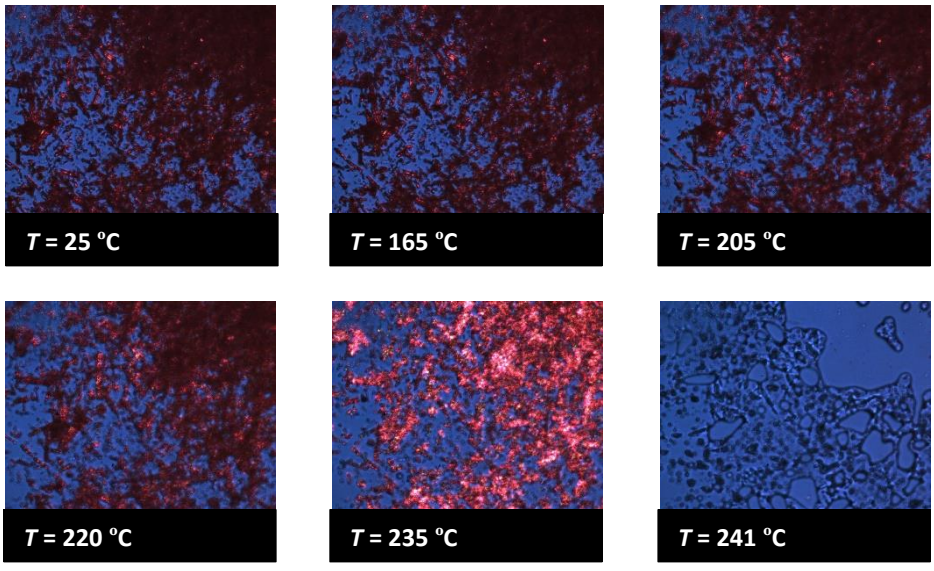

FIG. Apdx1-10 – Images captures during a PLTM run with IGU:DMSO. β = 10 °C/min.

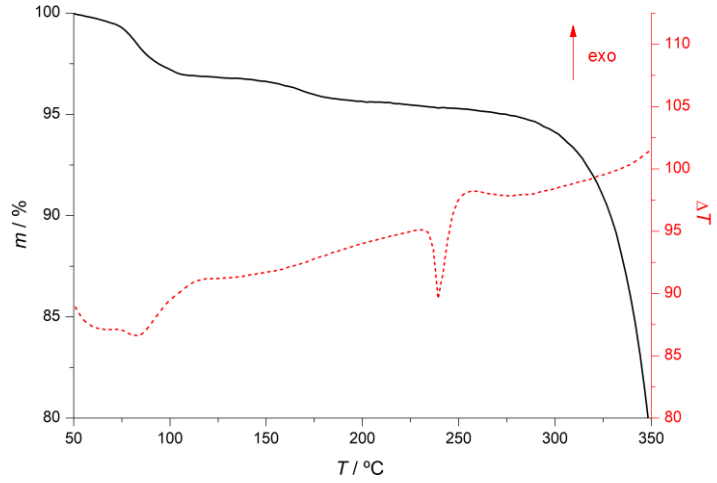

FIG. Apdx1-11 – TG and DTA curves of IGU's hydrate, formed during the dissolution tests.

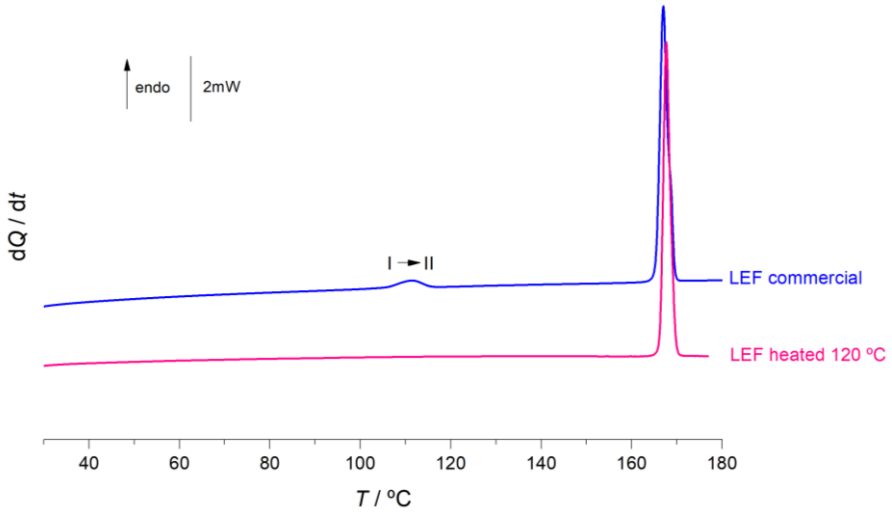

FIG. Apdx1-12 – DSC curves of commercial LEF and LEF preheated to 120 °C. β = 10 °C/min.

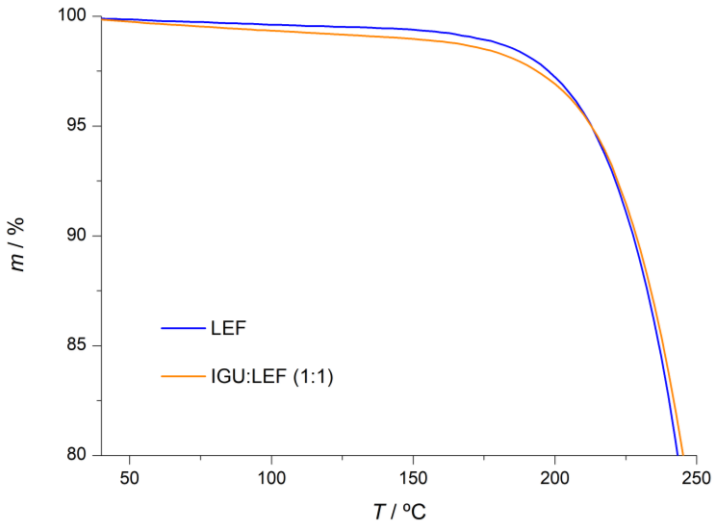

FIG. Apdx1-13 – TG curves of LEF, and IGU:LEF in a 1:1 molar ratio, obtained by LAG. β = 10 °C/min.

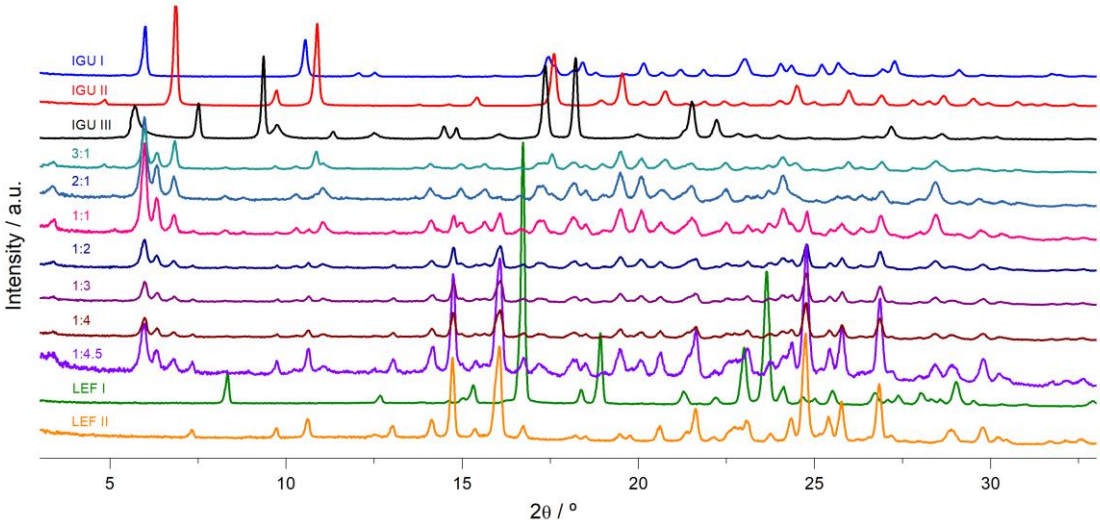

FIG. Apdx1-14 – XRPD diffractogram of the various molar ratios used to study the IGU:LEF system.

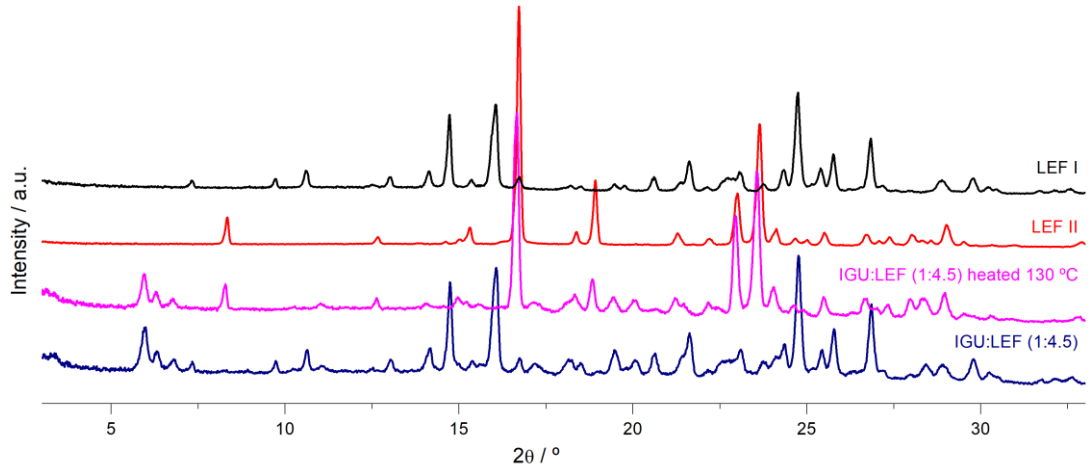

FIG. Apdx1-15 – XRPD diffractogram of the IGU:LEF 1:4.5 eutectic composition, the same sample preheated until 130 °C, and LEF polymorphs I and II.

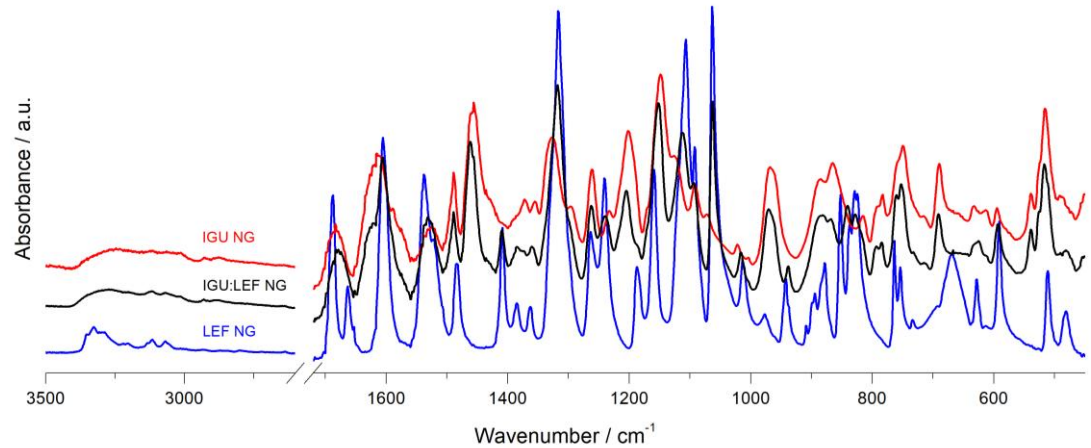

FIG. Apdx1-16 – FTIR-ATR spectra of IGU, LEF and IGU:LEF 1:1, submitted to neat grinding at 30 Hz for 60 minutes.

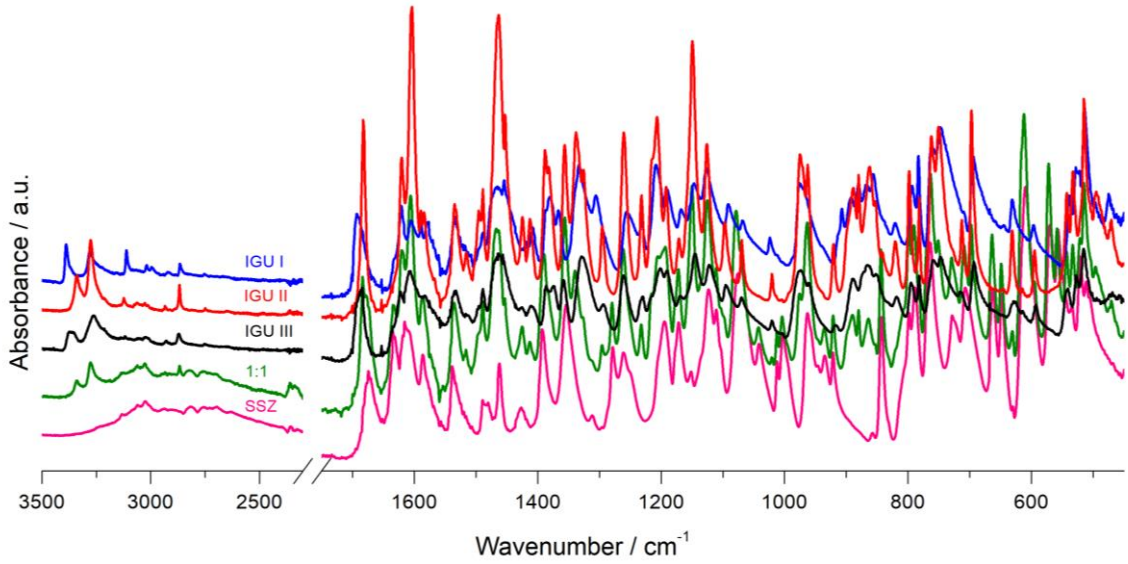

FIG. Apdx1-17 – FTIR-ATR spectra of SSZ, IGU' forms I, II and III, and the IGU:SSZ ample in a 1:1 molar ratio.

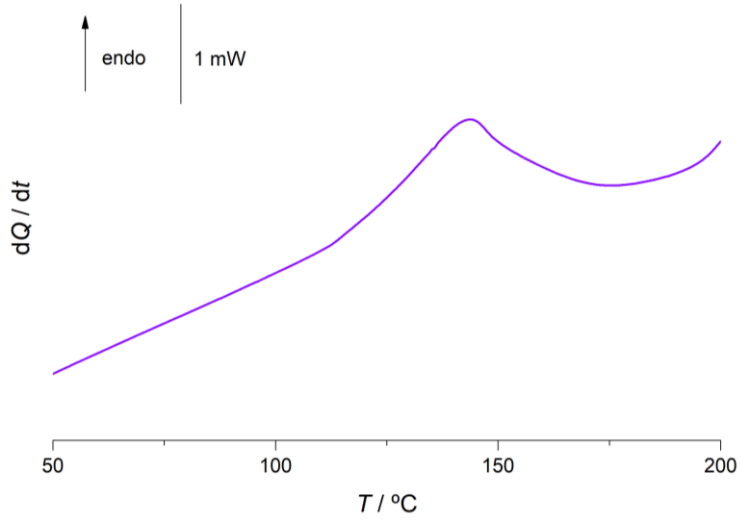

FIG. Apdx1-18 – DSC curve of a FA sample, heated at β = 10 ºC/min in a perforated capsule.

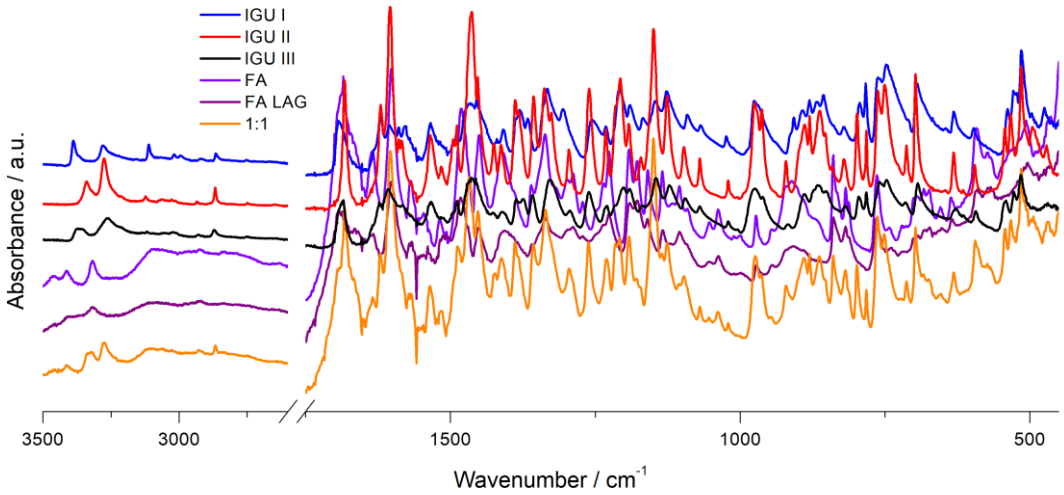

FIG. Apdx1-19 – FTIR-ATR spectra of the three known IGU polymorphs, commercial FA, FA submitted to LAG at 15Hz for 30 minutes with EtOAc, and the equimolar mixture of IGU and FA, obtained in the same conditions.

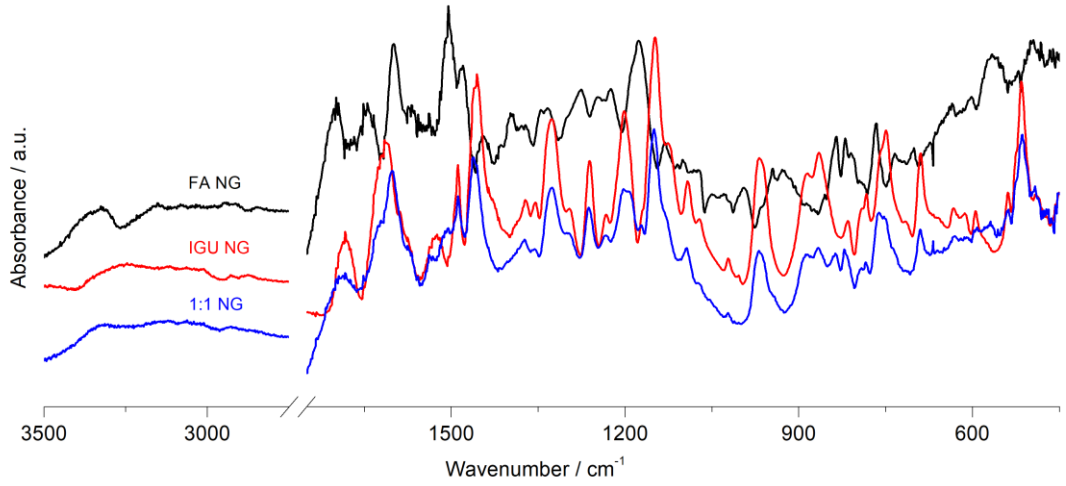

FIG. Apdx1-20 – FTIR-ATR spectra of FA dihydrate, IGU, and IGU:FA 1:1, submitted to NG at 30Hz for 60 minutes, in steel vessels.

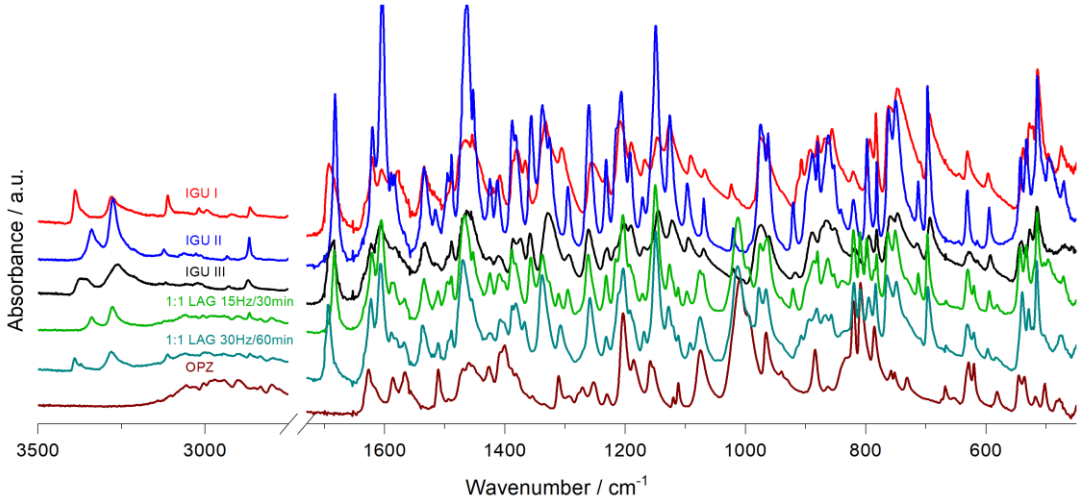

FIG. Apdx1-21 – FTIR-ATR spectra of the known IGU polymorphs, OPZ, and the IGU:OPZ equimolar mixture, obtained with LAG. IGU II was used in the 1:1 mixture grinded at 15Hz for 30 minutes, while IGU I was used in the 1:1 mixture grinded at 30Hz for 60 minutes.

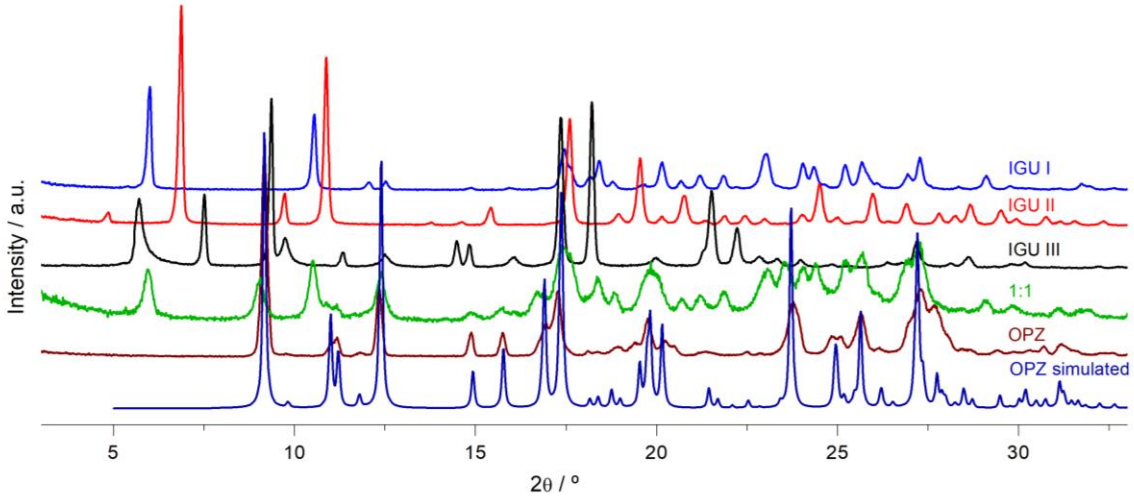

FIG. Apdx1-22 – XRPD diffractogram of the known IGU polymorphs, experimental and simulated OPZ, and the IGU:OPZ equimolar mixture, obtained with LAG.

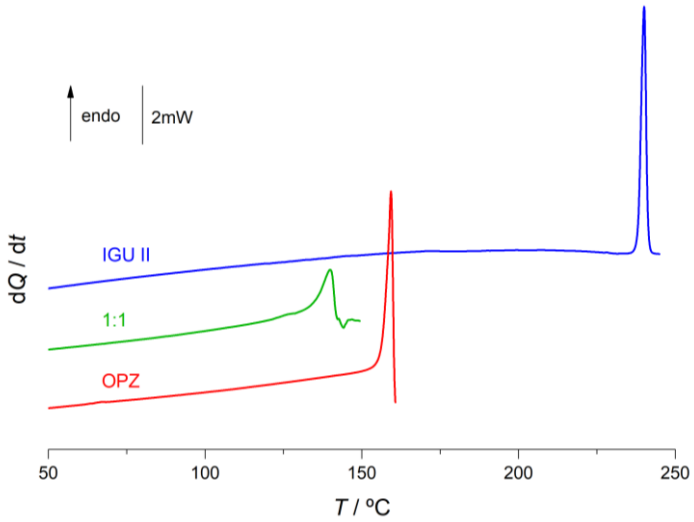

FIG. Apdx1-23 – DSC curves of IGU, OPZ and the 1:1 mixture, obtained with LAG at 15Hz for 30 minutes with EtOAc. β = 10 °C/min.

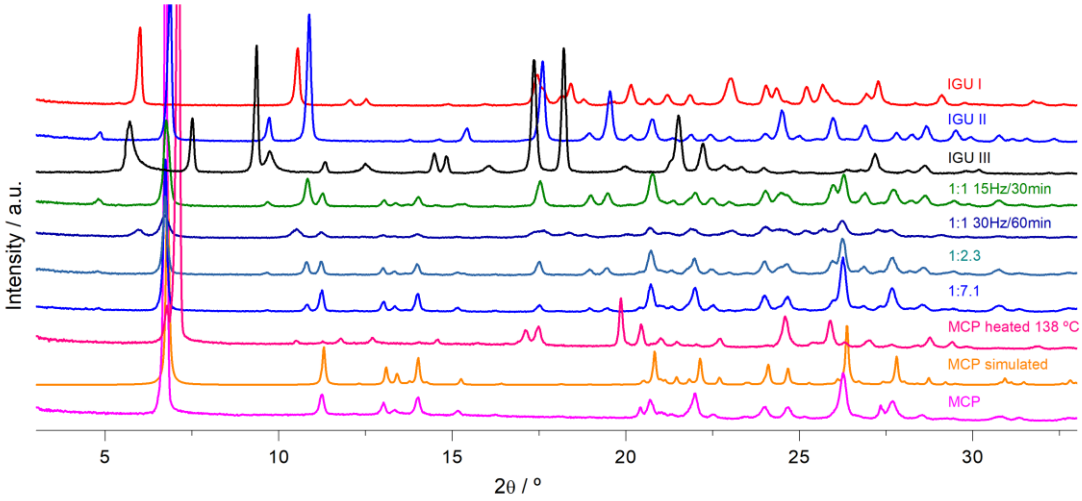

FIG. Apdx1-24 – XRPD diffractogram of the known IGU polymorphs, experimental and simulated MCP, MCP's polymorph, and the IGU:MCP compositions, obtained with LAG.

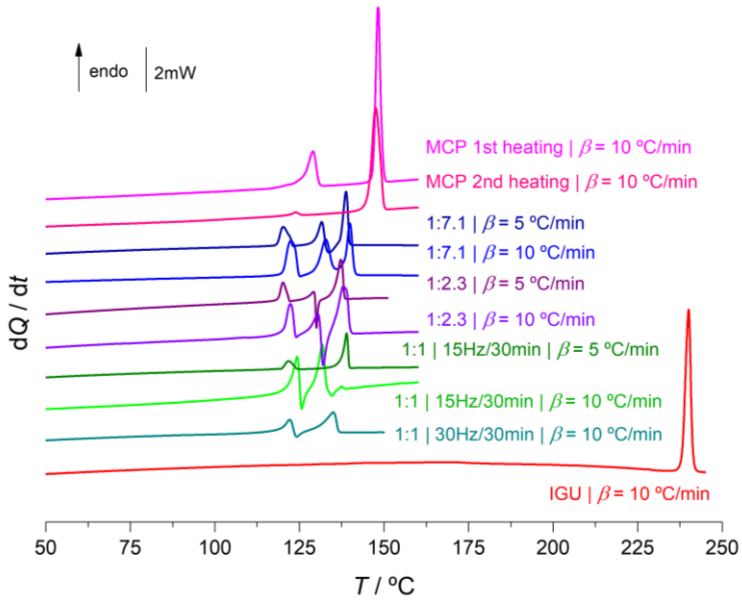

FIG. Apdx1-25 – DSC curves of IGU, MCP, and the IGU:MCP composition, obtained with LAG.

APPENDIX 2

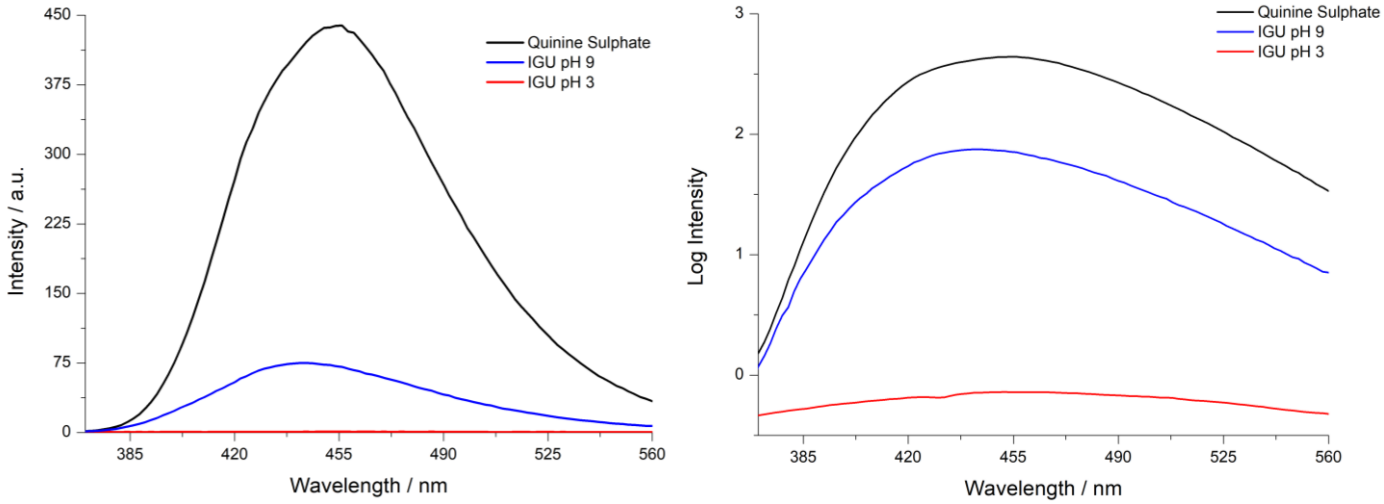

FIG. Apdx2-1 – Fluorescence spectra (**A**) and logarithmic spectra (**B**) of the QS solution and the two IGU solutions, at different pH values. Excitation was done at 320 nm for both QS and IGU pH 3, whereas 346 nm was used for IGU pH 9.

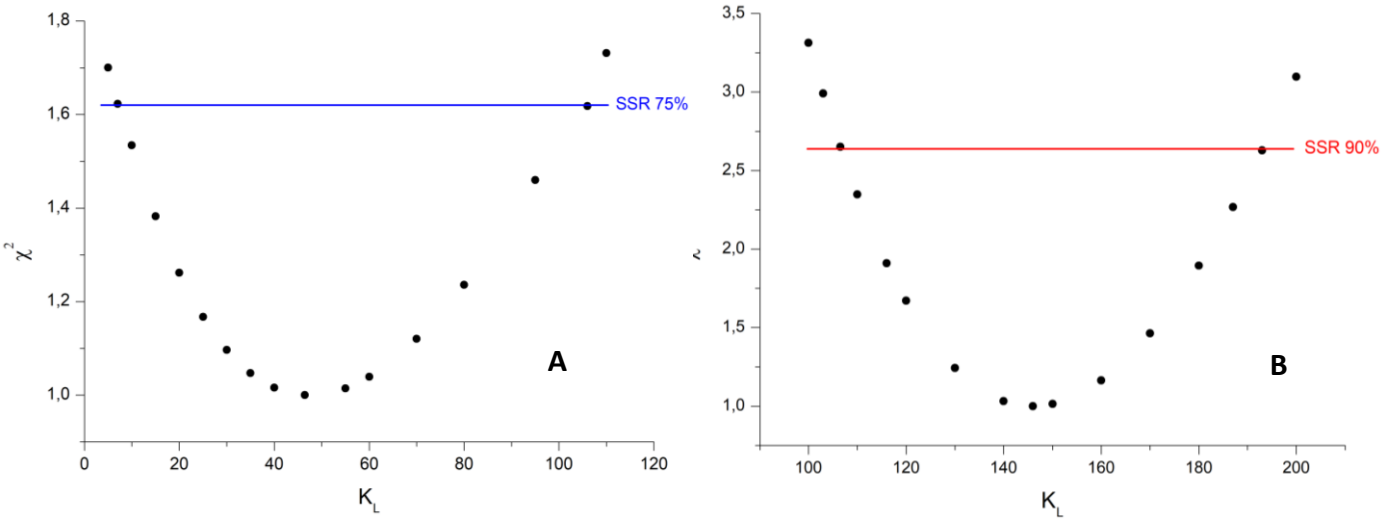

FIG. Apdx2-2 – Chi square test for the KL values obtained for the partition study with POPC (**A**) and with POPC:DDAB (**B**). Confidence intervals are represented on each graph.

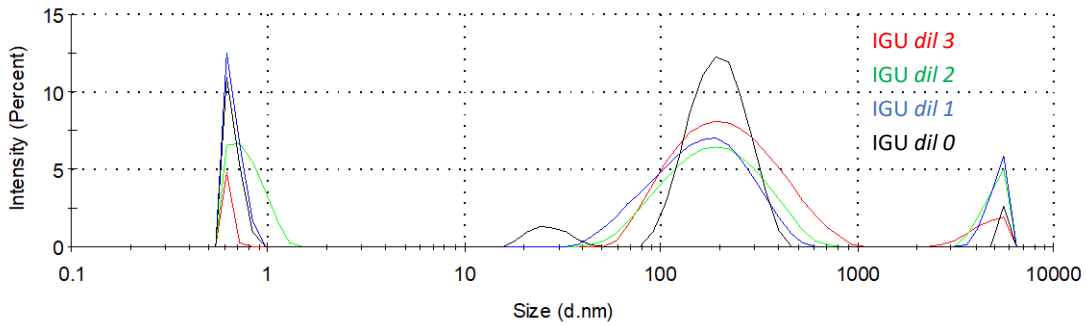

FIG. Apdx2-3 – Size distribution by intensity of the four IGU solutions studied.

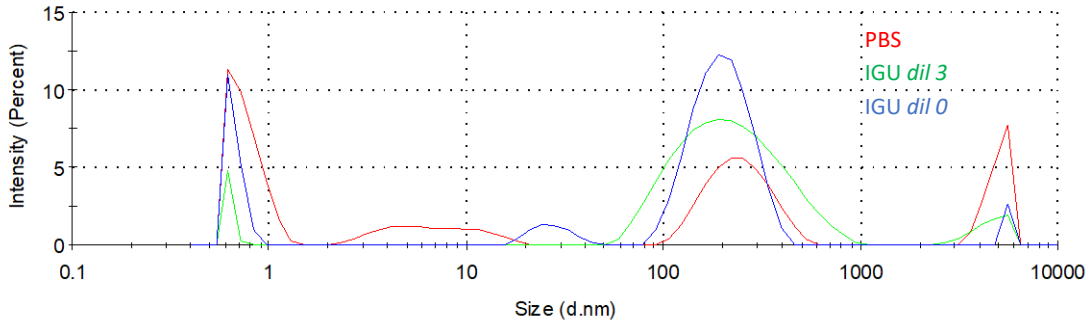

FIG. Apdx2-4 – Size distribution by intensity of the IGU solutions *dil 0* and *dil 3*, compared with the PBS solvent used to prepare the dilutions.